INFORMATION TO USERS

This manuscript has been reproduced from the microfilm master. UMI films the text directly from the original or copy submitted. Thus, some thesis and dissertation copies are in typewriter face, while others may be from any type of computer printer.

The quality of this reproduction is dependent upon the quality of the copy submitted. Broken or indistinct print, colored or poor quality illustrations and photographs, print bleedthrough, substandard margins, and improper alignment can adversely affect reproduction.

In the unlikely event that the author did not send UMI a complete manuscript and there are missing pages, these will be noted. Also, if unauthorized copyright material had to be removed, a note will indicate the deletion.

Oversize materials (e.g., maps, drawings, charts) are reproduced by sectioning the original, beginning at the upper left-hand corner and continuing from left to right in equal sections with small overlaps. Each original is also photographed in one exposure and is included in reduced form at the back of the book.

Photographs included in the original manuscript have been reproduced xerographically in this copy. Higher quality 6" x 9" black and white photographic prints are available for any photographs or illustrations appearing in this copy for an additional charge. Contact UMI directly to order.

UMI

A Bell & Howell Information Company
300 North Zeeb Road, Ann Arbor MI 48106-1346 USA
313/761-4700 800/521-0600

Reproduced with permission of the copyright owner. Further reproduction prohibited without permission.

LIGHT SCATTERING STUDY OF STRUCTURE AND DYNAMICS IN THE LIQUID-GLASS TRANSITION

by

Guoqing Shen

A dissertation submitted to the Graduate Faculty in Physics in partial fulfillment
of the requirements for the degree of Doctor of Philosophy

The City University of New York

1998

UMI Number: 9908362

UMI
300 North Zeeb Road
Ann Arbor, MI 48103

This manuscript has been read and accepted for the Graduate Faculty in Physics in satisfaction of the dissertation requirement for the degree of Doctor of Philosophy

5/20/98

Date

Chairman of Examining Committee

5/28/98

Date

Executive Officer

Joseph L. Birman ____________

Fred H. Pollak ____________

Frederick W. Smith ____________

David Weitz ____________

Supervisory Committee

The City University of New York

ABSTRACT

LIGHT SCATTERING STUDY OF STRUCTURE AND DYNAMICS IN THE LIQUID-GLASS TRANSITION

by

Guoqing Shen

Advisor: Professor Herman Z. Cummins

Polarized and depolarized Brillouin spectra of several fragile glass-forming materials were measured and analyzed by different implementations of the Mountain theory to study the dynamics of liquids near the liquid-glass transition. Isotropic spectra of those materials were also obtained, but the Mountain modes were very weak. The results indicate that the conventional subtraction approach is not valid for liquids of anisotropic molecules with coupling of transverse shear waves and orientational fluctuations. To study the transverse shear waves and orientational fluctuations, polarized and depolarized Brillouin spectra of salol were collected.

Depolarized back-scattering spectra of trimethyl-heptane were obtained in the frequency range of 0.3 GHz to 4000 GHz with a temperature range of 180 to 294K. Analysis of the corresponding susceptibility spectra revealed a reasonable agreement with the predictions of the idealized mode coupling theory.

ACKNOWLEDGMENTS

I would like to express my deep gratitude to my adviser Professor Herman Z. Cummins for his great encouragement, practical tutelage, patient guidance, and continued support throughout my graduate education and research at the City College of New York.

I express my grateful acknowledgment to Professor Robert M. Pick and Professor Wolfgang Gotze in developing crucial theoretical aspects of this research and for their invaluable guidance, suggestions, and discussions.

I thank Professor Jean Toulouse for letting me use ultrasonics apparatus and his helpful discussions and suggestions concerning this research. I also thank Peter Finkel for instructing and helping me in the ultrasonic velocity measurements.

I sincerely thank the members of my thesis committee, Professor Joseph L. Birman, Professor Fred H. Pollak, Professor Frederick W. Smith, and Professor David Weitz for their guidance, suggestions and discussions.

I gratefully thank Dr. Gen Li for his generous discussions and instructions on experiments. I thank Dr. Zhongmo Ju for his friendship and collaboration during these years.

I thank all the people in our group: Dr. Weimin Du, Dr. Joel Hernandez, Dr. Wolfgang Losert, Dr. Harish Barshilia, Dr. Yoon-Hwae Hwang, and the pattern formation group for their assistance, collaboration, and friendship, and for contributing to a helpful and pleasant environment in our lab.

I thank Miss Tracy Turner and Professor Victor Chung for their long time effective assistance and help. I also thank the people in the Electronics shop, Glass shop, Computer Lab, and Machine shop for their professional help in construction and maintenance for our apparatus and equipment.

I gratefully thank all my family members and friends. Through their help, encouragement, and friendship, they have contributed to this dissertation.

DEDICATION

I dedicate this thesis to my father
and my family

CONTENTS

ABSTRACT ---------- iii
ACKNOWLEDGMENTS ---------- iv
DEDICATION ---------- vi
CONTENTS ---------- vii
LIST OF TABLES ---------- ix
LIST OF FIGURES ---------- x

INTRODUCTION

A. Glass and liquid-glass transition ---------- 1
B. The Kauzmann paradox ---------- 5
C. Brillouin scattering studies of the liquid-glass transition ---------- 6
D. Depolarized light scattering ---------- 9
E. Overview of theories of liquid-glass transition ---------- 10

PART I BRILLOUIN SCATTERING SPECTROSCOPY

Chapter 1. Theory of Brillouin scattering

A. Historical sketch of Brillouin scattering ---------- 16
B. General Aspects of Brillouin scattering ---------- 24
C. Simple Liquids of Isotropic Molecules ---------- 27
D. Complex Liquids ---------- 33
E. Depolarized Brillouin spectrum ---------- 38

Chapter 2. Analysis of Brillouin Spectra

A. Simple liquids of isotropic molecules ---------- 45
B. Complex liquids of isotropic molecules ---------- 51
C. Complex liquids of anisotropic molecules ---------- 66

Chapter 3. Experimental Apparatus and Data Processing

A. Principle of the Fabry-Perot interferometer ---------- 70
B. Brillouin scattering apparatus ---------- 77
C. Data processing ---------- 80

Chapter 4. Brillouin scattering measurements

A. Materials -- 85

B. Sample preparation and temperature control ------------------------ 89

C. Brillouin spectra and fitting results for PC and OTP --------------- 90

D. Physical properties of TMH --- 99

E. Density and orientational fluctuations ----------------------------- 106

F. Depolarized spectra of salol -- 114

PART II DEPOLARIZED LIGHT SCATTERING SPECTROSCOPY

Chapter 5. Mode Coupling Theory

A. Equation of motion --- 120

B. Schematic idealized MCT --- 123

C. Predictions of the idealized MCT ----------------------------------- 127

D. Introduction to the extended MCT ---------------------------------- 133

Chapter 6. Tests of Mode Coupling Theory: TMH

A. Experimental apparatus -- 136

B. Data processing --- 138

C. Data analysis and results --- 141

CONCLUSIONS

A. Brillouin scattering spectroscopy ----------------------------------- 153

B. Isotropic spectrum -- 156

C. Depolarized back-scattering spectroscopy ------------------------ 156

D. Future Study --- 159

BIBLIOGRAPHY -- 161

LIST OF TABLES

Table 1-1 Brillouin scattering studies of glasses and glass-forming liquids ---------- 21

Table 2-1 Fitting parameters of different versions of the Mountain theory ---------- 65

Table 4-1 Density of TMH ---------- 100

Table 4-2 Refractive index of TMH ---------- 103

Table 4-3 Integrated intensities of TMH and $CHCl_3$ ---------- 108

Table 4-4 Experimental and theoretical Rayleigh ratios ---------- 109

Table 6-1 Fitting parameters of idealized MCT analysis for α- and β relaxation ---------- 143

Table 6-2 Comparison of relaxation time ---------- 151

Table C-1 MCT analysis parameters for some glass-forming materials --159

LIST OF FIGURES

Fig. I-1 The Angell plot -- 3
Fig. I-2 Schematic Kauzmann paradox ------------------------------------ 5
Fig. I-3 90^0 polarized Brillouin spectrum of CCl_4 ------------------------ 8
Fig. 1-1 Schematic diagram of Brillouin scattering --------------------- 25
Fig. 1-2 Representation of the Brillouin spectrum of simple liquids -- 29
Fig. 1-3 VV spectra of TMH at some temperatures --------------------- 32
Fig. 1-4 VV, VH, and ISO spectra of OTP at T = 340K ---------------- 37
Fig. 1-5 VH spectra of salol --- 39
Fig. 1-6 Schematic diagram of scattering geometry -------------------- 40
Fig. 1-7 VH spectra of OTP and PC ------------------------------------- 43
Fig. 2-1 VV spectra of PC at different temperatures -------------------- 46
Fig. 2-2 3 Lorentzians fit for PC at 240K -------------------------------- 47
Fig. 2-3 Hydrodynamic theory fit for PC at 240K ---------------------- 49
Fig. 2-4 VV spectrum of water at room temperature -------------------- 51
Fig. 2-5a 4 Lorentzians fit for PC at 240K -------------------------------- 53
Fig. 2-5b 4 Lorentzians and their sum ------------------------------------ 53
Fig. 2-6 Mountain theory fit for PC at 240K --------------------------- 55
Fig. 2-7 VV spectra of PC with Mountain theory fits ------------------ 56
Fig. 2-8 Comparison of 4 Lorentzians and Mountain theory fits ------ 59
Fig. 2-9 Generalized hydrodynamic equation fit for PC at 240K ------ 61
Fig. 2-10 Comparison of Generalized hydrodynamic equation and Mountain theory fits -- 62
Fig. 2-11 Calculated curve of Generalized hydrodynamic equation from Mountain theory fit --- 63
Fig. 2-12 Generalized hydrodynamic equation fit with Cole-Davidson function --- 64
Fig. 2-13 VV, VH, ISO spectra of PC at 240K ---------------------------- 67
Fig. 2-14 VV, VH, and ISO spectra of Salol at 230 K -------------------- 69
Fig. 3-1 Diagram of a FP interferometer ---------------------------------- 70
Fig. 3-2 Schematic transmission function -------------------------------- 71
Fig. 3-3 Diagram of a tandem FP interferometer ----------------------- 74
Fig. 3-4 Transmission function of the TFPI ----------------------------- 76
Fig. 3-5 Schematic Brillouin scattering apparatus ----------------------- 78
Fig. 3-6a VV spectrum of acetone in channel numbers -------------------- 82
Fig. 3-6b VV spectrum of acetone in frequency --------------------------- 82
Fig. 4-1a Chemical structure of Propylene Carbonate -------------------- 86

Fig. 4-1b Chemical structure of Ortho-Terphenyl ---------------------------- 86

Fig. 4-1c Chemical structure of Trimethyl-heptane --------------------------- 86

Fig. 4-2 Diagram of the sample holder -- 90

Fig. 4-3a VV spectra of OTP at some temperatures ----------------------------- 91

Fig. 4-3b VV spectra of PC at some temperatures ------------------------------ 91

Fig. 4-4a VV spectra of OTP with simplified Mountain theory fits ------ 93

Fig. 4-4b VV spectra of PC with simplified Mountain theory fits -------- 93

Fig. 4-5a Brillouin mode shift ω_B with high and low frequency limit of OTP -- 94

Fig. 4-5b Brillouin mode shift ω_B with high and low frequency limit of PC --- 94

Fig. 4-6a Linewidths of Rayleigh mode $\Delta\omega_R$, Mountain mode $\Delta\omega_M$, and Brillouin mode of $\Delta\omega_B$ OTP from the 4-Lorentzian fit ---- 94

Fig. 4-6b Linewidths of Rayleigh mode $\Delta\omega_R$, Mountain mode $\Delta\omega_M$, and Brillouin mode of $\Delta\omega_B$ PC from the 4-Lorentzian fit ------ 94

Fig. 4-7a Landau-Placzek ratios of OTP --------------------------------------- 95

Fig. 4-7b Landau-Placzek ratios of PC -- 95

Fig. 4-8a Relaxation times of OTP -- 96

Fig. 4-8b Relaxation times of PC --- 96

Fig. 4-9a Longitudinal sound velocity v of OTP ----------------------------- 96

Fig. 4-9b Longitudinal sound velocity v of PC ------------------------------ 96

Fig. 4-10a Nonergodicity factor of OTP -------------------------------------- 98

Fig. 4-10b Nonergodicity factor of PC --------------------------------------- 98

Fig. 4-11 Intensity of TMH -- 101

Fig. 4-12 Schematic diagram of the refractive index measurement ------ 102

Fig. 4-13 Refractive index of TMH -- 103

Fig. 4-14 Lorentz-Lorentz relation -- 104

Fig. 4-15 Ultrasonic velocity of TMH --------------------------------------- 105

Fig. 4-16 Specific heat of TMH -- 105

Fig. 4-17a VV and VH spectra of TMH in a wide frequency range (0 ~ 4000 GHz) -- 107

Fig. 4-17b VV and VH spectra of $CHCl_3$ in a wide frequency range (0 ~ 4000 GHz)-- 107

Fig. 4-18a VV and VH Brillouin spectra of TMH at 160K ---------------- 109

Fig. 4-18b VV spectra of TMH with Mountain theory fit ------------------ 110

Fig. 4-19 Brillouin shift ω_B with high and low frequency limit ---------- 111

Fig. 4-20 Linewidths of Rayleigh mode $\Delta\omega_R$, Mountain mode $\Delta\omega_M$, and Brillouin mode of $\Delta\omega_B$ OTP from the 4-Lorentzian fit --------- 111

Fig. 4-21 Landau-Placzek and specific heats ratios of TMH -------------- 112
Fig. 4-22 Relaxation times -- 113
Fig. 4-23 Acoustic sound and ultrasonic velocities ------------------------ 113
Fig. 4-24 Nonergodicity factor of TMH ------------------------------------- 114
Fig. 4-25 VV and VH spectra of salol at 370K ---------------------------- 116
Fig. 4-26 VH spectra of salol at some temperatures ----------------------- 116
Fig. 5-1a Correlation function $\Phi(t)$ -- 125
Fig. 5-1b Susceptibility spectrum $\chi''(\omega)$ ----------------------------------- 125
Fig. 5-2 Nonergodicity factor --- 127
Fig. 6-1 Diagram of the Raman apparatus -------------------------------- 137
Fig. 6-2a Depolarized back-scattering spectrum of TMH at FSR = 18.75 GHz and T = 220 K -------------------------------------- 139
Fig. 6-2b Four TFPI spectra and a Raman spectrum of THM at T = 220 K --- 139
Fig. 6-2c Composite intensity spectrum of TMH at T = 220 K ---------- 139
Fig. 6-2d Corresponding susceptibility spectrum of TMH at 220 K ----- 139
Fig. 6-3 Depolarized back-scattering spectra of TMH ------------------- 140
Fig. 6-4 Corresponding susceptibility spectra ---------------------------- 142
Fig. 6-5 The interpolation fitting of β-relaxation region and the stretched exponential model fitting α-relaxation --------------- 144
Fig. 6-6 Master function fit of β-relaxation ------------------------------ 145
Fig. 6-7a Power law of scale frequency ------------------------------------- 146
Fig. 6-7b Power law of scale susceptibility -------------------------------- 146
Fig. 6-8 Susceptibility minimum versus frequency minimum ----------- 146
Fig. 6-9 Master function fit of α-relaxation ------------------------------ 148
Fig. 6-10 Stretched exponent β -- 149
Fig. 6-11 Power law of α-relaxation --------------------------------------- 150
Fig. 6-12 Comparison of relaxation time ---------------------------------- 151

INTRODUCTION

After more than 100 years of research, the nature of the glassy state and the physical processes underlying the liquid-glass transition remain incompletely understood and highly controversial. It is not yet known whether or not there is a thermodynamic phase transition underlying this phenomenon since no order parameter has ever been identified. To date, It has not been definitively established if the glassy state is distinct from the supercooled liquid in any sense except for the extremely long structural relaxation times of glasses, i.e. if the liquid-glass transition is purely kinetic.

Many experimental techniques have been exploited in the study of glasses and of the liquid-glass transition, and with the increasing precision of modern experimental methods have been able to provide critical tests of some of the theoretical models. Light scattering spectroscopy has been widely employed because it provides a very large dynamic range with high resolution. In this thesis, I present an analysis of the low-frequency Brillouin spectra of some fragile glass-forming materials with several versions of hydrodynamic theory in Part I. In Part II, I present a broad-frequency range depolarized light scattering study of a glass-forming material of TMH, and an analysis of the data based on the mode coupling theory (MCT) of the liquid-glass transition.

A. Glass and the Liquid-Glass Transition

Glass and the glass transition

The glassy state is a metastable (non-equilibrium) state which is one form of amorphous solid [1]. Most liquids will eventually solidify as the temperature decreases.

If a liquid does not crystallize easily and is cooled fast enough to avoid crystallization, it will become a supercooled liquid if the temperature is lower than the melting temperature T_m and transform to a glass if the temperature passes the glass transition temperature T_g. One of the important differences between liquid and glass is the viscosity η. The viscosities of supercooled liquids increase rapidly with decreasing temperature, from $\eta \sim 10^{-1}$ poise at the melting temperature T_m to 10^{13} poise at T_g which is the definition of the glass transition temperature [1]. Similarly, the structural relaxation time τ increases with decreasing temperature, from $\tau \sim 10^{-12}$ seconds at $T \sim T_m$ to $\tau \sim 10^2$ seconds at T_g.

The Arrhenius law and Williams-Landel-Ferry equation

The Arrhenius law, $\eta(T) = \eta_0 \exp(E_A / k_B T)$ is frequently used to describe the temperature dependent viscosity $\eta(T)$ of materials, where E_A is the activation energy. It works well for many strong glass-forming materials (strong and fragile glasses will be defined in the next section). However, for fragile glass-forming materials, a much better fit can be obtained with the Vogel-Fulcher equation, $\eta(T) = \eta_0 \exp[A / k_B(T-T_0)]$ (The Arrhenius law can be obtained from the Vogel-Fulcher equation if $T_0 = 0$).

Another widely used equation for viscosities $\eta(T)$ is the Williams-Landel-Ferry equation: $\log\left[\frac{\tau_\alpha(T)}{\tau_\alpha(T_S)}\right] = -\frac{C_1(T-T_S)}{(C_2+T-T_S)}$, where T_S is a material-dependent reference temperature. The Williams-Landel-Ferry equation is equivalent to the Vogel-Fulcher equation if T_S is fixed with $C_1 = B/C_2$ and $C_2 = T_S - T_0$. τ and η are connected by the Maxwell relation: $\tau = \eta / G_\infty$, where G_∞ is the high frequency shear modulus.

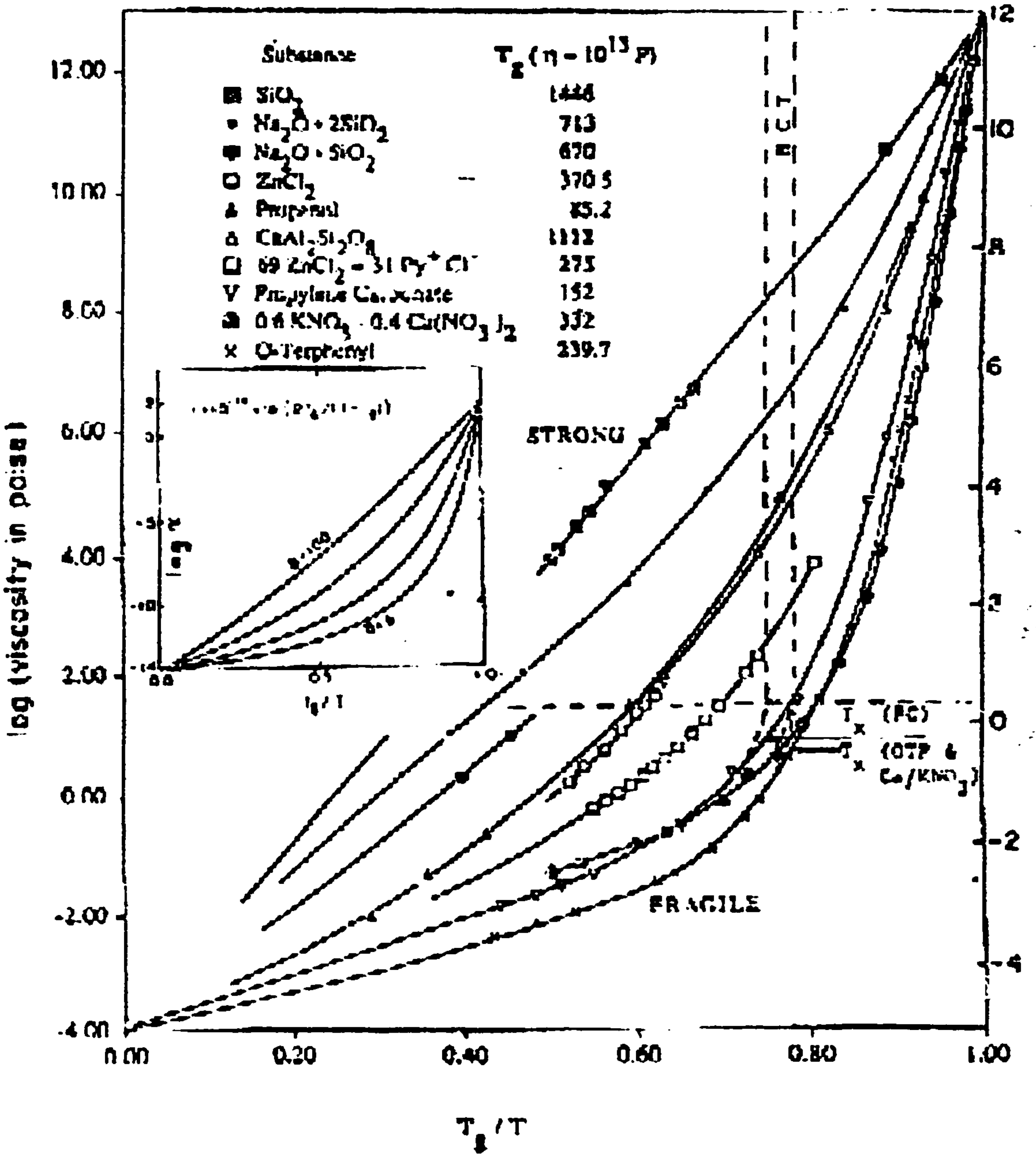

Figure I -1. The Angell plot of the viscosities $\eta(T_g/T)$ as functions of T_g/T (from reference [2]). The viscosities of strong glass-forming materials obey the Arrhenius law (straight line), while the viscosities of fragile glass-forming materials increase much faster than the Arrhenius law when the temperature decreases.

The Angell plot

Figure I-1 is the Angell plot [2] which is widely used to present viscosities $\eta(T)$ of glass-forming materials. The interactions between molecules determine whether a glass-forming material is strong or fragile. In the strong glass-forming materials, such as SiO_2, the molecules interact covalently and are connected by a network of covalent bonds. In the fragile glass-forming materials, such as ortho-terphenyl (OTP), molecules interact through the weak non-directional van der Waals force.

Fragility index

Following the scheme suggested by Angell, structural glass-forming materials can be classified quantitatively by a fragility index $m = \left[\frac{d(\log < \tau >}{d(T_g / T)} \right]_{T=T_g}$, where $<\tau>$ is either the viscosity or the average α-relaxation time, with the strong glass-forming materials such as SiO_2 (m=20) falling in the lower m region and the fragile glass-forming materials such as OTP (m=81) falling in the higher m region [3].The liquid-glass transition is generally thought to be a dynamic transition which cannot be defined by the appearance of an order parameter at the glass transition temperature T_g because of the lack of long range spatial order in the glass state. For example, when liquid Glucose is cooled, the heat content and the specific volume show no abrupt change [4]. However, its coefficient of thermal expansion drops abruptly by more than a factor of 3 and its specific heat decreases by nearly a factor 2. These changes occur within a temperature range of ~ 20K. It was found that the glass transition temperature T_g depends on the cooling rate and the measurement time. T_g is higher at high cooling rates or short time-period measurements [1].

B. The Kauzmann paradox

The Kauzmann paradox

In 1948, Kauzmann [4] pointed out a peculiar thermodynamic circumstance presented by glass-forming materials, connected with the observation that the entropy of a fragile liquid substantially exceeds that of the crystalline solid. The entropy curves, shown by the heavy lines in Fig. I-2 for these two phases, when extrapolated to low temperature appear to cross at a positive temperature T_K (the Kauzmann temperature) which is found to be close to T_0 in the Vogel-Fulcher equation.

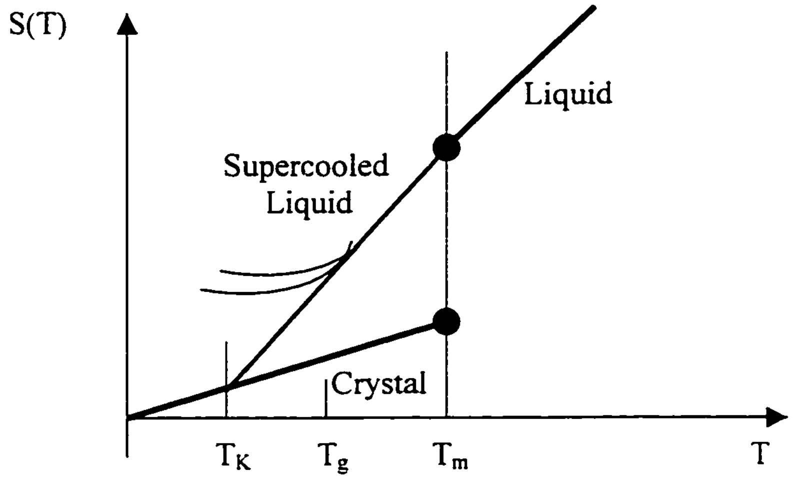

Figure I-2. Schematic view of the Kauzmann paradox

As Fig.I-2 shows, the entropy of the supercooled liquid stops following the extrapolation (because of structural arrest) at a value that decreases as the cooling rate decreases. Since T_K is lower than T_g (for fragile glass-forming liquids $T_g/T_K \sim 1.1$) where structural arrest occurs for experimentally possible cooling rates, the Kauzmann point is unreachable. But in principle, one could make the cooling rate slow enough to keep the system in equilibrium down to and below T_K. This implies that the manifestly disordered glass would have entropy lower then that of the ordered crystal when the temperature was below the Kauzmann temperature T_K, which would violate the third law of thermodynamics.

Some explanations

Kauzmann suggested that the way to avoid the Kauzmann paradox was to claim that nucleation of the crystal phase from the supercooled liquid became overwhelmingly probable as T_k is approached more and more slowly from above. However, experimental evidence on the homogeneous nucleation behavior of glass-forming materials apparently contradicts this view in the view of some authors [5]. An alternative viewpoint [6] is that T_k represents an idealized liquid-glass transition temperature. In this case, the supercooled liquid attains a vanishing configurational entropy at $T_k > 0$, and this point is a second-order phase transition point. Below T_k the ideal glass would retain its essentially unique configuration. However, no generally accepted evidence for this transition has even been found.

C. Brillouin Scattering Studies of the liquid-Glass Transition

Brillouin scattering spectroscopy

The liquid-glass transition has been studied for many years with various experimental techniques such as viscometry, dielectric response, ultrasonics, neutron scattering, NMR, light scattering (Raman and Brillouin), photon correlation spectroscopy, and computer simulation.

Brillouin scattering spectroscopy is a powerful tool due to its large spectral frequency range and high resolution for the study of the structure and dynamics of materials. Brillouin scattering in dense media is caused by fluctuations of the local dielectric tensor $\Delta\varepsilon$ [7].

Brillouin spectrum

In liquids of isotropic molecules, the thermally excited density and temperature variations lead to such fluctuations. The Brillouin spectrum of simple liquids (non-relaxing) has three components, one unshifted Rayleigh (thermal diffusion) mode and two symmetrically shifted Brillouin modes (longitudinal acoustic phonons). The Brillouin modes are shifted in frequency because of the phonon propagation. Fig. I-3 shows a typical Brillouin scattering spectrum of CCl_4 in the polarized geometry $I_{VV}(\omega)$ at room temperature. The shape of a Brillouin spectrum is determined by the thermodynamic parameters and transport coefficients of the liquid. Therefore, an analysis of experimentally determined spectra can yield information concerning these quantities for the liquid at different temperatures.

Mountain mode

In liquids with slowly relaxing internal degrees of freedom, the Brillouin spectrum becomes more complicated, as first described by Mountain [8]. With decreasing temperature there is a broadening and shift of the Brillouin components related to the strength and relaxation time of the new degree of freedom. Also, a fourth component (the Mountain mode) appears between the Brillouin components, Fig. I-3. This approach has been widely used to study supercooled liquids approaching the liquid-glass transition, with the structural relaxation playing the role of Mountain's internal degree of freedom. Initially, several studies tracked the position and width of the Brillouin components with temperature, and extracted the temperature dependence of the sound velocity and attenuation which could then be compared with theoretical predictions.

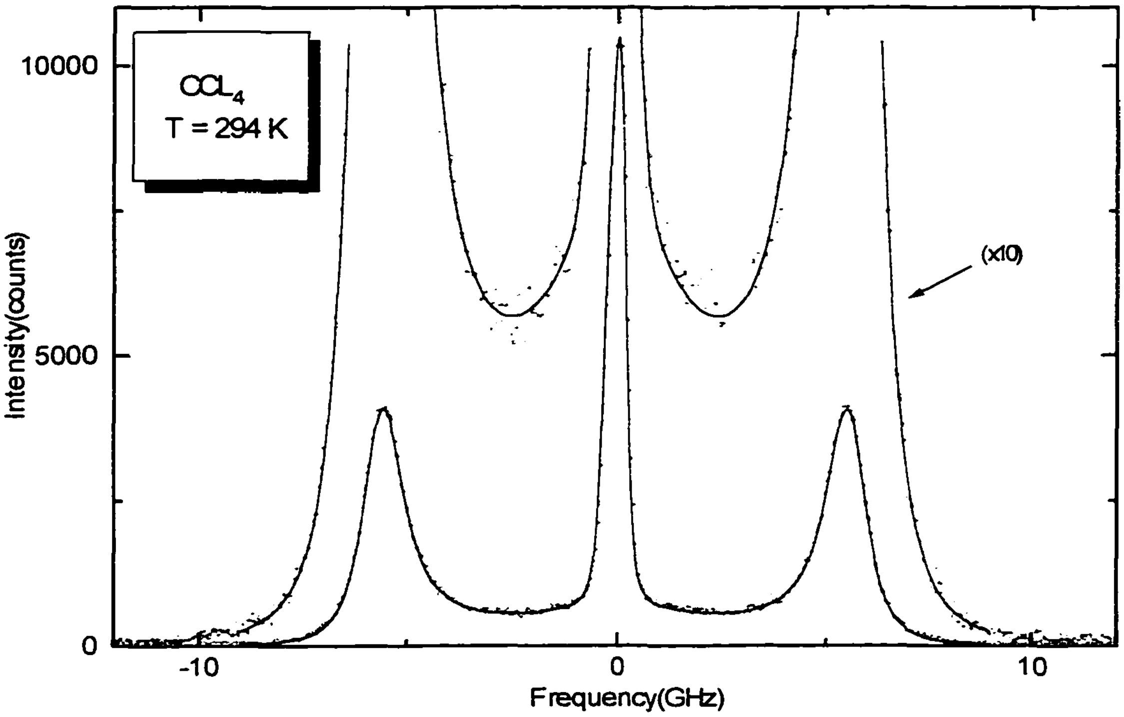

Figure I-3. The Polarized Brillouin spectrum of CCl_4 at T= 294K. Note the presence of an additional broad component between the Brillouin peaks. This the Mountain mode which will be described later.

In most previous studies, only the frequency shifts and linewidths of the Brillouin peak and the linewidth of the Rayleigh peak were analyzed, while the additional information contained in the detailed shapes of the spectra was ignored. More recently, spectra have been analyzed by fitting to the full expressions for the spectrum derived by Mountain. We will review the procedures for such comparisons in chapter 2.

Orientational and translational motions

Additional complications develop when the molecules in the glass-forming liquid are optically anisotropic, a possibility not included in the Mountain hydrodynamic description. Such anisotropy gives rise to additional structure in the spectrum which must be included in a complete analysis. Specifically, orientational dynamics and the coupling of orientational dynamics and shear waves produce additional spectral structure which contributes to both the polarized and depolarized spectra.

D. Depolarized light Scattering

Coupling of orientational and translational motions

The coupling of orientational and translational motions in liquids with anisotropic molecules has been generally neglected in the analysis of polarized Brillouin spectra. Liquids with anisotropic molecules were usually treated with the assumption that these two motions are independent. Kivelson and co-workers [9-10] considered this effect in liquids with symmetric top molecules and introduced two parameters: the dynamic coupling parameter R which accounts for the coupling between shear waves and the orientational motion, and the decay rate Γ of the orientation process which is approximately equal to the half-width of the depolarized spectrum. R can be shown to be related to the coupling parameter between shear waves and orientational motion in the depolarized spectrum [10].

Depolarized spectra

In the polarized spectrum, the unshifted central peak (or peaks) is due to entropy and orientational fluctuations and the shifted Brillouin components are due to the propagating longitudinal acoustic waves. Relaxation processes give rise to the Mountain mode and also effect the linewidth of the Brillouin modes.

The depolarized spectrum arises from scattering by the shear acoustic waves and fluctuations of anisotropy associated with molecular reorientation processes. The shear wave is over-damped in the normal viscous liquid region where a dip in the central component appears at high temperatures in the VH spectrum. As the liquid is supercooled, the shear wave becomes under-damped and gives rise to a symmetric shifted doublet due to propagation of transverse acoustic waves with very weak intensity compared to the central component.

E. Overview of Theories of the Liquid-Glass Transition

Several theories have been developed to explain the phenomenon of the liquid-glass transition such as the entropy theory [11], free volume theory [12-13], and mode coupling theory [14-16]. The entropy theory and free volume theory basically focused on structural aspects while the mode coupling theory is focused on aspects of the dynamics of supercooled liquids:

a. What is the microscopic origin of the relaxation processes in supercooled liquids ?

b. What is the detailed time dependence of structural relaxation functions ?

c. What is the specific signature of the liquid-glass transition?

The early theories (entropy, free volume) of the liquid-glass transition presume that a real transition will take place if the cooling rate is infinitely slow [17], which puts the critical temperature below the glass transition temperature T_g. The mode coupling theory, in contrast, predicts the existence of a dynamic instability at a crossover temperature T_c somewhat above T_g, by about 30-100 K.

Entropy theory

Following Gibbs and DiMarzio, Adam and Gibbs [11] analyzed the relaxation behavior of glass-forming liquids based on the configurational entropy S_{config} which vanishes at a second-order phase transition temperature T_2 and suggested that the relaxation involved cooperatively rearranging regions of increasingly larger size with decreasing temperature. The configurational entropy is the difference between the entropies of the liquid and crystal which decreases with decreasing temperature as can be seen in Fig. I-2. They calculated the α relaxation time $\tau_\alpha(T)$ for the allowed size distribution of cooperatively rearranging regions and obtained a result nearly identical to the Williams-Landel-Ferry equation. The existence of cooperatively rearranging regions was supported by experiments and is also predicted by free volume theory as described in the following section.

Free volume theory

The basic assumption of free volume theory is that the free volume v_f available for a molecule is the volume v within the transient cage formed by its neighbors minus the minimum volume v_c required by the molecule. In the extended form of free volume theory, Cohen and Grest [17] analyzed the statistical distribution of clusters of liquid-like cells (with $v > v_c$) and solid-like cells (with $v < v_c$) and found that above the percolation threshold, there is an infinite cluster of liquid-like cells and the material can be considered as a liquid; Below the percolation threshold, only finite liquid-like clusters exist.

Both the entropy theory and free volume theory provide excellent fits to viscosity $\eta(T)$ or relaxation time $\tau(T)$ data, but neither provides any insight into the dynamics of supercooled liquids or glasses.

Mode coupling theory

Mode coupling theory (MCT) was advanced as a possible theory of the liquid-glass theory by Leutheusser [14] and Bengtzelius, Gotze, and Sjolander [15] in 1984, then developed primarily by Gotze and Sjogren [16, 18]. In MCT, the system is described by a set of coupled dynamic equations for the density fluctuations. MCT provides detailed predictions for many experimentally accessible aspects of the liquid-glass transition dynamics and has motivated many of the recent experimental investigations of the liquid-glass transition. MCT [18] predicts a dynamic singularity at a crossover temperature T_C, somewhat above T_g. This crossover temperature T_C is an equilibrium parameter of the system which separates the supercooled liquid state into two regions: the strongly supercooled low temperature side $T < T_C$ and the moderately supercooled high temperature side $T > T_C$. A two-step relaxation process is predicted by MCT: for $T > T_C$ but near T_C an initial power law critical decay towards a plateau f^c, followed by a second power law decay which is the beginning of the primary α-relaxation process.

For any given material, MCT predicts that anomalies occur at T_C for all variables that couple to density fluctuations. Therefore, the same T_C should be found for a given material from any appropriate experiment, e.g. neutron scattering, light scattering, or photon correlation spectroscopy. There are two versions of the mode coupling theory, called the idealized MCT and the extended MCT. The extended MCT includes the extra hopping effect, while the idealized MCT only considers the cage effect.

The idealized MCT is based on generalized kinetic equations for density fluctuation dynamics in supercooled liquids, and predicts structural arrest of the density fluctuations at T_C due to mode coupling effects. MCT predicts the evolution of the density fluctuation dynamics near the dynamic ergodic to nonergodic transition at the crossover temperature T_C. The MCT predictions include: a) a two-step relaxation process (the slow α and the fast β relaxations); b) structural arrest at T_C with a non-zero infinite-time asymptote of the density fluctuation correlation function $\Phi_q(t\to\infty) = f_q^c$; c) scaling of the α-relaxation above T_c and of the β-relaxation both above and below T_c [16,18].

To test mode coupling theory, many fragile glass-forming materials were studied with various experimental techniques which verified some of those predictions. Although many of the crucial experiments have utilized neutron scattering, it was found that depolarized light scattering spectroscopy provides the complete susceptibility spectrum described by MTC.

The depolarized back scattering spectra of CKN [19-20], salol [21], PC [22], glycerol (an intermediate glass-forming material) [23] and OTP [24] have been analyzed in our laboratory using both the idealized and extended MCT. The nonergodicity parameter f was calculated using the fitting parameters obtained from the Brillouin scattering spectrum. A related study of OTP had been reported by Steffen et al. [25] who extended the spectral window to a wide frequency region (14 decades) by combining the photon correlation spectrum and confocal spectroscopy with the depolarized light scattering spectrum obtained with a tandem Fabry-Perot interferometer and a Raman spectrometer.

In the first part of this thesis, I will present a detailed review of Brillouin scattering spectroscopy and of the procedures used to analyze experimental spectra. In part II, I will review the MCT and its application in the analysis of depolarized light scattering spectra. I will then present depolarized spectra of the molecular glass-forming material TMH (2,4,6-trimethyl-heptane) and its analysis with MCT.

PART I

BRILLOUIN SCATTERING SPECTROSCOPY

Chapter 1

Theory of Brillouin Scattering

A. Historical Sketch of Brillouin Scattering

Rayleigh Law

The basic theory of light scattering was developed a century ago [26]. The earliest experimental study was carried out by Tyndall (1869). He found that when white light was scattered by very fine particles, the scattered light was partly polarized and also slightly blue in color at 90° scattering angle. He concluded that both the polarization and the blue color of light from the sky were caused by scattering of sunlight by dust particles in the atmosphere.

Two years later (1871), Lord Rayleigh first explained the observed polarization and color of the sunlight scattered in the atmosphere. He also pointed out that light could be scattered by the molecules in pure gases. Subsequently, Rayleigh (1881,1889) [27-28] deduced the same results from Maxwell's electromagnetic wave theory and found that for non-interacting, non-absorbing, and optically isotropic particles having sizes very small compared to the wavelength of the incident light, the intensity of scattering should be proportional to the inverse fourth power of the wavelength, the well-known Rayleigh law:

$$I_S = I\frac{9\pi^2 NV^2}{2\lambda^4 r^2}\left(\frac{\kappa-\kappa_0}{\kappa+2\kappa_0}\right)^2(1+\cos^2\phi), \qquad [1.1]$$

where I is the intensity of unpolarized incident light, N is the number of scattering particles in the volume V, r is the distance to the point of observation, ϕ is the angle though which the light is scattered, λ is the wavelength of incident light, and κ,κ_0 are the relative permittivities of the particles and the medium, respectively.

Since then, Rayleigh's approach had been developed to cover anisotropic and absorbing particles having sizes comparable to the wavelength of the incident light. Although Rayleigh's theory works well in gases, it was found to predict too large intensities in dense media such as liquids and solids, and even gases at atmospheric pressure. In these cases, the molecular separation is small compared with the wavelength of light leading to destructive interference effects.

Einstein equation

Einstein (1910)[7] was able to bypass this difficulty by assuming the liquid to be a continuous medium in which thermal fluctuations cause density fluctuations. He carried out a calculation of the intensity of the scattered light based on thermodynamic fluctuation theory for the mean-square fluctuations in the density:

$$I_S = I\frac{Vq_0^4}{16\pi r^2}\sin^2\phi\left(\frac{\partial\varepsilon}{\partial\rho}\right)_T^2 <(\Delta\rho)^2>, \qquad [1.2a]$$

with

$$<(\Delta\rho)^2>=(k_BT)\rho^2\chi_T \qquad [1.2b]$$

where I is the intensity of incident light, V is the volume, q_0 is the wavevector of incident light, r is the distance to the point of observation, ϕ is the angle though which the light is scattered, ε is the dielectric constant, k_B is the Boltzmann constant, T is the temperature, χ_T is the compressibility and ρ is the density of the medium.

Brillouin prediction

All these earlier studies focused only on the intensity of the scattered light. Progress in understanding its frequency spectrum was first made by Brillouin (1914, 1922)[29-30]. He calculated the spectrum of light scattered by the density fluctuations associated with sound waves, and found that the spectrum of a fluid consists a doublet (Brillouin doublet) split symmetrically around the frequency of the incident light. The splitting, which is much smaller than the frequency of the incident light, is determined by the velocity of the sound wave.

In the early 1930s, Gross [31] carried out a series of light scattering experiments on liquids using a very high resolution Echelle grating spectrometer and first observed the predicted Brillouin doublet. He also noticed the presence of another unshifted central component (Rayleigh line).

Landau-Placzek ratio

Landau and Placzek (1934)[32] suggested a theoretical explanation of the spectrum based on hydrodynamics and attributed the Rayleigh line to non-propagating temperature fluctuations. They showed that the ratio of the integrated intensity of the Rayleigh component I_R to that of Brillouin doublet $2I_B$ is given by the specific heat ratio (Landau-Placzek ratio): $I_R/2I_B = (c_P-c_V)/c_V$, where c_P and c_V are the specific heats at constant pressure and volume, respectively.

Mountain theory

In 1966, Mountain carried out the complete analysis of light scattering by simple fluids based on continuum hydrodynamics, suggested (but not published) by Landau and Placzek. Mountains derivation has also been reviewed and elaborated in several books, including Boon and Yip [33] and Berne and Pecora [34]. Mountain also analyzed the spectrum produced by a liquid having internally relaxing degrees of freedom [8, 35-36]. He assumed that the spectrum for a liquid of isotropic molecules with an internal degree of freedom can be represented by introducing a frequency dependent bulk viscosity. In particular, the energy transfer from the internal degrees of freedom can be described by a single relaxation time. He pointed out that not only are the shift and width of the Brillouin lines modified, but a new unshifted component (Mountain mode) appears in the spectrum, which has been observed subsequently. The integrated intensity ratio of the components is no longer given by the conventional Landau-Placzek ratio.

Rytov prediction

Rytov (1957) [37] predicted that there is a doublet centered at the incident frequency in the depolarized spectrum of liquids with optically anisotropic molecules using a phenomenological theory. In 1967, Stegeman and Stoicheff

[38-39] studied the depolarized spectra of several anisotropic materials and observed this central dip at high temperatures.

Previous Brillouin scattering experiments

The first observations of the Brillouin scattering spectrum using laser excitation were reported with an ultrahigh-resolution Fabry-Perot etalon by Chiao et al. (1964) [40] and with a grating spectrometer by Benedek (1964) [41]. Gornall and his co-workers (1966) [42] first observed the Mountain mode in the Brillouin spectrum of CCl_4. Since those pioneering researches, many studies have appeared. Table 1-1 lists previous experimental studies of glasses and the liquid-glass transition using Brillouin scattering.

Brillouin scattering studies of Propylene Carbonate (PC)

Du et al.[22] measured the VV and VH Brillouin spectra of PC over a large temperature range. The isotropic spectra were calculated from the VV and VH spectra by determining the geometrical constant from the intensity ratio of VV and VH spectra. The nonergodicity factor f_0 was computed from the isotropic spectra.

Torell [43] and coworkers carried out a series of Brillouin scattering studies of PC and fitted the Brillouin spectra using generalized hydrodynamic theory with the Cole-Davidson model for the structure relaxation. The sound velocities at the low (C_0) and high (C_∞) frequency limits were treated as fitting parameters in their fitting processes.

Table I-1: Brillouin Scattering Studies of Glasses and Glass-Forming Liquids

Material	Ref DB#	Year	Author	Comment
As_2O_3	704	1996	Yannopoulos	
As_2S_3	85	1977	Nemanich	
As_2Se_3	85	1977	Nemanich	
		1986	Cho	
B_2O_3		1974	Bucaro	
	2	1989	Grimsditch	
	6	1988	Yagi	
	230	1988	Grimsditch	
	371	1989	Borjesson	
BaF_2-ZrF_4	6	1988	Yagi	
$BiCl_3$-KCl	265	1983	Torell	
	212	1984	Torell	
CKN	2	1989	Grimsditch	
	3	1982	Torell	
	4	1983	Torell	
	5,	1989	Cheng	
	230	1988	Grimsditch	
	236	1990	Torell	
	275	1991	Tao	
	308	1991	Pavlatou	
	538	1993	Li	
	617	1992	Tao	
$Ca(NO_3)$-H_2O	229	1988	Elmroth	
DMSO-H_2O	9	1987	Bezot	
GeO_2	125	1988	Miller	
GeS_2	85	1977	Nemanich	
$GeSBr_2$	357	1990	Loheider	
$(KCl)_{1-x}(KCN)_x$		1989	Berret	
$LiCl_2$-H_2O	63	1989	Tao	
	69	1972	Hsich	
	250	1991	Tao	
SiO_2		1966	Shapiro	
	32	1989	Mazzacurati	
	297	1982	Lyons	
	440	1991	Kisliuk	
	442	1992	McNeil	
ZnCl2	1	1984	Knape	
	87	1987	Soltwisch	
	301	1991	Grimsditch	
dibutyl phthalate		1982	Lempert	
difluoro tetrachloroethane		1982	Wang	
		1994	Kruger	
dimethyl heptane	43	1984	Carroll	
dimethyl pentane	43	1984	Carroll	
ethanol		1988	Benassi	
	581	1995	Srinivasan	

ethyl benzoate		1975	Bezet
		1986	Oh
glycerol	42	1979	Allain
	94	1968	Pinnow
	161	1968	Knaap
	301	1991	Grimsditch
		1997	Miller
metatoluidine		1998a	Dreyfus
		1998b	Dreyfus
methanol	581	1995	Srinivasan
orthoterphenyl	343	1992	Patkowski
	400	1991	Fischer
	440	1991	Kisliuk
	604	1981	Higashigaki
	602	1992	Kuklik
	448	1987	Wang
		1997	Cummins
α-phenyl o-cresol		1983	Wang
3 phenyl propanol		1983	Wang
polybutylacrylate-dioxane		1992	Brown
polybutyl methacrylate	699	1990	Patterson
polymethyl acralate	7	1971	Huang
polymethyl methacrylate	8	1969	Friedman
		1982	Kato
polypropylene oxide	370	1991	Torell
polypropylene glycol		1975	Huang
	468	1987	Borjesson
		1988	Vanderwal
propylene carbonate	225	1990	Borjesson
	236	1990	Torell
	311	1992	Elmroth
	366	1991	Borjesson
	471	1994	Du
polyurethane		1996	Levelut
poly(vinyl-chloride)		1987	Ng
salol	10	1976	Enright
		1980	Wang
	11	1986	Wang
	428	1993	Dreyfus
	470	1992	Dreyfus
m-tricresylphosphate		1998	Soltwisch
toluene	663	1983	Levy
trimethyl heptane	43	1984	Carroll
trimethylene glycol		1996	Itoh
triphenyl phosphite		1975	Tsay
	12	1989	Miles
	474	1993	Gomperts

Brillouin scattering studies of Ortho-terphenyl (OTP)

Wang and co-workers [44] measured the VV and VH Brillouin spectra of supercooled OTP with different scattering angles. They found that at high temperature, the shear wave is diffusive and gives rise to a dip at the center of the VH spectra. The linear response theory [45] was used to analyze these VV and VH spectra. They found that there were two kinks in the shifted frequency versus temperature curve. These two kinks exist at temperature $T = T_g$ and $T = T_k$, where T_k is defined by Wang as the anomalous temperature, which is above the melting temperature T_m. The temperature-dependent linewidth of the Brillouin modes reaches the maximum at T_k and minimum at T_g [46].

To explain that the Landau-Placzek ratio is sometimes much higher than expected from the theory, Fischer et al. [47] assumed that the supercooled liquid is generally not a thermal equilibrium state as usually assumed, then introduced an order parameter (which depends on thermal history) in the melt whose mean square fluctuations give rise to 'excess' scattering. This was attributed to dynamic clusters.

Recently, Steffen, Patkowski et al. reported a series of studies [25, 48] on depolarized light scattering on OTP and found that OTP samples can be prepared in two states: with and without clusters. Clusters are long range density fluctuations of unknown physical nature, which can be characterized both by static correlation length and by a cluster diffusion coefficient in the static and dynamic light scattering as well as by a high value of the Landau-Placzek ratio. The origin of these clusters is not yet understood.

Brillouin scattering studies of Trimethyl-heptane (TMH)

Carroll and Patterson [49] found that the VH spectrum of TMH is too weak to be observed on the same scale as that used for the VV spectrum. As a result no polarizer was used for the scattered light and the anisotropic scattering was ignored in their analysis. Their results indicated that TMH has very low optical anisotropy. This result will be further discussed in part II where we will analyze the weak depolarized TMH spectra on the basis of MCT.

B. General Aspects of Brillouin Scattering

In the semi-macroscopic view, light scattering is a result of local fluctuations in the dielectric constant of the medium. Molecules in the medium are constantly translating and rotating so that the instantaneous dielectric constant of sub-regions (which depends on the positions and orientations of the molecules) will fluctuate and thus give rise to light scattering. Thus, the fluctuations of dielectric constant can be represented by the density (position) fluctuations and orientational fluctuations. For isotropic liquids, only the density fluctuations exist (temperature fluctuations couple weakly to the dielectric constant and are ignored).

The basic experimental arrangement is shown in Fig.1-1. Light with frequency ω_0 and wavevector $\mathbf{q}_i$ is incident on the sample. The incident light interacts with the molecules of the medium and is scattered through at an angle θ. The scattered light has a frequency distribution $I(\mathbf{q},\omega)$ and a wavevector $\mathbf{q}_s$, where $\mathbf{q} = \mathbf{q}_s - \mathbf{q}_i$.

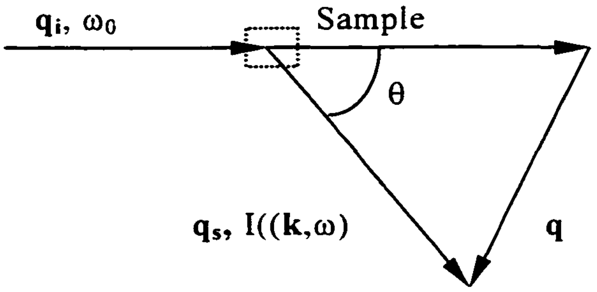

Figure 1-1. Schematic diagram of Brillouin scattering

For Brillouin scattering, the frequency shifts are small in comparison to ω_0 so that the magnitude of **q** is accurately given by

$$q = |\,\mathbf{q}\,| = (4\pi n/\lambda_0)\ \sin(\theta/2), \qquad [1.3]$$

where n is the refractive index of the medium, λ_0 is the wavelength of incident light, and θ is the scattering angle. If the polarization of the incident light is perpendicular to the scattering plane and that of the scattered light is perpendicular or parallel to scattered plane, the polarized (VV) or the depolarized (VH) scattering spectrum is observed. In Brillouin scattering, only the magnitude of **q** is important so that the vector notation is no longer used in this thesis.

Polarized Brillouin scattering

In the polarized spectrum, the scattering arises from density and orientational fluctuations . The depolarized spectrum arises from fluctuations of the anisotropic part of the dielectric tensor associated with the orientational processes, the transverse acoustic waves, and the coupling of orientation and shear wave (there is also weak scattering from dipole-induced-dipole, DID, effects in both VV and VH spectra which will be discussed in part II).

In the long-wavelength limit, the polarized scattering intensity $I_{VV}(q,\omega)$ for a liquid of isotropic molecules due to density fluctuations of the liquid is given by [34]

$$\begin{aligned} I_{VV}(q,\omega) &\propto \int_0^\infty e^{-i\omega t} < \delta\rho^*(q,0)\delta\rho(q,t) > dt \\ &= \int_0^\infty e^{-i\omega t}\Phi(q,t)dt \quad . \\ &= S(q,\omega) \end{aligned} \tag{1.4}$$

where $\delta\rho(q,t)$ is the qth Fourier component of the density fluctuations, $\Phi(q,t)$ is the autocorrelation function (or intermediate scattering function) of density fluctuations, and the dynamic structure factor $S(q,\omega)$ is the Fourier transform of $\Phi(q,t)$.

Assumptions

With the following assumptions [33] and the hydrodynamic laws, we can establish the relationship between the fluctuations and the intensity of scattered light.

- The liquid is considered as a continuous medium; it is locally homogenous, isotropic, viscous, and thermally conducting.
- The local thermodynamic conditions are completely specified by three state variables related to the equation of state.

- Local thermodynamic equilibrium applies.
- The irreversible production of entropy by dissipation is accounted for.
- Transport processes are governed by linear laws where the transport coefficients are considered as constant parameters.

C. Simple Liquids of Isotropic Molecules

Density fluctuations

First, we consider simple liquids where density fluctuations can be described by the hydrodynamic equations and in which the internal degrees of freedom do not contribute to the relaxation processes. Orientational fluctuations are ignored for the isotropic molecules. The transverse velocity does not couple to the optical properties, so that the viscous shear modes do not contribute to the scattered spectrum and there is therefore no depolarized spectrum ($I_{VH} = 0$).

To describe the density fluctuations, the pressure fluctuations and either the temperature or entropy fluctuations can be used as the independent variables. Since sound propagation is an adiabatic process, it is convenient to decompose the density fluctuations into pressure fluctuations at constant entropy and entropy fluctuations at constant pressure.

Brillouin spectrum

The frequency of the light scattered by the fluctuations at constant entropy (thermal sound waves or phonons) is shifted by an amount proportional to the velocity of the sound waves. Two peaks are observed because scattering can occur from waves traveling in opposite directions but at the same speed as first predicted by Brillouin. These peaks are broadened somewhat because of the dissipative processes which damp out the waves.

The light scattered by the fluctuations at constant pressure is not shifted in frequency although it is broadened somewhat due to the thermal dissipative processes which damp out these fluctuations, Fig. 1-2.

The normalized spectral distribution function

The detailed derivation of the spectrum for simple liquids was first presented by Mountain [35]. Following Mountain, it is convenient to define a normalized spectral distribution function $\sigma(q,\omega)$ by

$$\sigma(q,\omega) = S(q, \omega) / S(q), \qquad [1.5]$$

where $S(q, \omega)$, the dynamic structure factor is proportional to the light scattering spectrum $I(q, \omega)$ and $S(q)$ is the static structure factor given by

$$S(q) = \frac{1}{2\pi}\int_{-\infty}^{\infty} d\omega S(q,\omega) \ . \qquad [1.6]$$

Small fluctuations

To construct $\sigma(q,\omega)$, we assume that fluctuations around equilibrium are small

$$\rho = \rho_0 + \rho_1 \ ,$$

$$v = v_1 \ , \qquad [1.8]$$

$$T = T_0 + T_1 \ ,$$

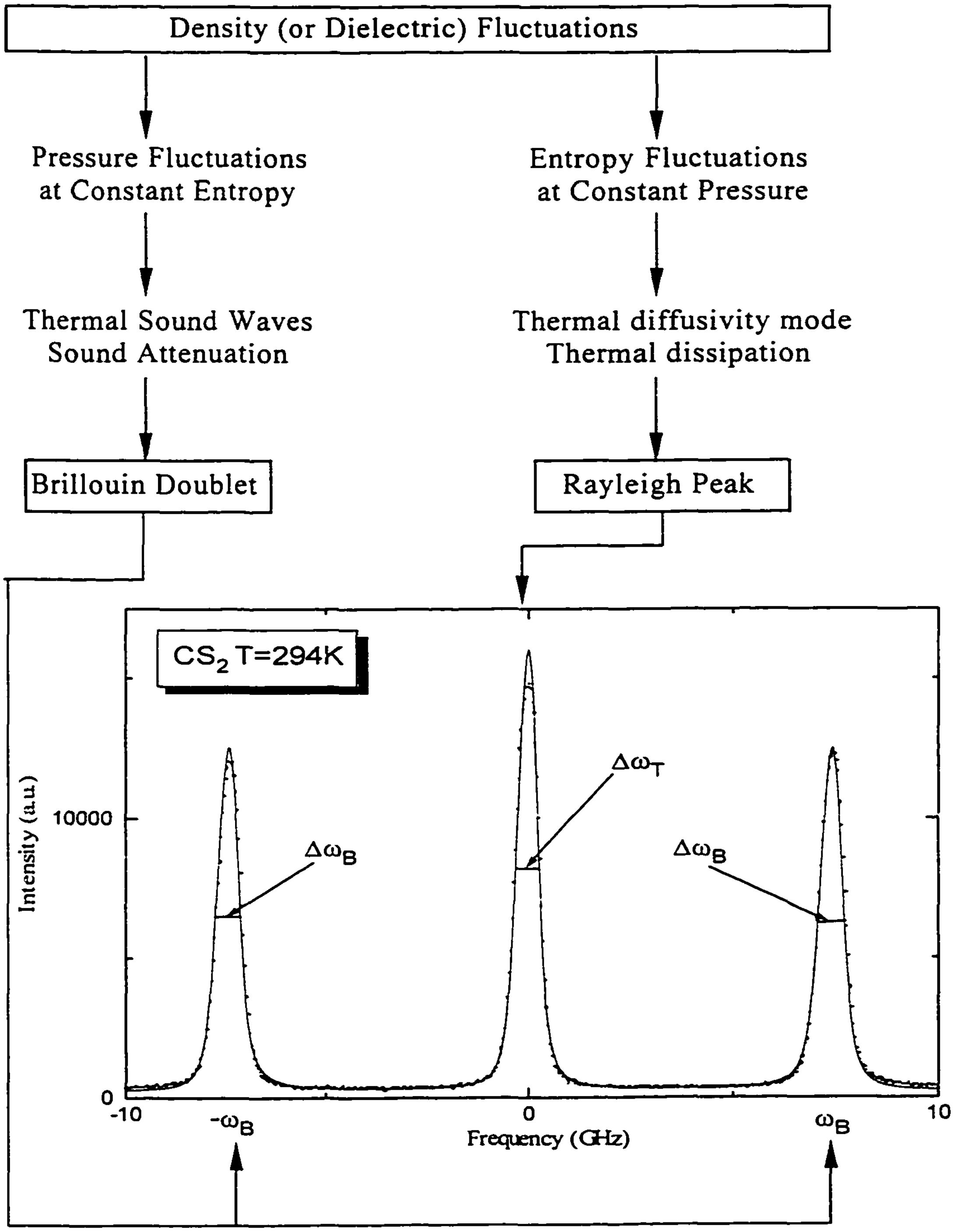

Figure 1-2. Representation of the Brillouin scattering spectrum of simple liquids [33] (The quantities ω_B, $\Delta\omega_B$, and $\Delta\omega_T$ are given in section 2-A)

where ρ_1, v_1, and T_1 are the fluctuations of the density ρ, velocity v, and temperature T at the equilibrium values ρ_0, $v_0 = 0$, and T_0, respectively. The higher order terms are neglected. Since the fluctuations are assumed to be very small, the variables satisfy $\rho_0 >> \rho_1$ and $T_0 >> T_1$.

Linearized hydrodynamic equations(non-relaxing)

We also assume that the density fluctuations are governed by the three basic laws of hydrodynamics: (1) the continuity equation which expresses the conservation of matter; (2) the force equation or the longitudinal part of the Navier-Stokes equation which expresses the conservation of momentum; (3) the energy-transport equation which expresses the conservation of energy. With the assumptions discussed before, these three linearized equations are:

i) the continuity equation:

$$\frac{\partial \rho_1}{\partial t} + \rho_0 \mathrm{div} \cdot \bar{v} = 0 \ . \qquad [1.9]$$

ii) the longitudinal part of the Navier-Stokes equation:

$$\rho_0 \frac{\partial \bar{v}}{\partial t} + \frac{C_0^2}{\gamma} \mathrm{grad}(\rho_1) + \frac{C_0^2 \beta \rho_0}{\gamma} \mathrm{grad}(T_1) - (\frac{4}{3}\eta_S + \eta_B) \mathrm{graddiv} \cdot \bar{v} = 0 , \qquad [1.10]$$

and

iii) the energy-transport equation:

$$\rho_0 c_V \frac{\partial T_1}{\partial t} - \frac{c_V(\gamma - 1)}{\beta} \frac{\partial \rho_1}{\partial t} - \lambda \nabla^2 T_1 = 0 , \qquad [1.11]$$

where C_0 is the low frequency limit of sound velocity, γ is the ratio of the specific heat at constant pressure c_P to the specific heat at constant volume c_V, β is the thermal expansion coefficient, η_S and η_B are shear and bulk viscosities, and λ is the thermal conductivity.

These three linearized hydrodynamic equations can be solved by Laplace transformation on time and Fourier transformation on space. Then the ensemble averages for the initial states are evaluated and noting that terms in $<\rho^*(q)\rho(-q)>$ and $<T(q)\rho(-q)>$ vanish because of statistical independence we obtain (for more details, see reference [34]).

$$\frac{<\rho(q,s)\rho(-q)>}{<\rho(q)\rho(-q)>}=\frac{s^2+(a+b)q^2s+abq^4+C_0^2(1-1/\gamma)q^2}{s^3+(a+b)q^2s^2+(C_0^2+abq^4)s+aC_0^2q^4/\gamma}, \qquad [1.12]$$

where $a = \lambda/\rho_0 c_V$ and $b = (4/3\eta_S+\eta_B)/\rho_0$. The spectral distribution function $\sigma(q,\omega)$ can be obtained from Eq. [1.12]

$$\begin{aligned}\sigma(q,\omega)&=2\,\mathrm{Re}\left[\frac{<\rho(q,s)\rho(-q)>}{<\rho(q)\rho(-q)>}\right]_{s=i\omega}\\&=2\,\mathrm{Re}\left[\frac{s^2+(a+b)q^2s+abq^4+C_0^2(1-1/\gamma)q^2}{s^3+(a+b)q^2s^2+(C_0^2+abq^4)s+aC_0^2q^4/\gamma}\right]_{s=i\omega}\end{aligned} \qquad [1.13]$$

Equation [1.13] can be represented as

$$\begin{aligned}\sigma(q,\omega)&=2\,\mathrm{Re}\left[\frac{F_2(i\omega)}{G_3(i\omega)}\right]\\&=\frac{N_1D_1+N_2D_2}{D_1^2+D_2^2}\end{aligned} \qquad [1.14]$$

where N_1, N_2, D_1, and D_2 are polynomials and will be defined later. $F_2(i\omega)$ and $G_3(i\omega)$ are second and third order polynomials, respectively. If the three roots of the third order polynomial $G_3(i\omega)$ are well separated, then the spectral distribution function can be approximately separated into the sum of three Lorentzians: One unshifted thermal diffusion (Rayleigh) component and two shifted Brillouin components centered at $\omega = \pm vq$, where v is the velocity of adiabatic sound waves and q is the scattering wavevector determined by Eq.(1.3).

Fig. 1-2 demonstrates the result of this calculation, while Fig. 1-3. shows a set of typical polarized Brillouin spectra of TMH at different temperatures.

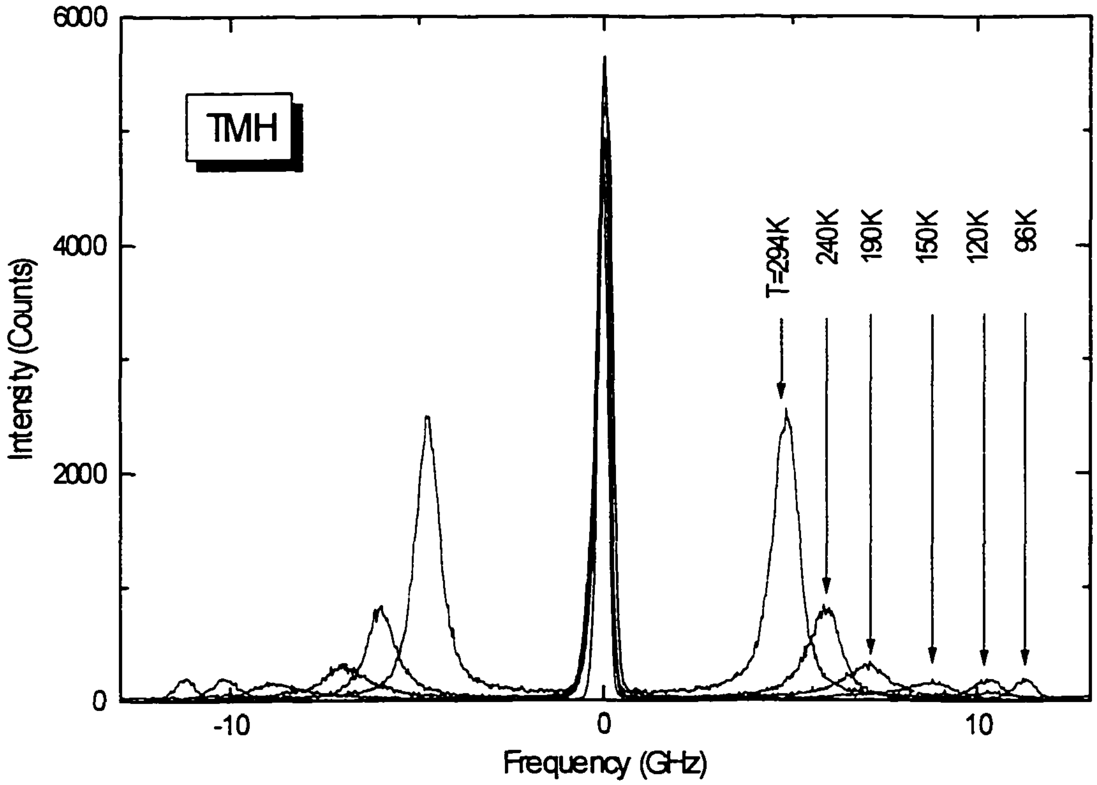

Fig.1-3. The VV spectra of TMH at T= 294, 240, 190, 150, 120, and 96K

D. Complex Liquids

Relaxation function

For complex liquids, where relaxation effects are present, it is necessary to modify the hydrodynamic equations, Eqs. [1.9], [1.10], and [1.11]. Mountain [8] introduced a frequency-dependent viscosity function b'(ω) into the longitudinal part of the Navier-Stokes equation to represent the coupling of internal degrees of freedom of the molecules to the translational degrees of freedom of the liquid. with this modification, b (of Eq.[1.12]) becomes $b = (4/3\eta_s+\eta_b) + b'(\omega) = b_0 + b'(\omega)$. In reference [8], Mountain represented the frequency-dependent viscosity function b'(ω) by a single-relaxation time function:

$$b'(\omega) = \frac{b_1}{1+i\omega\tau}, \qquad [1.15]$$

where $b_1 = (C_\infty^2 - C_0^2)\tau$, C_∞ is the sound velocity in the high frequency limit, and τ is the relaxation time. Zwanzig [50] showed that the frequency-dependent viscosity described by Eq.[1.15] can be interpreted as any adiabatic loss mechanism in the liquid if the time scale of energy transport is much longer than the thermal relaxation time.

Linearized hydrodynamic equations(relaxing)

The three linearized hydrodynamic equations with this modification are given by

i) the continuity equation

$$\frac{\partial \rho_1}{\partial t} + \rho_0 \mathrm{div} \cdot \bar{v} = 0, \qquad [1.16]$$

ii) the longitudinal part of the Navier-Stokes equation

$$\begin{aligned} \rho_0 \frac{\partial \bar{v}}{\partial t} &= -\frac{C_0^2}{\gamma} \mathrm{grad}(\rho_1) - \frac{C_0^2 \beta \rho_0}{\gamma} \mathrm{grad}(T_1) \\ &\quad + (\frac{4}{3}\eta_S + \eta_B) \mathrm{graddiv} \cdot \bar{v} + \int_0^t \eta'(t - t') \mathrm{graddiv}[\bar{v}(t')] dt' \end{aligned}, \qquad [1.17]$$

iii) the energy-transport equation

$$\rho_0 c_V \frac{\partial T_1}{\partial t} - \frac{c_V (\gamma - 1)}{\beta} \frac{\partial \rho_1}{\partial t} - \lambda \nabla^2 T_1 = 0, \qquad [1.18]$$

with $\eta'(t) = \eta_0 e^{-t/\tau}$.

Third and fourth order polynomials

By using the same procedures discussed for simple liquids, these three linearized hydrodynamic equations can be solved and the dynamic structure factor is given by

$$S(q,\omega) = S(k)\, 2\, \mathrm{Re}\, [F_3(s) / G_4(s)]_{s = i\omega} \qquad [1.19]$$

or equivalently by

$$\sigma(q,\omega) = 2\, \mathrm{Re}\, [F_3(i\omega) / G_4(i\omega)] \qquad [1.20]$$

where $F_3(i\omega)$ and $G_4(i\omega)$ are third and fourth order polynomials in $i\omega$. Eq.[1.20] also can be approximated by the sum of four Lorentzians (the Rayleigh component, the Brillouin doublet, and a new central component) using the same method of residues (partial fractions) with factorization of the denominator. The fourth component is a quasi-elastic mode, called the Mountain mode, and has linewidth ~ $1/\tau$, associated with the internal relaxation process. We will discuss the use of these different expressions for the spectral distribution function $\sigma(k,\omega)$ to analyze experimental data in chapter 2.

In a subsequent paper, Mountain [36] introduced an additional coordinate ξ to represent the internal relaxing degree of freedom into the linearized hydrodynamic equations, Eqs.[1.8], [1.9], and [1.10] with frequency-independent transport coefficients. He considered two cases: In the first case, the internal variable couples only on the local temperature (thermal relaxation); In the second case, the internal variable couples only on the local density (structural relaxation). Comparison with the Eq.[1.19] was made in these two limiting cases. He found that the two calculations gave similar but not identical results in the former case while the two calculations yielded identical results for structural relaxation.

The distinction between thermal relaxation and structural relaxation was further studied by Allen-Demoulin et al. [51], who analyzed the general mixed coupling case and explored the interaction of the Rayleigh and Mountain modes near the liquid-glass transition.

Complex liquids with anisotropic molecules

When linearly polarized light is scattered by a liquid with anisotropic molecules, the scattered light consists of both polarized (VV) and depolarized (VH) parts. This scattered light is caused by fluctuations of the local temperature, density, and molecular orientation, and by dipole-induced-dipole (DID) effects. Because of the weak dependence of the molecular polarizability on temperature, the first effect can be neglected. We also ignore the weak DID effects and assume initially that density and orientational fluctuations are uncorrelated.

The dynamic structure factor $S_{ISO}(q,\omega)$

The dynamic structure factor $S_{VV}(q,\omega)$ of the VV spectrum contains the contributions of the density fluctuations (the isotropic part) and of the orientational fluctuations (the anisotropic part), while the dynamic structure factor $S_{VH}(q,\omega)$ of the VH spectrum contains solely the contributions of the orientational fluctuations (the anisotropic part) [52]. The dynamic structure factor $S_{ISO}(q,\omega)$ of the isotropic spectrum is usually assumed to be given by:

$$S_{ISO}(q,\omega) = S_{VV}(q,\omega) - k\, S_{VH}(q,\omega), \qquad [1.21]$$

where k is a geometrical factor which is determined by symmetries in the molecular polarizability tensor. Usually, k is taken as 4/3 [34]. The more complex case is that density and orientational fluctuations are coupled and the DID (the second order density fluctuation) effects can not be neglected. Then, $S_{VH}(q,\omega)$ is caused by density and orientational fluctuations and their coupling.. In this case, Eq.[1.21] is no longer valid.

Unfortunately, so far, there is no theory or experiment which can clearly separate these two fluctuations. Fig. 4a and 4b show the polarized (VV),

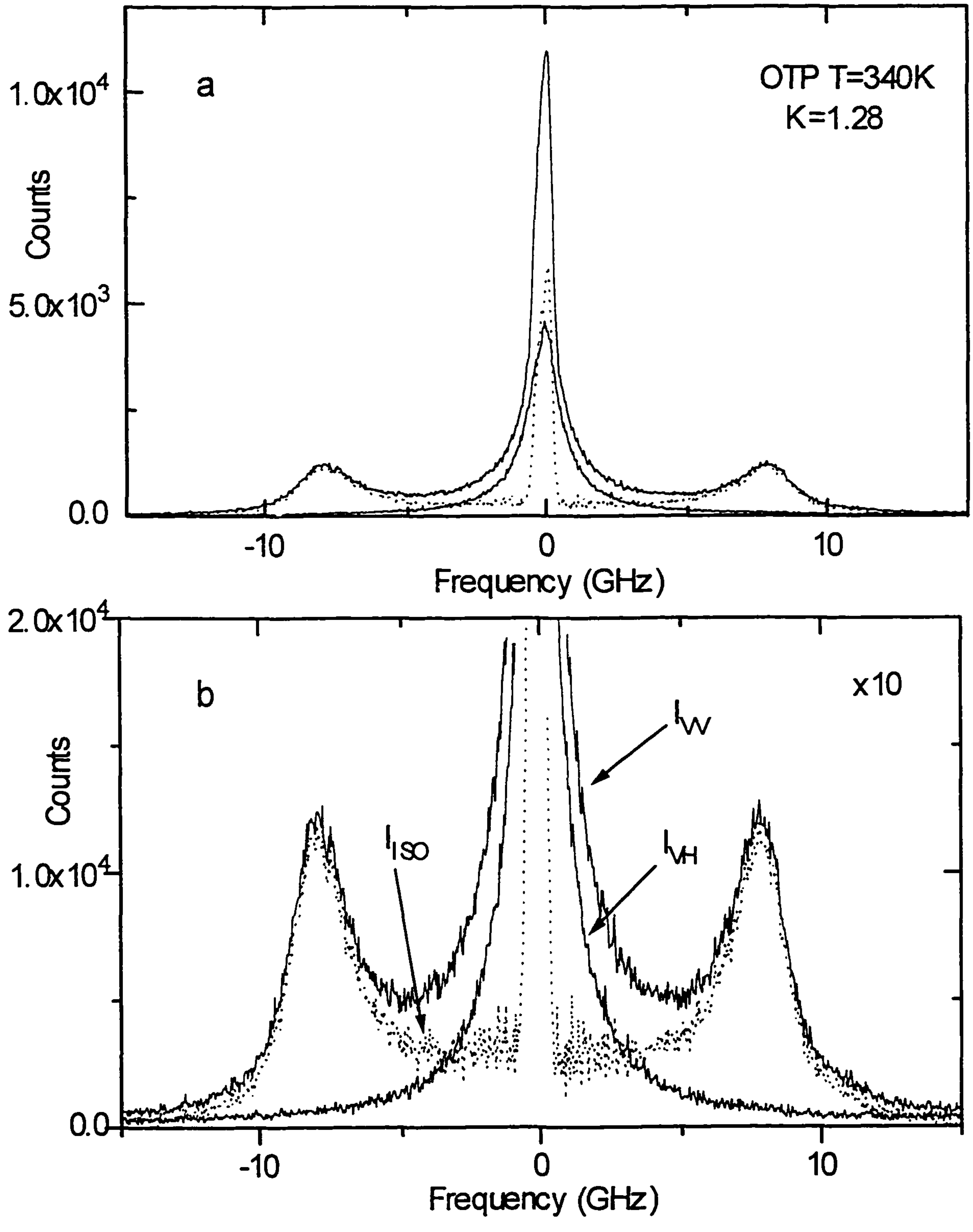

Figure 1-4 The VV, VH, and isotropic spectra of OTP at T=340K

depolarized (VH), and isotropic spectra of OTP at T = 340K, where the isotropic spectrum was calculated with Eq.[1.21] with the factor f = 1.28 determined from the ratio of VV to VH spectra at frequencies far above the Brillouin line where only orientational and DID scattering should be significant. Note that the Mountain component of the isotropic spectrum has almost vanished.

E. Depolarized Brillouin spectrum

In a liquid consisting of optically anisotropic molecules, many new features arise in the scattering spectra. The most important feature is the appearance of depolarized components caused by orientational dynamics, and the coupling between rotational motion and transverse shear modes.

The central dip

It was found that in the high temperature region ($\Gamma >> q^2\eta_0/\rho$, where Γ is the rate of molecular reorientation and η_0 is the zero frequency shear viscosity) depolarized spectra of some liquids (such as anisaldehyde, quinoline, salol) exhibit a novel central peak with a narrow central dip, Fig.1-5a. The existence of this doublet had been first predicted by Leontovich (1941) [53] using hydrodynamic theory, assuming that local stress is induced by a transverse shear wave due to the collective reorientation of individual molecules. Rytov (1957) [37] also predicted such a spectrum using a macroscopic phenomenological theory. This new feature was first extensively studied in experiments by Fabelinskii et al.[54] and by Stegeman and Stoicheff [38-39].

Transverse modes

With a smaller reorientation rate ($\Gamma \sim q^2\eta/\rho$), the shear wave dip is not present in the depolarized spectrum and the spectrum can not be described by a Lorentzian function, Fig. 1-5b. Furthermore in the low temperature region where $\Gamma \ll q^2\eta/\rho$, the depolarized spectrum consists of a shifted doublet centered at $\omega_T = v_T q$, due to the propagation of transverse waves, where v_T is the velocity of the transverse acoustic waves, with very weak intensity and a narrow-intense central component due to the orientational fluctuations, figure 1-5c.

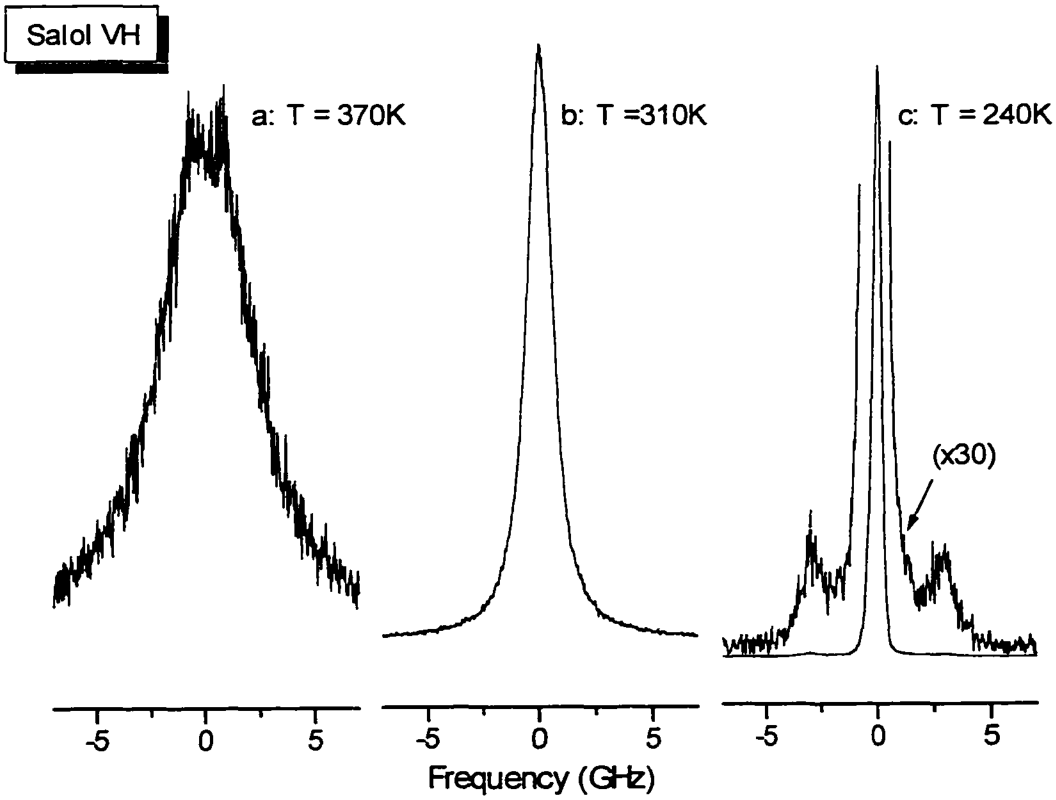

Figure 1-5 The VH spectra of salol at T=370, 310, and 240K.

Depolarized spectrum

In a coordinate system, Fig. 1-6, where the **Y** axis indicates the polarization of incident light and the scattering vector q is along the **Z** axis, the polarized and depolarized spectra observed at scattering angle θ is given by [34]

$$S_{VV}(q,\omega) = S_{YY}(q,\omega) \qquad [1.22a]$$

$$S_{VH}(q,\omega) = S_{YZ}(q,\omega)\cos^2\frac{\theta}{2} + S_{YX}(q,\omega)\sin^2\frac{\theta}{2} , \qquad [1.22b]$$

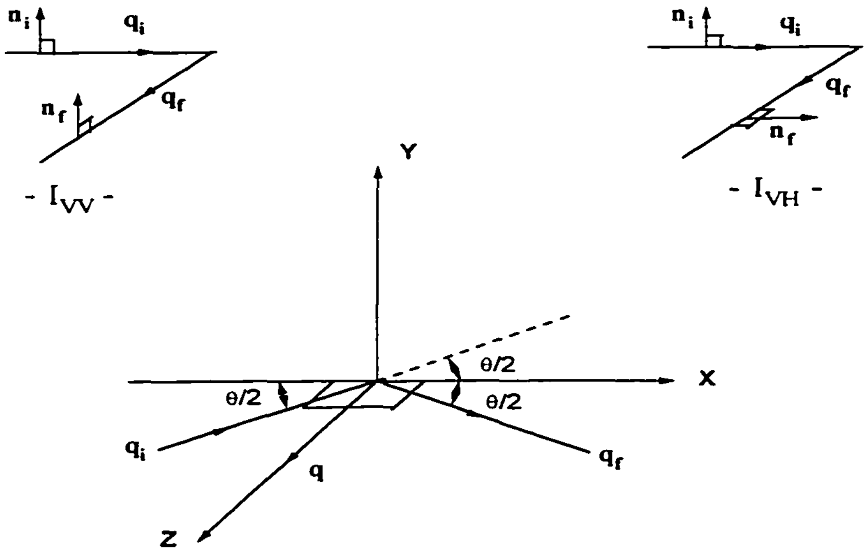

Fig. 1-6 Schematic diagram of scattering geometry

where S_{YY}, S_{YZ} and S_{YX} are the Fourier transforms of the polarizability correlation functions, $<\alpha_{YY}(q,t)\alpha^*_{YY}(q,0)>$, $<\alpha_{YZ}(q,t)\alpha^*_{YZ}(q,0)>$ and $<\alpha_{YX}(q,t)\alpha^*_{YX}(q,0)>$, respectively. Any angular dependence of the depolarized (VH) spectrum is due to the difference in the dynamic processes governing the time dependence of the correlation functions $<\alpha_{YZ}(q,t)\alpha^{*}_{YZ}(q,t)>$ and $<\alpha_{YX}(q,t)\alpha^{*}_{YX}(q,0)>$.

From general symmetry considerations, the reorientational motion modulating $\alpha_{yz}(q,t)$ will couple to the collective transverse velocity of the liquid, while $\alpha_{yx}(q,t)$ will not. (Because for q along the Z axis, the two possible shear waves are V_X and V_Y, so the mode symmetries are XZ and YZ.) This coupling is dynamic and gives rise to a shear wave dip at the center of the high temperature depolarized scattering.

Keyes-Kivelson [55] and Anderson-Pecora [56] (see Berne and Pecora [34]) calculated the depolarized scattering spectrum using hydrodynamic equations which include the orientational effects. They found that the depolarized spectrum is given by

$$I_{VH}(q,\omega) \propto \frac{\Gamma[\omega^2 + (\upsilon_S q^2)^2(1-R)\cos^2\theta/2]}{[\omega^2 - \upsilon_S q^2\Gamma]^2 + \omega^2[\Gamma + \upsilon_S q^2(1-R)]^2} + \frac{\Gamma}{\omega^2 + (\Gamma)^2}\sin^2\frac{\theta}{2} \,. \qquad [1.23]$$

In the limit of $\frac{\upsilon_S q^2}{\Gamma} << 1$, Equation [1.23] reduces to the sum of two Lorentzians

$$I_{VH} \propto \frac{\Gamma}{\omega^2 + (\Gamma)^2} - R\left[\frac{\upsilon_S q^2}{\Gamma}\right]\frac{\upsilon_S q^2}{\omega^2 + (\upsilon_S q^2)^2}\cos^2\frac{\theta}{2} \,, \qquad [1.24]$$

where Γ is the linewidth of the depolarized back-scattering spectrum, θ is the scattering angle, $\upsilon_S = \eta_S/\rho$ is the kinematic shear viscosity, and $R<1$ is a parameter which is determined by the dynamic coupling between transverse waves and orientational dynamics [10].

From Eq.[1.24], it is clear that the corresponding spectrum consists of a broad band with linewidth Γ with a narrow Lorentzian subtracted that leads to a dip with linewidth $\upsilon_S q^2$. The depth of the dip is proportional to $(R/\Gamma)\cos^2\theta/2$ at $\omega=0$. When $R=0$, the second Lorentzian vanishes and the spectrum reduces to a single Lorentzian with linewidth Γ due to the orientational dynamics.

The Andersen-pecora theory leading to Eq. [1.23] provides excellent fits to depolarized light scattering spectra at high and moderate temperatures where $\Gamma \geq q^2\eta/\rho$. But at low temperatures where propagating transverse acoustic modes appear, the theory fails. This is because at low temperatures viscoelastic effects must also be included.

Inclusion of viscoelastcity in the analysis of depolarized spectra has been presented in a series of papers by Wang and co-workers [57-59] and also, by a method based on including additional variables, by Kivelson [9-10, 60]. Recently, Pick and co-workers have reanalyzed this problem, finding more general expressions for the depolarized and polarized spectra [61]. This aspect of Brillouin scattering spectroscopy is currently under study in our laboratory but will not be discussed further in this thesis.

Figure 1-7 shows the VH spectra of PC and OTP at high and low temperatures. At high temperatures, no central dip was found in either the PC or OTP spectra. But at low temperatures, transverse modes were observed in both the PC and OTP spectra.

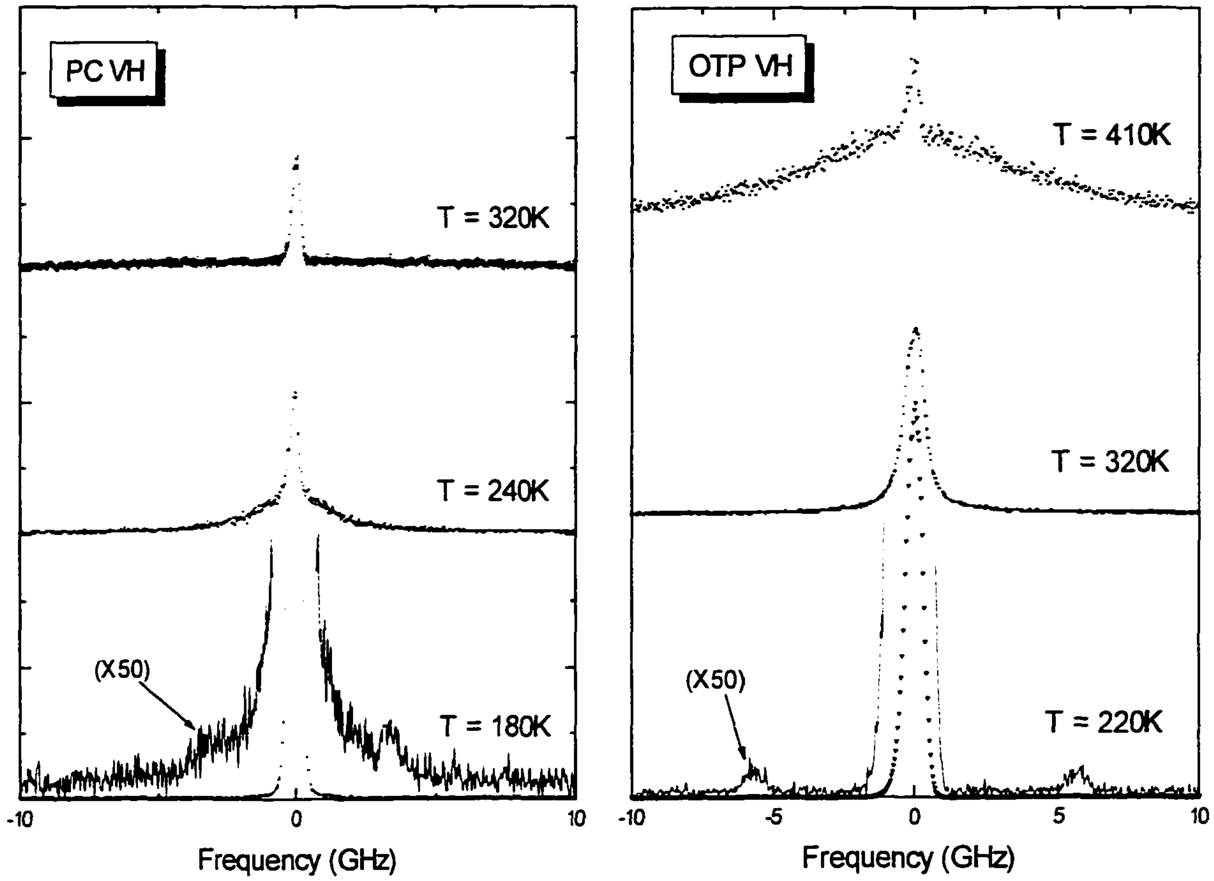

Figure 1-7 The $\theta=90^0$ VH spectra of PC and OTP

DID effects

If DID effects (second order density fluctuations) are considered in the scattering spectra, the situation becomes yet more complex. There is no theory of Brillouin scattering which includes this effect. In the experiments, the problem becomes how to separate the orientational fluctuations from the density fluctuations. Kivelson [60] proposed that the orientational fluctuations give rise to the 'narrow' component in the depolarized spectrum while the density fluctuations give rise the 'broad' component, but this identification is open to serious question. An effort to separate the two effects for the molecular glass-former salol indicated that the total scattered intensity due to orientational fluctuations is about 30 times larger than the DID contribution [62].

Chapter 2

Analysis of Brillouin Spectra

In this chapter, we review several approaches to the analysis of Brillouin spectra using the polarized (VV) and depolarized (VH) spectra of Propylene Carbonate (PC) at T=240K as an example. In Figure 2-1, we show a set of typical polarized Brillouin spectra of PC (T_g = 160K, T_m = 218K) for temperatures between 180 and 290K. With decreasing temperature, The Brillouin components move to higher frequency and the width of the Brillouin components first broadens, goes through a maximum, and again narrows. At intermediate temperatures, an additional central component appears between the Brillouin components.

A. Simple Liquids of Isotropic Molecules

Three Lorentzians (Brillouin and Landau-Placzek)

For simple liquids, as discussed in chapter 1, the Brillouin spectrum consists approximately of three Lorentzians forming a symmetric triplet: the two Brillouin components produced by scattering from propagating sound waves are centered (relative to the frequency of the incident light) at $\pm\ \omega_B$, and their half-width $\Delta\omega_B$ is the sound-absorption coefficient. The central unshifted component, produced by the non-propagating temperature (or entropy) fluctuations, has half-width $\Delta\omega_T$ determined by the thermal diffusion coefficient. The light-scattering spectrum is given by

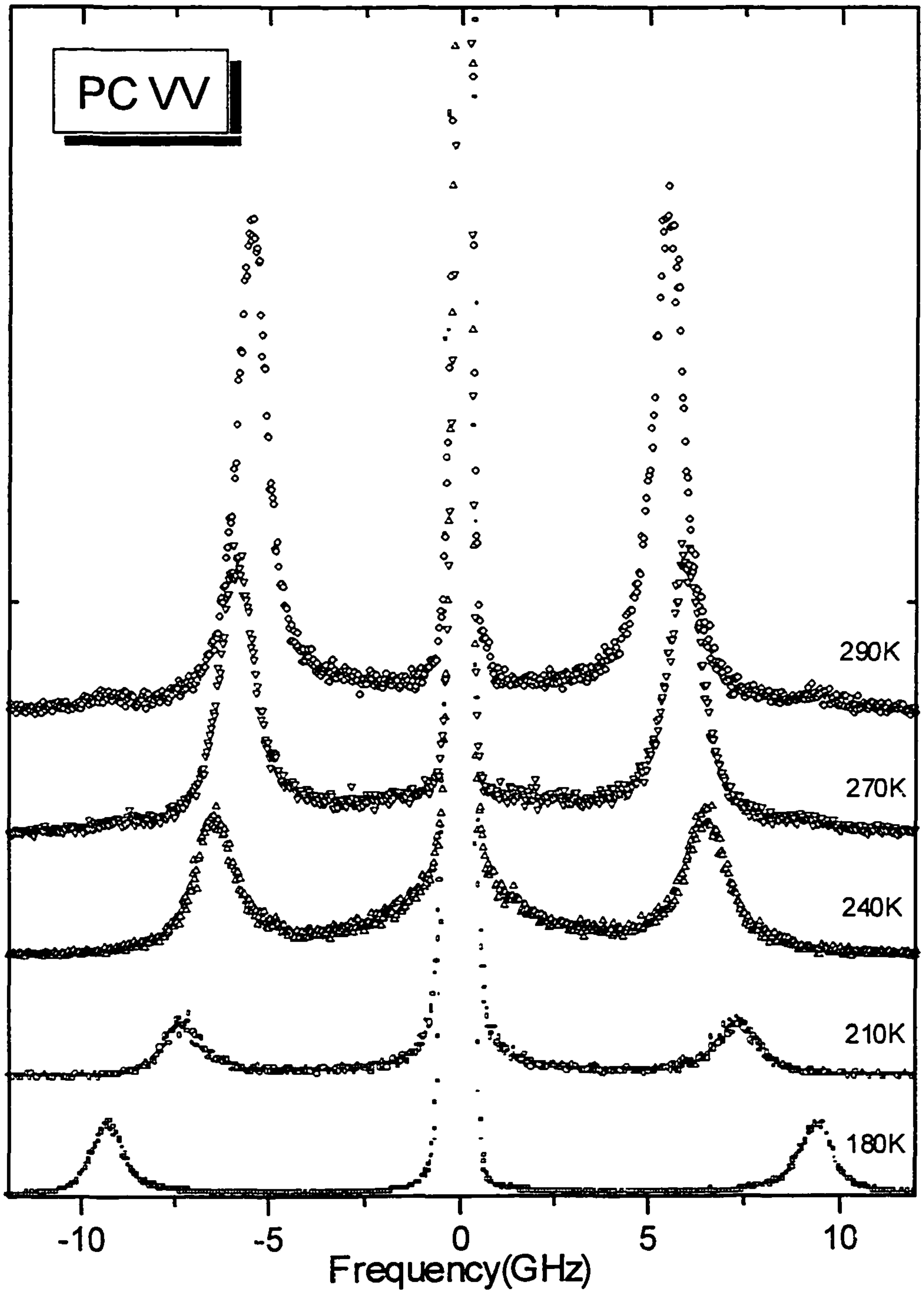

Figure 2-1 The 90^0 polarized spectra of PC at different temperatures, from top T = 290 (◇), 270 (▽), 240 (△), 210 (○), 180 (□)K.

$$I(\omega) = I_T \frac{\Delta\omega_T}{\Delta\omega_T^2 + \omega^2} + I_B \left[\frac{\Delta\omega_B}{\Delta\omega_B^2 + (\omega - \omega_B)^2} + \frac{\Delta\omega_B}{\Delta\omega_B^2 + (\omega + \omega_B)^2} \right], \qquad [2.1]$$

where I_T and I_B are the integrated intensities of the thermal diffusion mode and the Brillouin modes, respectively. The temperature-dependent values of ω_B and $\Delta\omega_B$ can be related to the thermodynamic parameters as discussed in the following sections, for example, ω_B and $\Delta\omega_B$ can be used to analyze coupling of acoustic modes to structural relaxation [34].

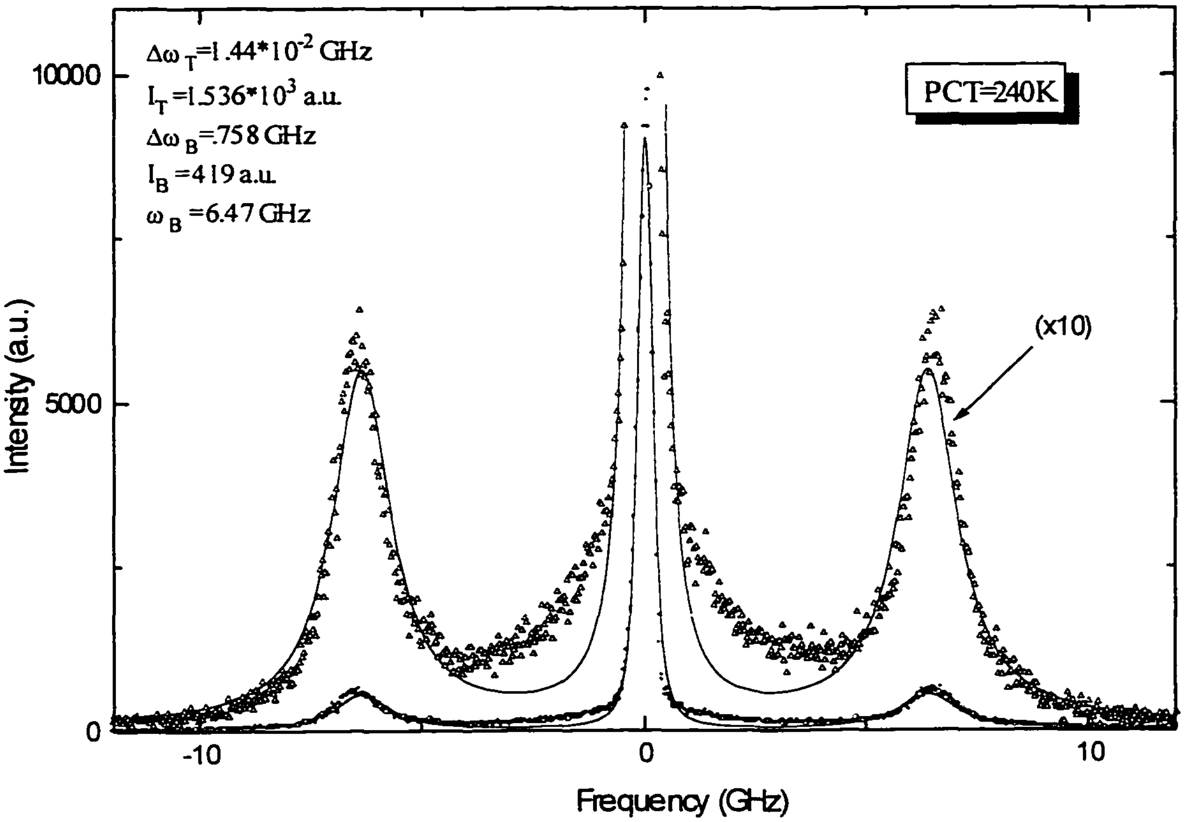

Figure 2-2 The 90^0 VV spectrum of PC at 240K fit by Eq.[2.1]

In Figure 2-2, the VV spectrum of PC at 240K was fit by Eq.[2.1]. The fitting parameters are I_T, $\Delta\omega_T$, I_B, ω_B, and $\Delta\omega_B$. The non-linear least squares fit method (including convolution with the experimentally determined instrumental function) was used in all of our data analysis procedures. It is evident in Fig.2-2 that the fitting curve is much lower than the spectrum in the central regions between the Brillouin components and the central component.

Hydrodynamic theory

As discussed in section 1-C, the hydrodynamic theory shows that, for simple liquids of isotropic molecules, the normalized light-scattering spectrum $\sigma(q,\omega)$ can be written as [35]

$$\sigma(q,\omega) = 2\,\mathrm{Re}\left[\frac{s^2+(a+b)q^2s+abq^4+C_0^2(1-1/\gamma)q^2}{s^3+(a+b)q^2s^2+(C_0^2q^2+abq^4)s+aC_0^2q^2/\gamma}\right]_{s=i\omega}, \qquad [2.2]$$

where $a=\lambda/\rho_0c_V$ (λ = thermal conductivity, ρ_0 = average density), C_0 is the low-frequency adiabatic sound velocity , $b=(4/3\eta_S+\eta_B)/\rho_0$ (η_S and η_B are the shear and bulk viscosities), q is the scattering wavevector, γ is the ratio of specific heats c_P/c_V , λ_0 is the wavelength of incident light, and θ is the scattering angle.

Equivalently, Eq.(2.2) can be expressed as

$$\sigma(q,\omega) = 2\frac{N_1D_1+N_2D_2}{D_1^2+D_2^2}, \qquad [2.3]$$

where

$$\begin{aligned} N_1 &= -\omega^2+abq^4+C_0^2q^2(1-1/\gamma)\\ N_2 &= \omega(a+b)q^2\\ D_1 &= -\omega^2(a+b)q^2+C_0^2aq^4/\gamma\\ D_2 &= \omega(-\omega^2+C_0^2q^2+abq^4) \end{aligned} \qquad [2.4]$$

The spectrum $I(q,\omega)$ is given by

$$I(\omega) = I_0\sigma(q,\omega). \qquad [2.5]$$

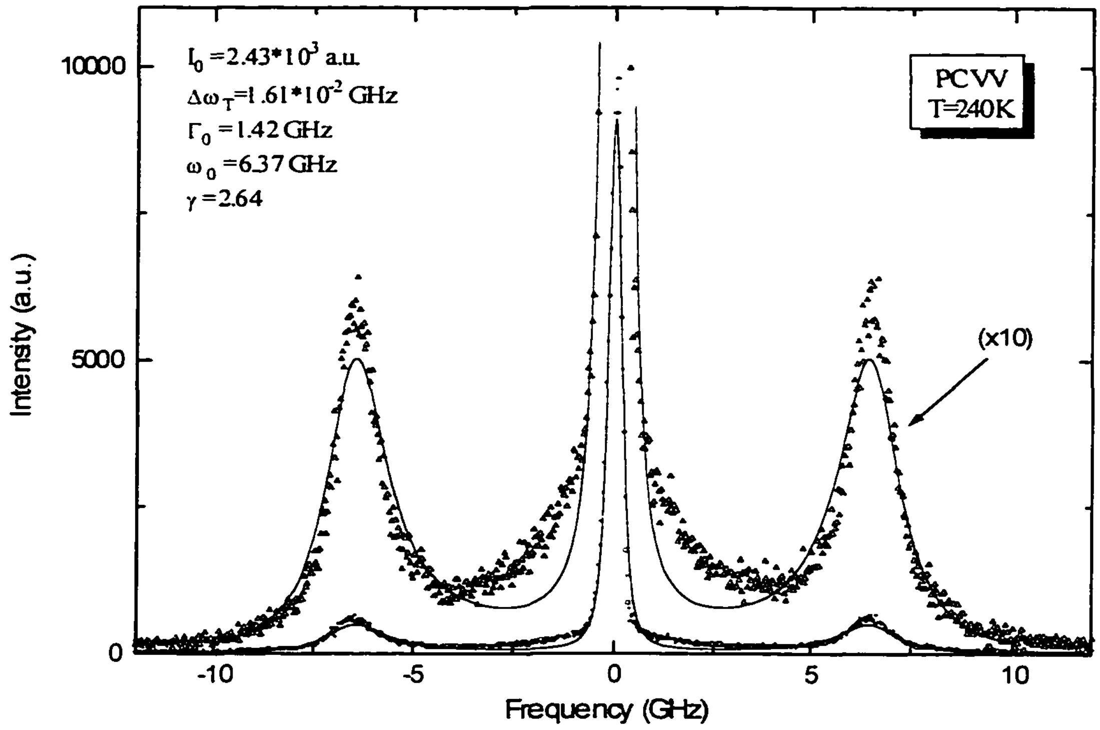

Figure 2-3 The 90^0 VV spectrum of PC at 240K fit by Eq.[2.5]

Figure 2-3 shows the VV spectrum of PC at 240K fit by Eq.[2.5]. The fitting parameters are I_0 , aq^2, bq^2 , C_0q, and γ. There is a slight improvement compared with Fig.2-2, but the theoretical fit curve is still lower than the experimental spectrum in the central region. This result indicates that there is an extra component in the spectrum which is not included in either Eq.[2.1] or Eq.[2.3]. That means that we cannot treat PC as a simple liquid of isotropic molecules.

Using the method of residues, with approximate factorization of the denominator of Eq.[2.3] to order q^2, leads to the three Lorentzians approximation for the spectral distribution function $\sigma(q,\omega)$

$$\sigma(q,\omega)=\frac{c_p-c_v}{\pi c_p}\frac{2\lambda q^2/\rho_0 c_p}{(\lambda q^2/\rho_0 c_p)^2+\omega^2}+\frac{c_v}{2\pi c_p}\left[\frac{\Gamma q^2}{(\Gamma q^2)+(\omega+C_0 q)^2}+\frac{\Gamma q^2}{(\Gamma q^2)+(\omega-C_0 q)^2}\right] \quad [2.6]$$

and

$$\Gamma=\frac{1}{2}\left[\frac{4/3\eta_S+\eta_B}{\rho_0}+\frac{1}{\rho_0}\left(\frac{\lambda}{c_v}-\frac{\lambda}{c_p}\right)\right] \quad [2.7]$$

Comparing Eq.[2.5] with Eq. [2.1], we have

$$I_B=\frac{I_0 c_V}{2\pi c_p} \quad [2.8]$$

$$\omega_B=\pm C_0 q \quad [2.9]$$

$$\Delta\omega_B=\Gamma q^2 \quad [2.10]$$

$$I_T=\frac{I_0(c_P-c_V)}{\pi c_p} \quad [2.11]$$

$$\Delta\omega_T=D_T q^2, \quad [2.12]$$

and $D_T = \lambda/\rho_0 c_p$ is the thermal diffusion coefficient.

The Landau-Placzek ratio

The ratio of the integrated intensities of the thermal diffusion mode (I_T) to that of the combined Brillouin modes ($2I_B$), the Landau-Placzek ratio, is given by

$$I_T / 2I_B = \gamma - 1 \quad [2.13]$$

If $\gamma=1$ ($c_P = c_V$), the thermal diffusion mode will disappear. Figure 2-4 shows the Brillouin spectrum of water at T=294K ($c_P \sim c_V$). Note that the thermal diffusion mode is

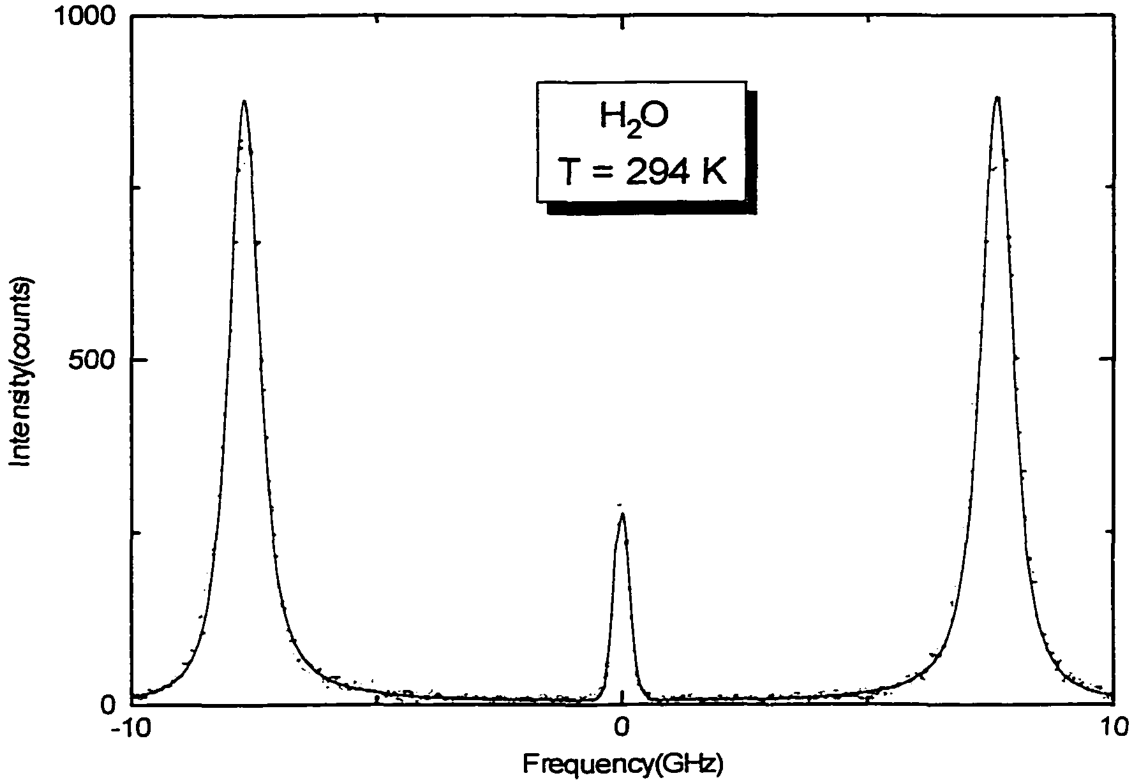

Figure 2-4 Polarized Brillouin spectrum of H_2O

very weak (It completely disappears at T = 4^0C where c_P=c_V [63-64]). The solid line is the three Lorentzians fitting curve.

B. Complex Liquids of Isotropic Molecules

Mountain's [M8, M9] generalization of the hydrodynamic approach of section 2-A, includes a frequency-dependent term in the longitudinal viscosity (see section 1-D). While the relaxing viscosity was originally proposed to represent internal molecular degrees of freedom, Mountain's approach has often been employed to represent structural relaxation in supercooled liquids approaching the liquid-glass transition. The single relaxation time form employed by Mountain (Eq. [1.15])can be easily generalized to a stretched exponential or other empirical relaxation function.

Four Lorentzians (Mountain Mode)

An approximation to Mountain's results, obtained by the method of residues as described in section 2-A, represents the spectrum as the sum of four Lorentzians. These are the Brillouin triplet described in section 2-A plus a fourth unshifted component (the Mountain Mode) which is due to structural relaxation. The fourth Lorentzian has half-width Γ_M and integrated intensity I_M. The light-scattering spectrum can be represented as

$$\begin{aligned} I(\omega) &= I_T \frac{\Gamma_T}{\Gamma_T^2+\omega^2} + I_M \frac{\Gamma_M}{\Gamma_M^2+\omega^2} \\ &+ I_B \left[\frac{\Gamma_B}{\Gamma_B^2+(\omega-\omega_B)^2} + \frac{\Gamma_B}{\Gamma_B^2+(\omega+\omega_B)^2} \right], \end{aligned} \qquad [2.14]$$

where ω_B is the shift of the Brillouin components; Γ_T, Γ_M , and Γ_B are the half-widths of the thermal diffusion mode, the Mountain mode, and the Brillouin modes, I_T, I_M, and I_B are the integrated intensities of the thermal diffusion mode, the Mountain mode, and the Brillouin modes, respectively.

A good fit result for the 240 K PC spectrum was obtained using this four-Lorentzian approximation, Eq.[2.14], as shown in Figure 2-5a. The fitting parameters are I_T, Γ_T, I_M, Γ_M, I_B, Γ_B, and ω_B. The residual fitting errors and the values of the fitting parameters are also shown in Fig.2-5a. From these fitting parameters, we have plotted the four Lorentzians separately (dashed lines) and their sum (solid line) in Figure 2-5b.

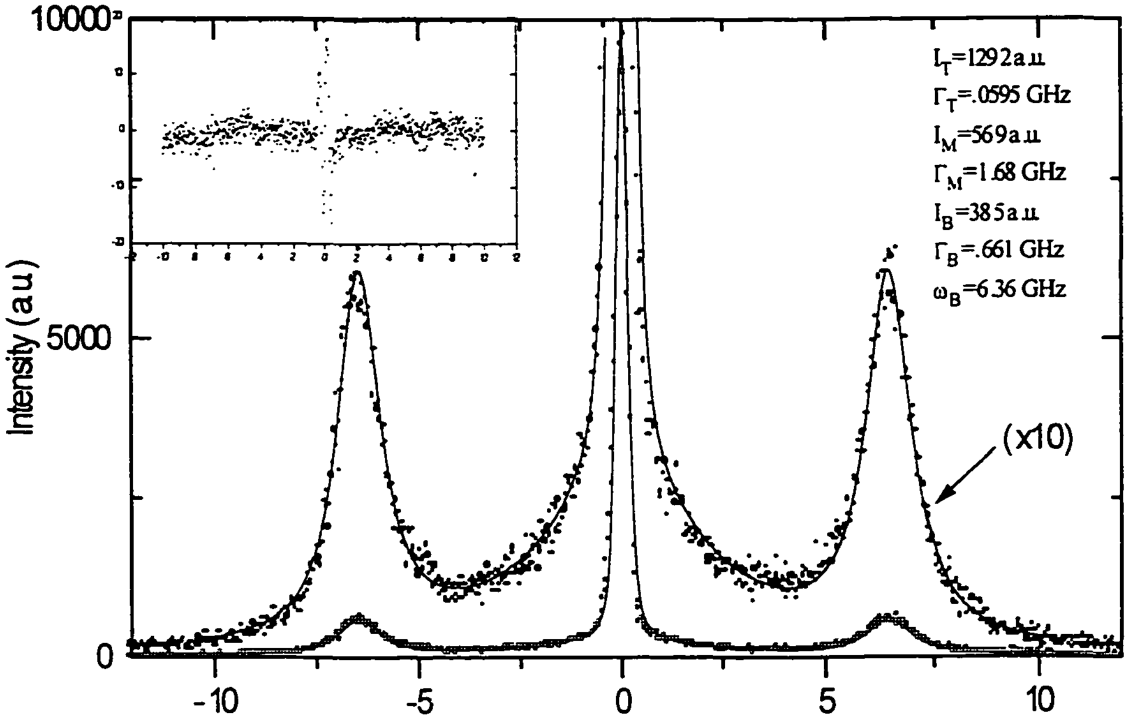

Figure 2-5a. PC 240 W with 4_Lorentzians Fit. Inset Residual fitting error

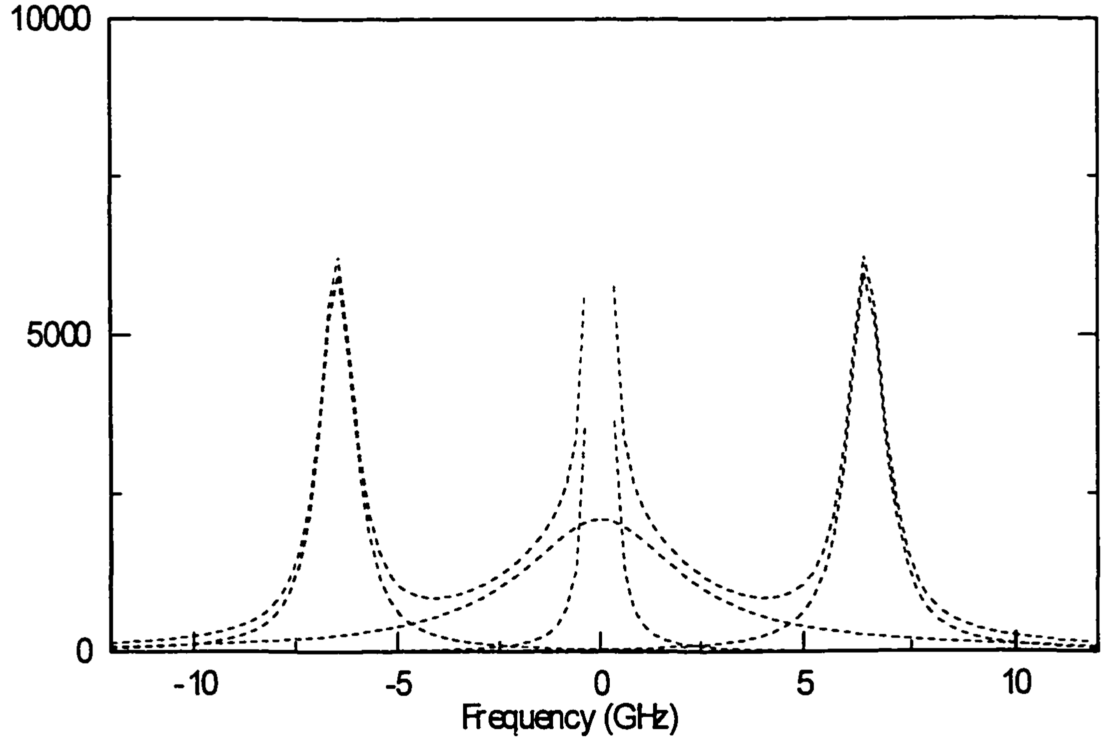

Figure 2-5b. 4 Lorentzians and Their Sum

Mountain theory

Mountain's generalization of conventional continuum Hydrodynamics added a single relaxation term b'(ω) to the regular longitudinal viscosity to represent the structural relaxation as described in section 1-D.

$$b(\omega) = b_0 + b'(\omega), \qquad [2.15]$$

with

$$b'(\omega)=b_1/(1+i\omega\tau), \qquad [2.16a]$$

$$b_0=(4/3\eta_S+\eta_B)/\rho_0 . \qquad [2.16b]$$

As discussed in chapter 1-D (Eq.[1.20]), the normalized spectral distribution function σ(k,ω) is given by [8]

$$\sigma(q,\omega) = 2\,\mathrm{Re}\left[\frac{s^2 + [(a+b_0)q^2 + b'(s)q^2]s + a(b_0 + b'(s))q^4 + C_0^2(1-1/\gamma)q^2}{s^3 + (a+b_0+b'(s))q^2s^2 + [C_0^2q^2 + a(b_0+b'(s))q^4]s + aC_0^2q^2/\gamma}\right]_{s=i\omega}$$

[2.17]

or, equivalently by

$$\sigma(k,\omega) = 2\frac{N_1D_1 + N_2D_2}{D_1^2 + D_2^2}, \qquad [2.18]$$

where

$$\begin{aligned}
N_1 &= -\omega^2 + ab_0q^4 + C_0^2q^2(1-1/\gamma) + (ab_1q^4 + b_1q^2\omega^2\tau)/(1+\omega^2\tau^2) \\
N_2 &= \omega[(a+b_0)q^2 + (b_1q^2 - ab_1q^4\tau)/(1+\omega^2\tau^2)] \\
D_1 &= -\omega^2(a+b_0)q^2 + C_0^2aq^4/\gamma + (ab_1q^4\omega^2\tau - \omega^2b_1q^2)/(1+\omega^2\tau^2)] \\
D_2 &= \omega[-\omega^2 + C_0^2q^2 + ab_0q^4 + (b_1q^2\omega^2\tau + ab_1q^4)/(1+\omega^2\tau^2)]
\end{aligned} \qquad [2.19]$$

Note that Eq.[2.17] reduces exactly to Eq.[2.2] if b_1=0 (without relaxation) and b_0=b.

Figure 2-6 shows the VV spectrum of PC at 240 K and the fitting curve (solid line) to Eq.[2.17] with the residual fitting errors and the values of the fitting parameters I_0, aq^2, b_0q^2, C_0q, b_1q^2, τ, and γ. We find that this fitting result is slightly better than the four-Lorentzian fit. Fits of the Mountain equation [2.17] to the VV spectra of PC at 5 different temperatures are shown in Fig.2-7. The linewidth of the Brillouin peaks reaches a maximum at about T = 240 K. At this temperature, the frequency shift of the Brillouin peaks satisfies $\omega_B\tau \approx 1$. By using the same method of residues described in section 2-A, the Mountain equation, Eq.[2.17], can be approximated by four Lorentzians [8],

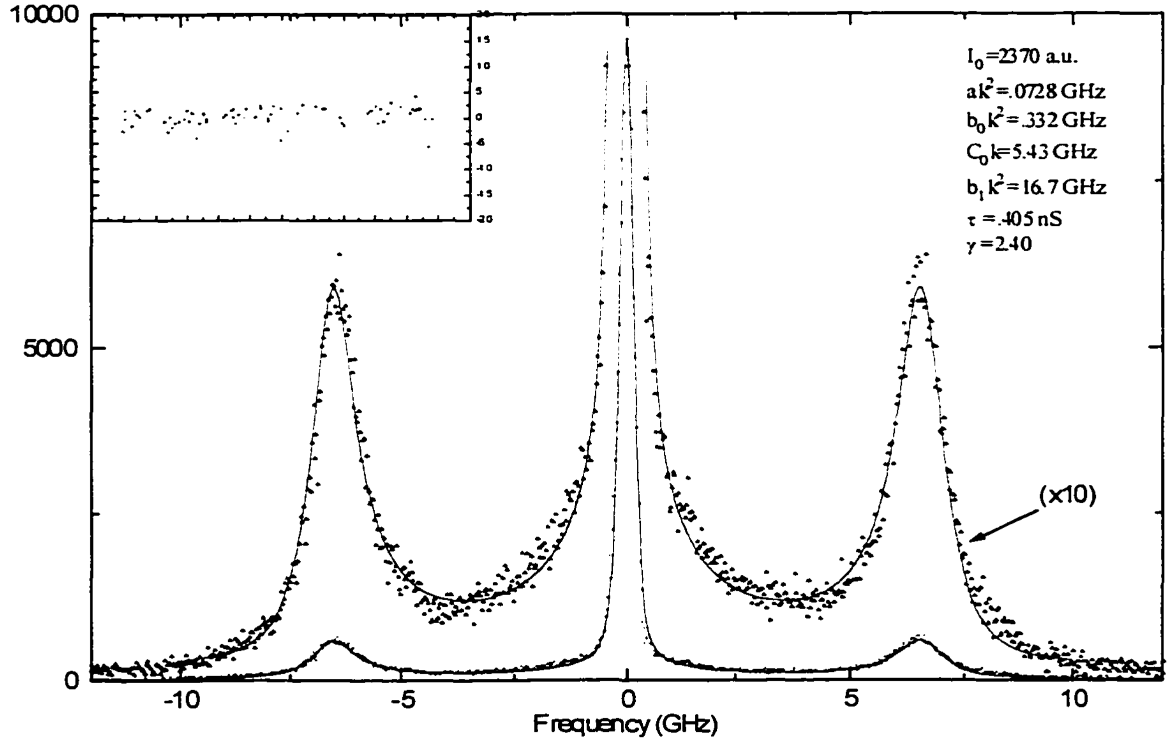

Figure 2-6 The VV spectrum of PC with full Mountain theory fit. The inset shows the residual fitting errors.

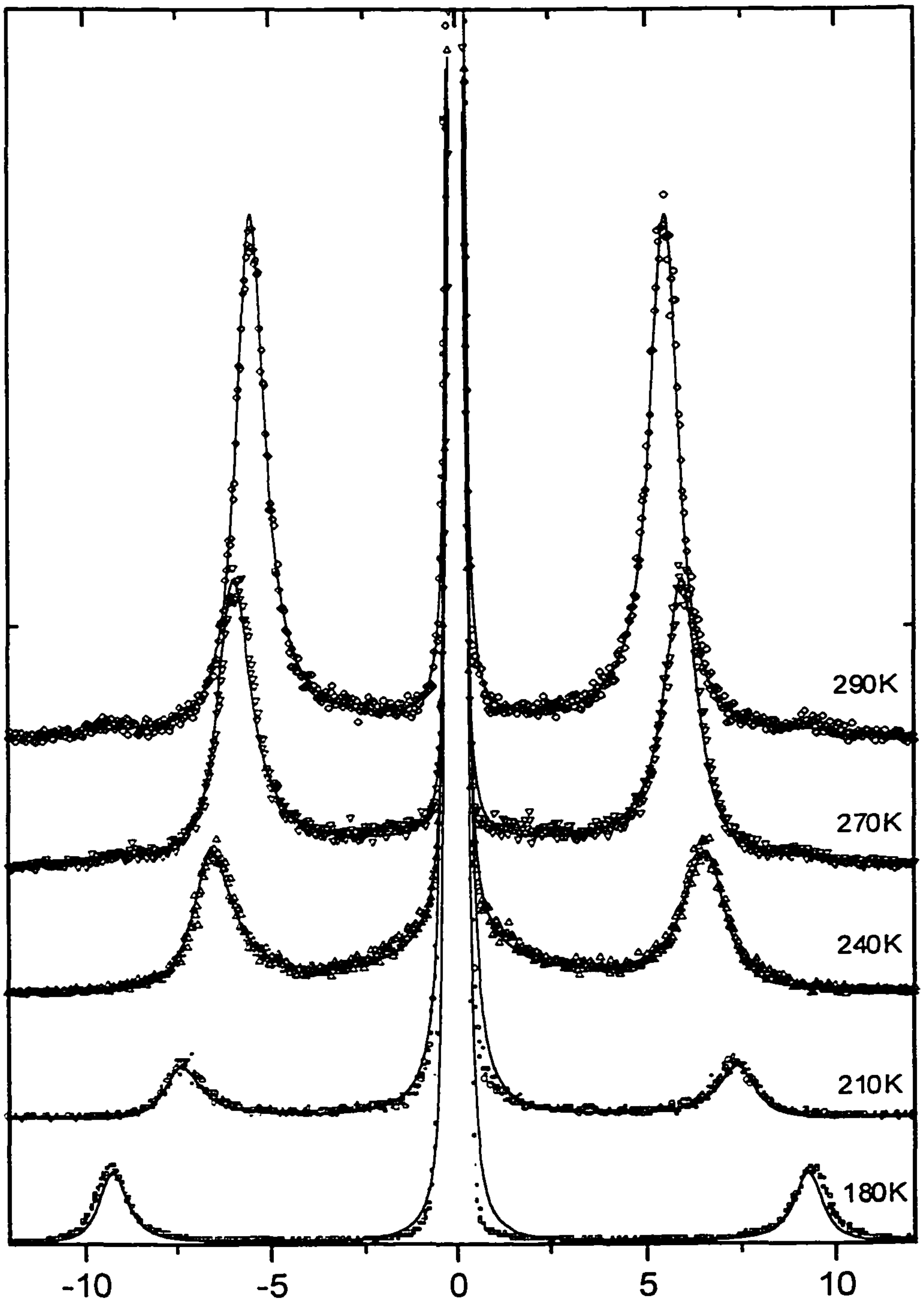

Figure 2-7 The VV spectra of PC at T = 290, 270, 240, 210, 180 (from top to bottom) with the Mountain equation fits (Eq. [2.17])

$$\sigma(k,\omega) = (1 - 1/\gamma)\frac{2\lambda q^2/\rho_0 c_p}{(\lambda q^2/\rho_0 c_p)^2 + \omega^2}$$
$$+\left[\frac{(C_\infty^2 - C_0^2)q^2 - (v^2/C_0^2 - 1)(C_0^4/v^4\tau^2 + C_0^2 q^2(1 - 1/\gamma)}{C_0^4/v^4\tau^2 + v^2 q^2}\right]\left[\frac{2C_0^2/v^2\tau}{C_0^4/v^4\tau^2 + \omega^2}\right] \qquad [2.20]$$
$$+\left[\frac{\left[1 - C_0^2/v^2(1 - 1/\gamma)\right]\left[v^2 q^2 + C_0^2/v^2\tau\right] - (C_\infty^2 - C_0^2)q^2}{C_0^4/v^4\tau^2 + v^2 q^2}\right]\left[\frac{\Gamma_B}{(\Gamma_B{}^2) + (\omega + vq)^2} + \frac{\Gamma_B}{(\Gamma_B{}^2) + (\omega - vq)^2}\right]$$

where the Brillouin shift is vq, with

$$(vq)^2 = \frac{1}{\tau^2}\{\frac{1}{2}[(C_\infty q\tau)^2 - 1] + \frac{1}{2}[(1 - C_\infty^2 q^2\tau^2)^2 + 4C_0^2 q^2\tau^2]^{1/2}\}, \qquad [2.21]$$

and the half-width of the Brillouin components is Γ_B, with

$$2\Gamma_B = aq^2 + b_0 q^2 - \left(\frac{C_0^2}{v^2}\right)\left(\frac{aq^2}{\gamma}\right) + \left[\frac{b_1 q^2}{1 + v^2 q^2\tau^2}\right](1 - aq^2\tau)\ . \qquad [2.22]$$

Relation between Mountain theory and 4 Lorentzians

Comparing Eqs.(2.20), (2.21), and (2.22) with Eq.(2.14), we find

$I_T = I_0(1 - 1/\gamma)$, [2.23]

$\Gamma_T = \lambda k^2/\rho_0 c_P$, [2.24]

$$I_M = I_0\left[\frac{(C_\infty^2 - C_0^2)q^2 - (v^2/C_0^2 - 1)[C_0^4/v^4\tau^2 + C_0^2 q^2(1 - 1/\gamma)]}{C_0^4/v^4\tau^2 + v^2 q^2}\right], \qquad [2.25]$$

$\Gamma_M = C_0^2/(v^2\tau)$, [2.26]

$$I_B = I_0\left[\frac{\left[1 - C_0^2/v^2(1 - 1/\gamma)\right]\left[v^2 q^2 + C_0^2/v^2\tau^2\right] - (C_\infty^2 - C_0^2)q^2}{C_0^4/v^4\tau^2 + v^2 q^2}\right], \qquad [2.27]$$

$$2\Gamma_B = aq^2 + b_0q^2 - \left(\frac{C_0^2}{v^2}\right)\left(\frac{aq^2}{\gamma}\right) + \left[\frac{b_1q^2}{1+v^2q^2\tau^2}\right](1-aq^2\tau), \qquad [2.28]$$

$$\omega_B{}^2 = (vq)^2 = \frac{1}{\tau^2}\{\frac{1}{2}[(C_\infty q\tau)^2 - 1] + \frac{1}{2}[(1-C_\infty^2q^2\tau^2)^2 + 4C_0^2q^2\tau^2]^{1/2}\}, \qquad [2.29]$$

where C_∞ is the high-frequency adiabatic sound velocity, with

$$C_\infty{}^2 = C_o{}^2 + (b_1q^2/\tau), \qquad [2.30]$$

$$C_0q \le \omega_B \le C_\infty q, \qquad [2.31]$$

The Landau-Placzek ratio

The ratio of the integrated intensity of the unshifted components to that of the Brillouin components is given by Eq.[2.23], [2.25], and [2.27]:

$$\frac{I_T + I_M}{2I_B} = \frac{(1-\frac{1}{\gamma}) + \frac{(C_\infty^2 - C_0^2)k^2 - (v^2/C_0^2 - 1)[(C_0^4/v^4\tau^2) + C_0^2k^2(1-1/\gamma)]}{C_0^4/v^4\tau^2 + v^2k^2}}{\frac{[1-C_0^2/v^2(1-1/\gamma)][C_0^2/v^2\tau^2 + v^2k^2] - (C_\infty^2 - C_0^2)k^2}{C_0^4/v^4\tau^2 + v^2k^2}} \qquad [2.32]$$

At low temperature, this ratio reduces to the conventional Landau-Pleczek ratio for simple liquids:

$$(I_T+I_M)/2I_B = I_C/2I_B = \gamma - 1 \ . \qquad [2.33]$$

At high temperature, a more involved expression is obtained:

$$\frac{I_T + I_M}{2I_B} = (\gamma - 1)\left[1 + \left(\frac{\gamma}{\gamma-1}\right)\left(\frac{C_\infty^2 - C_0^2}{C_0^2}\right)\right]. \qquad [2.34]$$

The ratio of the specific heats γ calculated from Eq.[2.33] or [2.34] is much larger than expected in the low temperature region.

Differences between the Mountain theory and 4 Lorentzians

Figure 2-8 shows the 4 Lorentzians (short dashed lines) calculated with Eq.[2.14] using the values of the fitting parameters obtained from the Mountain Equation in Eqs.[2.23] to [2.29], the sum of these 4 Lorentzians (long dashed line), and the Mountain equation fitting curve (solid line). The differences are significant, showing that the optimum 4-Lorentzian fit is not identical to the 4-Lorentzian approximation to the Mountain equation.

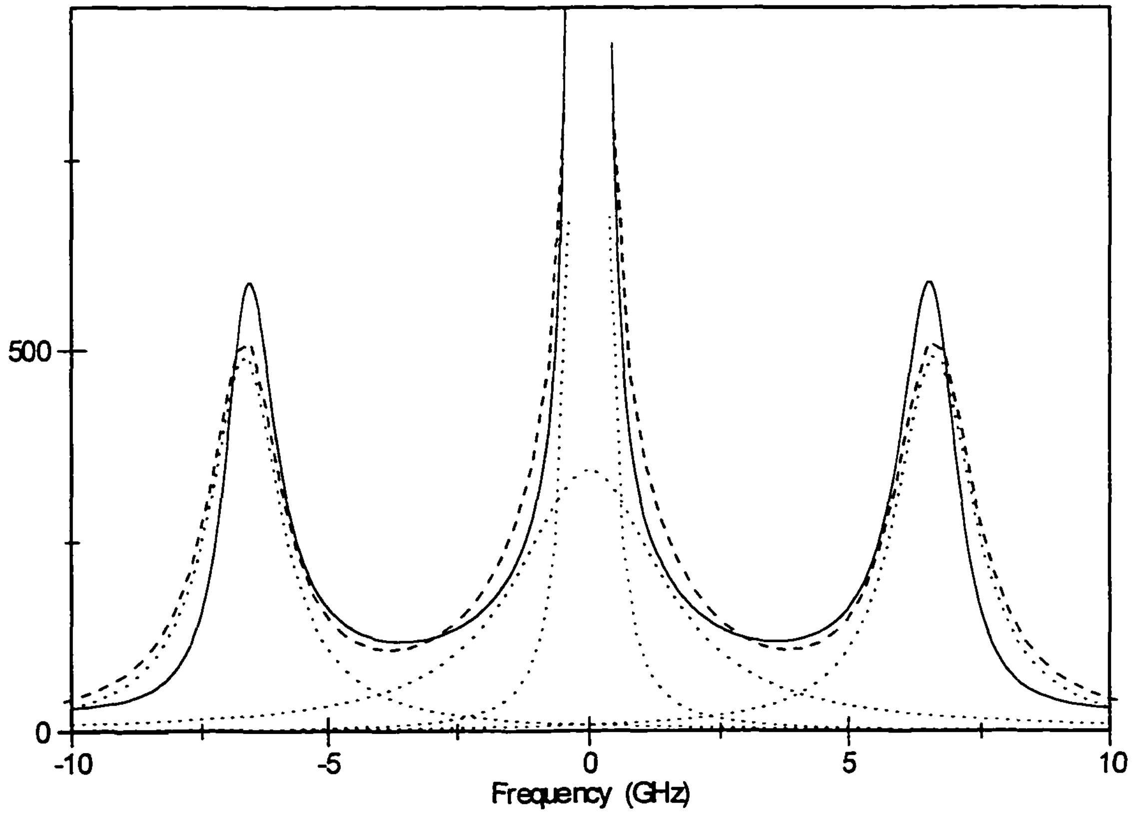

Figure 2-8 4 Lorentzians (Calculated From Eq.2.23-2.29) and their sum with full Mountain fit

Generalized hydrodynamic equation

Boon and Yip [33] noted that the dynamic structure factor $S(q,\omega)$ can be represented by

$$S(q,\omega) = \mathrm{Im}\,[\,\omega - \omega_0 - i\omega q\, D(q, i\omega)]$$

in which $D(q, i\omega)$ is a generalized damping function. $D(q, i\omega)$ can include thermal diffusion, structural relaxation, and even orientational motion. If we ignore thermal effects completely including thermal diffusion ($a = \lambda/\rho_0 c_P \approx 0$), the general result of the Mountain theory, Eq.[2.17] can be simplified considerably [65-66]. The normalized spectral distribution function (Eq.[2.17]) is then given by

$$\sigma(q,\omega) = \frac{(C_0^2 q^2/\gamma)[b_0 q^2 + b_1 q^2/(1+\omega^2\tau^2)]}{[\omega^2 - C_0^2 q^2 - b_1 q^2 \omega^2 \tau/(1+\omega^2\tau^2)]^2 + \omega^2[b_0 q^2 + b_1 q^2/(1+\omega^2\tau^2)]^2}\ . \qquad [2.35]$$

This result can be represented by

$$\begin{aligned} I(\omega) &= \frac{I_0}{\omega}\mathrm{Im}[\omega_0^2 - \omega^2 - i\omega b(\omega)]^{-1} \\ &= \frac{I_0}{\omega}\frac{\omega b'(\omega)}{[\omega^2 - \omega_0^2 - \omega b''(\omega)]^2 + [\omega b'(\omega)]^2}, \end{aligned} \qquad [2.36]$$

where $\omega_0 = C_0 q$, $b(\omega) = b_0\, q^2 + b_1\, q^2 / (1+i\omega\tau)$, and $b'(\omega)$ and $b''(\omega)$ are the real and imaginary parts of $b(\omega)$, respectively. Eq.[2.36] also can be rewritten as [65]

$$I(\omega) = \frac{I_0}{\omega}\mathrm{Im}\left[\omega_0^2 - \omega^2 - i\omega\Gamma(\omega)\right]^{-1} \qquad [2.37]$$

and

$$\Gamma(\omega) = \Gamma_0 + \Delta^2\left[\frac{1}{1 - i\omega\tau}\right] \qquad [2.38]$$

where $\Gamma(\omega)$ is a generalized damping function and Γ_0 is the damping constant. We will designate this approach, based on Eq.[2.37], as the generalized hydrodynamic formulation.

We used this generalized hydrodynamic equation, Eq.[2.37] and Eq.[2.38] with a thermal diffusion mode obtained from the 4-Lorentzian fit added to fit the VV spectrum of PC. The fitting parameters are I_0, b_1q^2, τ, C_0q, b_0q^2, and an additional fitting parameter *K* for adjusting the integrated intensity of the thermal diffusion mode I_T (I_T and Γ_T fixed). The fitting curve (solid line) and spectrum are shown with the fitting parameters and residual fitting errors in Figure 2-9.

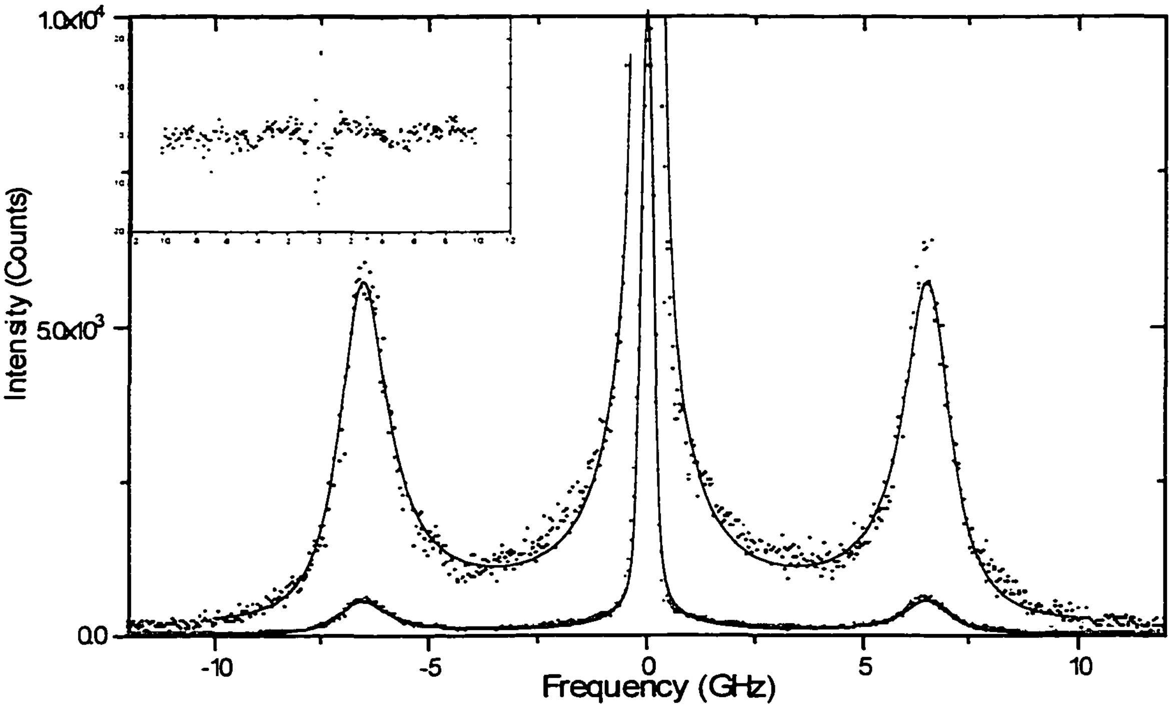

Figure 2-9 The VV spectrum of PC with Simplified Mountain Equation Fit

We plot the fitting curves of this generalized hydrodynamic equation (Eq.[2.37]) with the thermal diffusion mode added (right side, ○) and without the thermal diffusion mode (left side, □) with the fitting curve (solid line) of the Mountain Equation

(Eq.[2.17]) in Figure 2-10. We found that the fitting parameters of the generalized hydrodynamic equation without the thermal diffusion mode are very different than the two others.

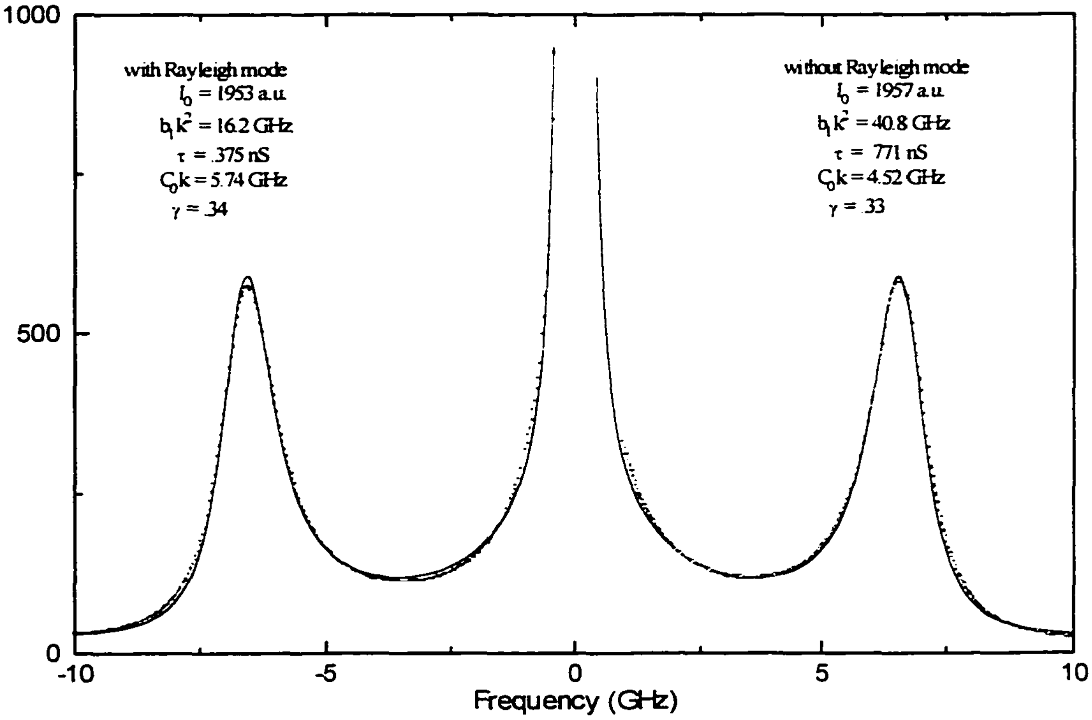

Figure 2-10 The fitting curves of generalized hydrodynamic equation with (left ☐) and without (right ○) thermal diffusion mode and the Mountain theory fitting curve (solid line)

Generalized hydrodynamic equation and the Mountain theory

The calculated curve of the generalized hydrodynamic equation was also obtained by substituting the values of the fitting parameters of the Mountain equation in Eq.[2.36] and plotted (dashed line) with the fitting curve of the Mountain equation (solid line) in Figure 2-11. The Brillouin modes of the calculated curve are shifted to higher frequency and the half-width of the Brillouin modes are too small. This is because the thermal diffusion mode contributes to the half-width and position of the Brillouin modes, Eq.[2.28] and Eq.[2.29]. If one wants to obtain an equivalent fitting curve to that of the Mountain equation, the fitting parameters must be adjusted. Specifically, by increasing $b_l k^2$ to increase the half-width and decrease the ω_B (or vk). When optimized, the fits obtained with those two approaches are nearly identical, as shown in Fig. 2-10.

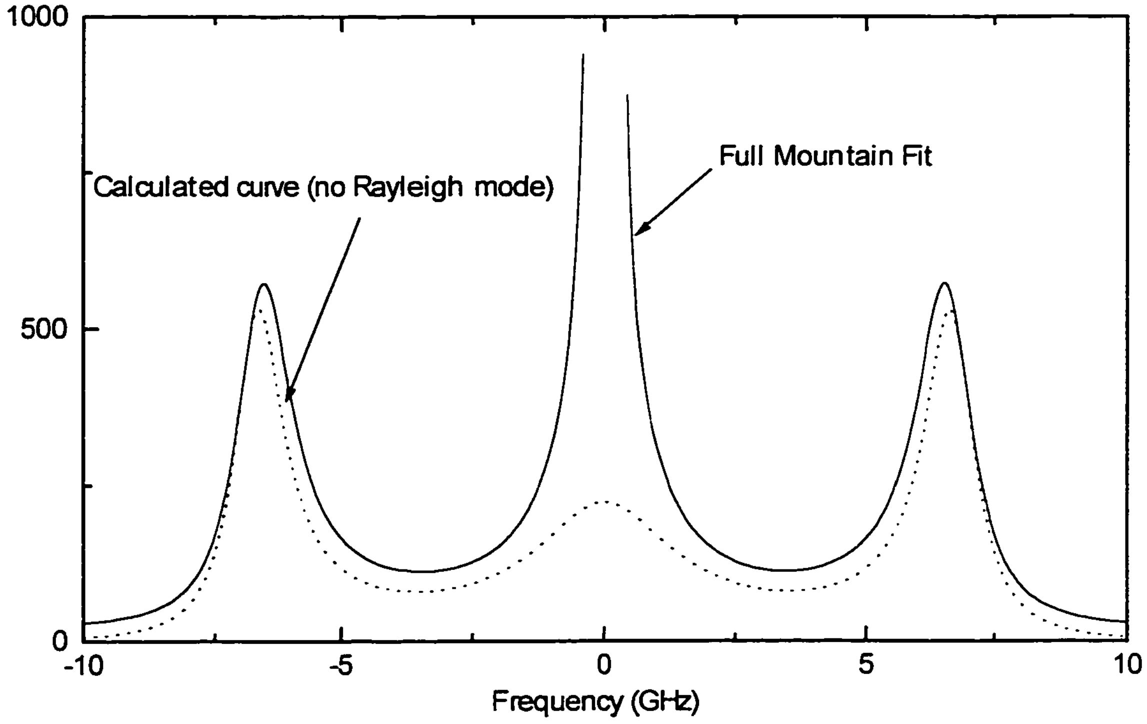

Figure 2-11 The curve calculated from Eq.2-32 with full Mountain fit

The Kohlrausch and Cole-Davidson functions

In analyzing Brillouin spectra, more complicated relaxation functions are often used instead of the single exponential function, such as the stretched exponential (Kohlrausch) function,

$$\Phi_K(t) = e^{-(t/\tau)^\beta}, \qquad (0<\beta<1) \qquad [2.39]$$

or the closely related Cole-Davidson function,

$$\Gamma(\omega) = \Gamma_0 + \Delta^2\left[1 - \frac{1}{(1 + i\omega\tau)^{\beta}}\right]. \quad (0<\beta<1) \qquad [2.40]$$

We have used Eq.[2.37], with the $\Gamma(\omega)$ of Eq.[2.40] to fit the VV spectrum of PC at 240K with fixed $\beta = 0.6$. The fitting curve (solid line) in Figure 2-12, and the spectrum are shown with fitting parameters. This fit is a little better than the fits described before.

All the fitting parameters obtained with the different fitting procedures discussed in this chapter are shown in Table 2-1.

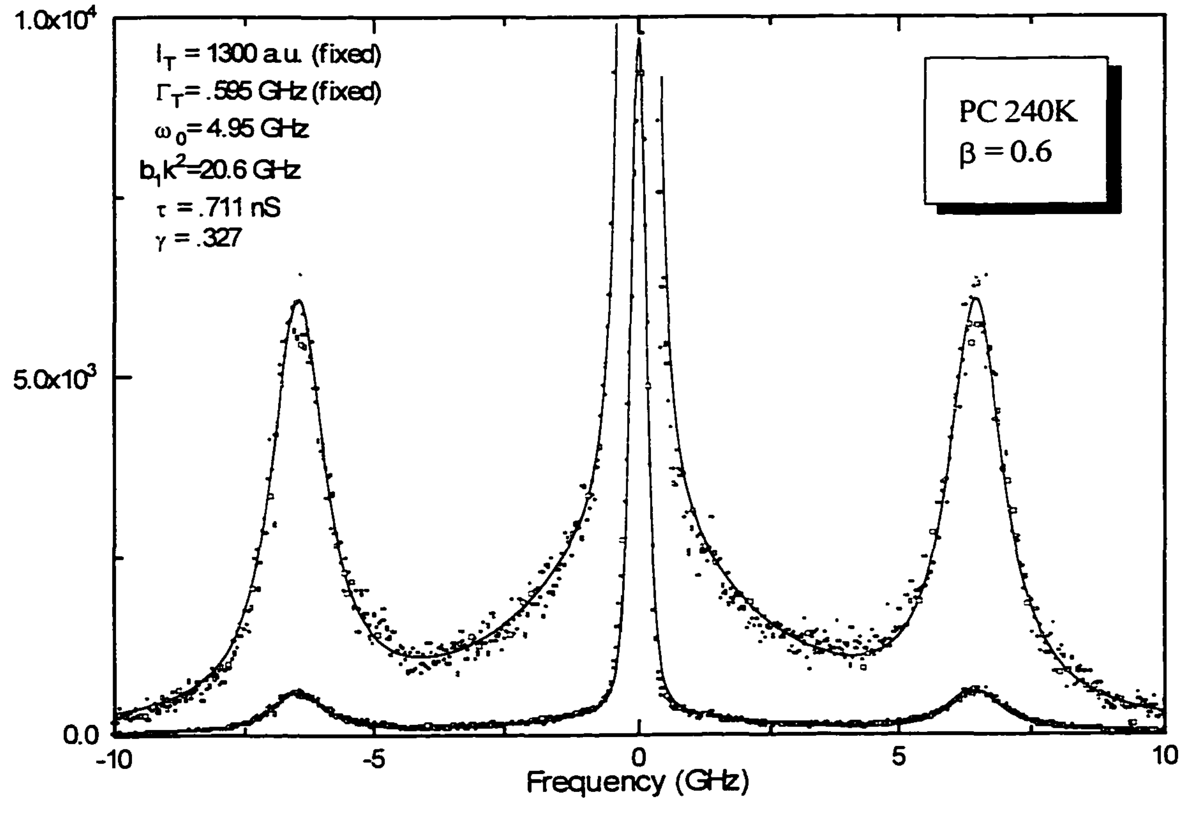

Figure 2-12 The generalized hydrodynamic equation with Cole-Davidson function fit (β fixed).

Table 2-1. Fitting Parameters

	I_T	Γ_T ($\Delta\omega_T$)	I_M	Γ_M ($\Delta\omega_M$)	I_B	Γ_B ($\Delta\omega_B$)	ω_B	I_0	(ak^2)	(b_0k^2)	(C_0k)	(b_1k^2)	τ	γ
3 Lorentzian	1536	.0144			419	.758	6.47							
Hydro. Equation								2430	.0161	1.42	6.37			2.64
4 Lorentzian	1292	.0595	569	1.68	385	.661	6.43							
4 Lorentzian (Calc)	1382	.0728	547	1.65	431	.870	6.64							
Mountain								2370	.0728	.332	5.43	16.7	.405	2.40
Γ(ω)+TD	1292	.0595						1953		.341	5.74	16.2	.375	
Γ(ω)+TD (Calc.)	1382	.0728						2370		.332	5.43	16.2	.405	
Γ(ω)								2934		.340	3.61	41.3	.764	
Γ(ω) (Calc.)								2370		.332	5.43	16.2	.405	
Γ(ω)+TD (β=.7)	1292	.0595						1916		.327	4.94	20.6	.711	

Table Caption

3-L	3 Lorentzians, Eq.[2.1]
Hydro:	Hydrodynamic Equation, Eqs.[2.3] - [2.5]
4-L	4 Lorentzians, Eq.[2.14]
Mountain:	Mountain theory, Eq.[2.18] - [2.19]
Γ(ω) + TD:	Generalized Hydrodynamic Equation with Thermal Diffusion Mode, Eqs.[2.37] – [2.38] and Eq.[2.14]
Γ(ω):	Generalized Hydrodynamic Equation without Thermal Diffusion Mode, Eqs.[2.37] – [2.38]
Γ(ω)+TD (β=.7)	Generalized Hydrodynamic Equation with Cole-Davidson function and Thermal Diffusion Mode Eqs.[2.37] – [2.40]
Calc:	The Values of Parameters are Calculated from parameters obtained from the Mountain theory fit

C. Complex Liquids of Anisotropic Molecules

In light scattering from molecular fluids, the incident light (polarized) impinges on the molecules and induces dipole moments. The magnitudes and directions of the induced dipole moments depend on the orientations of the molecules with respect to the electric field of the incident light. Because of continual reorientation of molecules, the magnitudes and directions of the induced-dipole moments fluctuate. This leads to fluctuations in the polarization and amplitude of the scattered light.

In general, the molecules of glass-forming liquids are optically anisotropic and the polarizability tensor has off-diagonal components. Then orientational fluctuations contribute to both the VV and VH spectra. The procedures discussed in sections 2-A and 2-B, representing density fluctuations alone, are only valid in liquids of isotropic molecules. The contributions of orientational fluctuations should be included in analyzing the VV spectrum of anisotropic molecules, as discussed in section 1-D.

Independent Density and Orientational Fluctuations

If the individual molecules are optically anisotropic but the velocity and orientational fluctuations are independent, the VV spectrum will contain independent uncorrelated contributions due to orientational and density fluctuations. (Additional contributions due to second-order collision-induced or DID scattering are also possible but will not be discussed here). The orientatonal scattering mechanism contributes to both the VV and VH spectra with intensity ratio 4:3 [34]. In principle, the spectrum due to density fluctuations alone, I_{ISO}, can be found from a simple subtraction:

$$I_{ISO} = I_{VV} - 4/3\ I_{VH} \qquad [2.41]$$

The procedures discussed in sections 2-A and 2-B can then be used to analyze the resulting I_{ISO} spectra, but usually one finds that there is at most only a very weak Mountain mode contribution remaining in the I_{ISO} spectra. This problem is illustrated in the I_{ISO} spectrum of PC at T = 240K shown in Fig. 2-13. Similar results were also found in salol [67] and OTP [68].

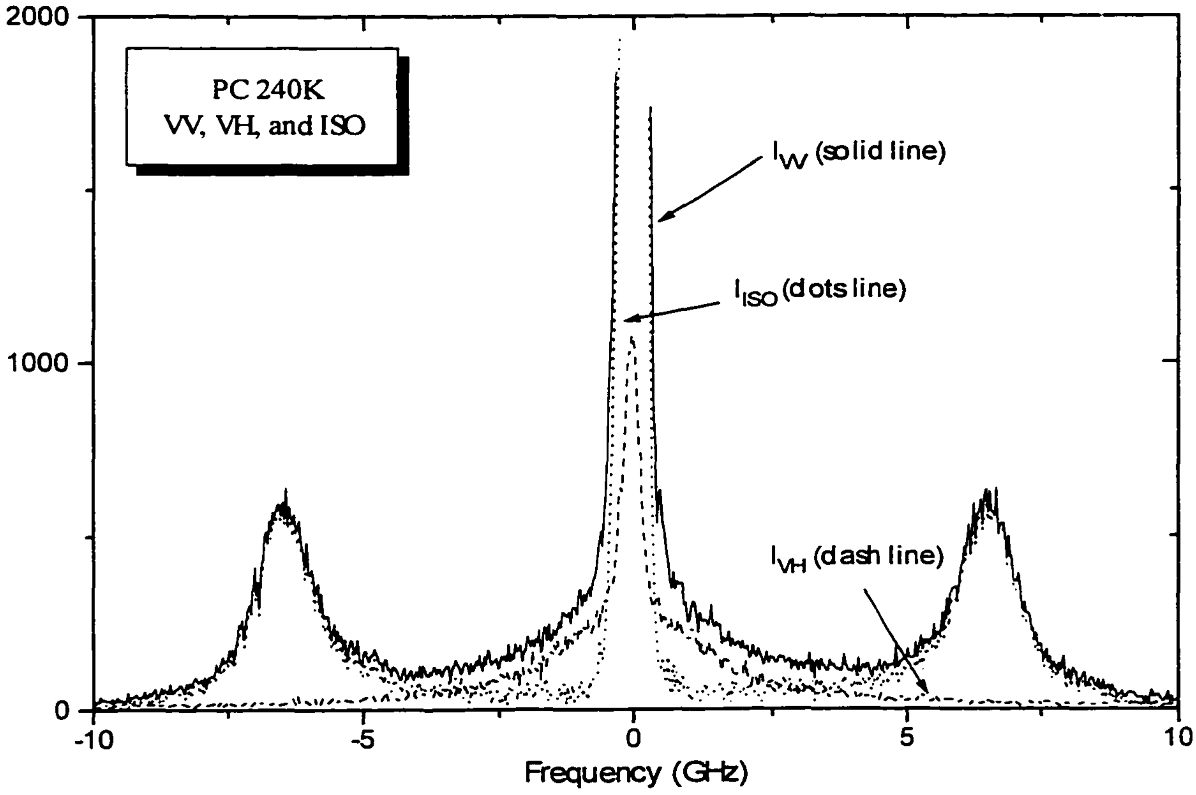

Figure 2-13 The 90^0 VV, VH, and ISO (from Eq.2.41) spectra of PC

Determining the constant k

In practice, the constant 4/3 has usually been arbitrarily replaced by an adjustable fitting parameter k which is somewhat smaller then 4/3, for example, k=1.24 for PC [22]. This k was determined by the ratio of I_{VV} and I_{VH} at high frequency (~100GHz) which is far above the Brillouin peak frequency (~10GHz). Since we do not know what is the exact value of k, we believe that there are only the orientational contributions of anisotropic molecules and DID contributions at high frequency.

If we assume that 4/3 is the correct value, we still need to make a correction because the transmission functions of the interferometer are different for VV and VH spectra. For our interferometer, the transmission function of the vertical polarization is 1.065 times that of the horizontal polarization. We obtained even weaker Mountain modes by this method. Therefore, to obtain an isotropic spectrum, the method of simply subtracting the whole depolarized spectrum from the polarized spectrum is not satisfactory.

Inclusion of the translation-rotation coupling

The simple subtraction method failed to calculate the isotropic spectrum of the liquids of anisotropic molecules since the interaction potential between any two molecules is not separable in the relative positions and orientations of these two molecules. Some new features appear in the depolarized spectra because of the translation-rotation coupling. People usually treat this problem by considering both the rotational and translational diffusion coefficients to be tensors [34]. In experiments, the problem becomes how to separate the orientational fluctuations from the density fluctuations to obtain a pure isotropic spectrum.

Clearly, the simple subtraction procedure of Eq.[2.41] fails at low temperatures where $I_{VH}(\omega)$ includes transverse Brillouin components [67]. The difficulty is that while $I_{VH}(\omega)$ includes effects due to transverse velocity-rotation coupling, such effects are essentially missing in $I_{VV}(\omega)$. Fig. 2-14 shows the VV (long dashed line), VH (short dashed line), and isotropic spectrum (solid line) of salol at T = 230K. This isotropic spectrum was obtained from Eq.[2.41] with k = 1.24. There are two holes caused by the transverse modes of the depolarized spectrum. As noted in section 1-E, this issue is still under study and will not be discussed further in this thesis.

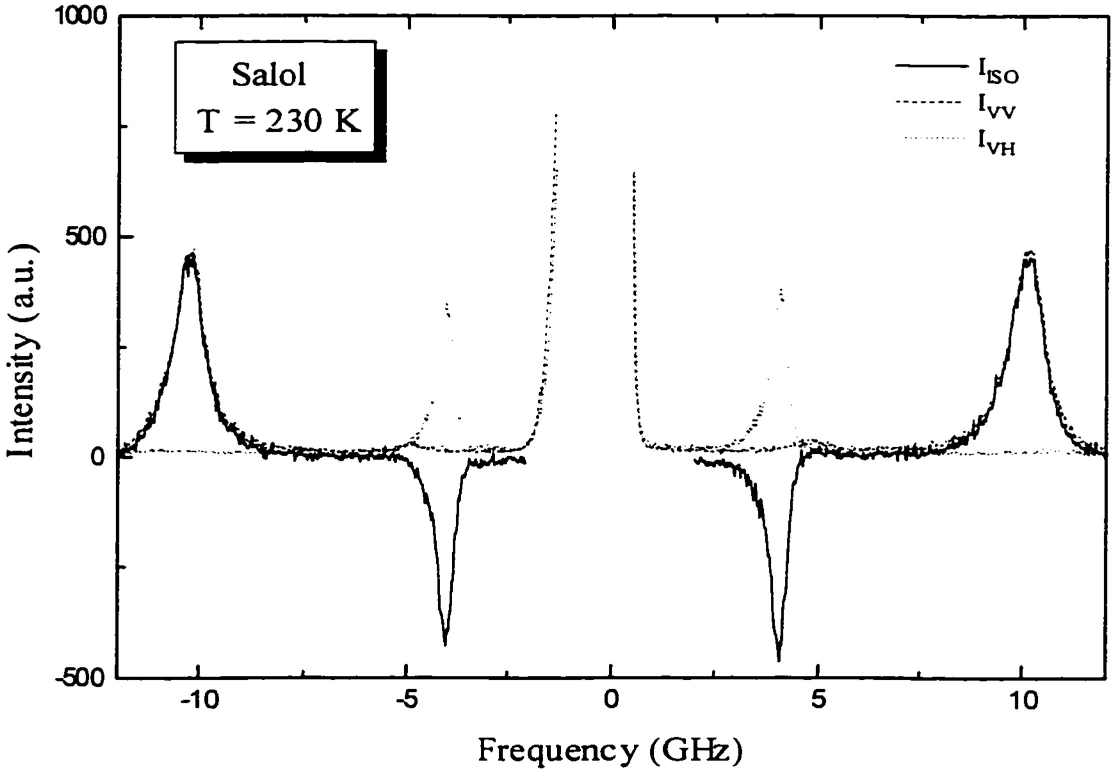

Fig. 2-14 The VV, VH, and ISO spectra of Salol at 230K

Chapter 3

Experimental Apparatus and Data Processing

A. Principle of the Fabry-Perot interferometer

Fabry-Perot interferometer

Brillouin scattering spectroscopy using the Fabry-Perot interferometer is a well-established method for investigating thermal sound waves in supercooled liquids. We give a brief summary here. For more details, consult reference [69].

A Fabry-Perot interferometer, Fig.3-1, consists of two high quality plain mirrors mounted accurately parallel to each other, and separated by an optical spacing L. The transmission function for normal incidence is given by

$$T = \frac{T_0}{1 + \frac{4F^2}{\pi^2}\sin^2\left(\frac{2\pi L}{\lambda}\right)}, \qquad [3.1]$$

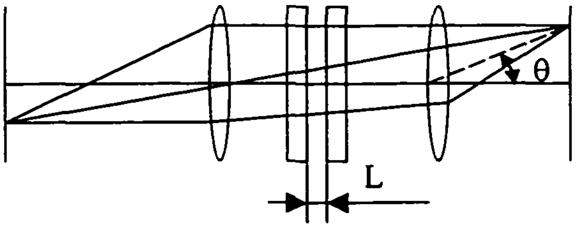

Fig. 3-1 Diagram of the Fabry-Perot interferometer

where T_0 (≤ 1) is the maximum possible transmission determined by the mirror reflectivity R and by losses in the system, F is the finesse which is defined as the ratio of the free spectral range (FSR), ν, to the full width at half maximum (FWHM), $\Delta\nu$ of the instrument response, and λ is the wavelength of the transmitted light.

Equation [3.1] shows that only those wavelengths satisfying

$$L = m\frac{\lambda}{2}, \qquad [3.2]$$

for integral values of m, will be transmitted. This is illustrated in Fig.3-2.

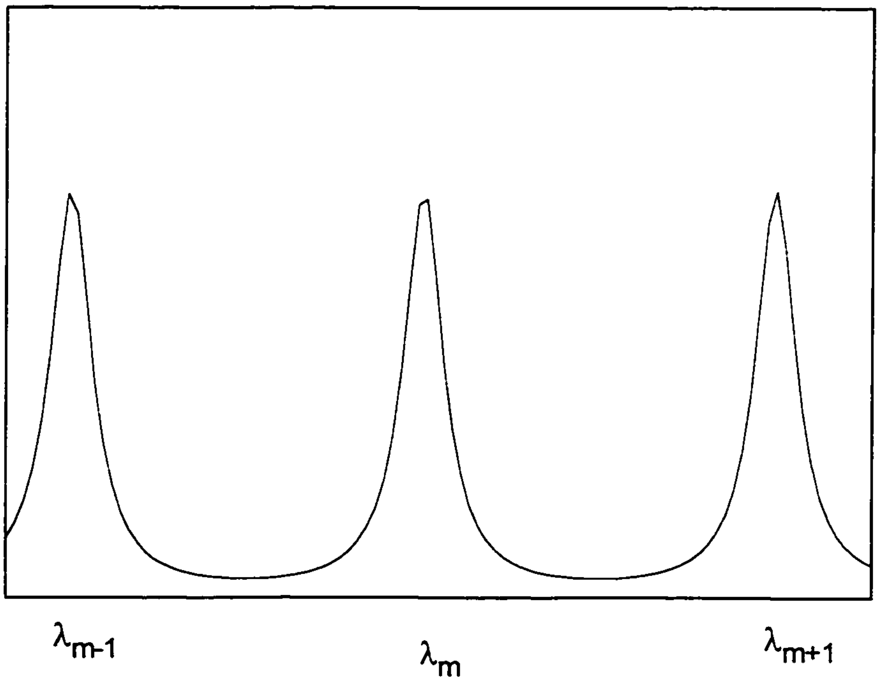

Fig. 3-2 Schematic transmission function

Free spectral range (FSR)

Form Eqs. [3.1] and [3.2], if a single wavelength λ is present, maxima will appear each time L increases by $\lambda/2$. If a range of wavelengths is present, for fixed m the resonant λ will change with L as $\Delta\lambda = 2\Delta L/m$. The change $\Delta\lambda$ corresponding to increasing L by one order is therefore $\Delta\lambda = \lambda^2/2L$ or

$$\nu = c/2L\,. \qquad [3.3]$$

where c is the speed of light in air. This ν is called the free spectral range (FSR). According to Eq. [3.3], the FSR only depends on the separation of two mirrors. Then, we can change the separation to obtain different FSRs. We also can convert the Brillouin spectrum from channel number to frequency using Eq.[3.3].

The finesse of a Fabry-Perot interferometer

The finesse ($F = \nu$ (FSR)/$\Delta\nu$) of a Fabry-Perot (FP), where $\Delta\nu$ is the observed width of a monochromatic spectral line due to the FP, depends primarily on the mirror reflectivity and the departure of the mirror surfaces from ideal planes. With the consideration of these two effects, we have a reflectivity finesse, F_r, and a surface finesse, F_s:

$$F_r = \frac{\pi\sqrt{R}}{1-R}\,, \qquad [3.4a]$$

$$F_s = \frac{M}{2}\,, \qquad [3.4b]$$

where R is the reflectivity of the mirror and M/2 is the r.m.s. variation of the mirror surface flatness.

In a real system, light is collected from a finite size source and over a finite solid angle so that the collimated light is not perfectly parallel light. This effect will cause an additional broadening of the transmission peak. For a pinhole with diameter d at the focus of a collimating lens of focal length f, the pinhole finesse is given by

$$F_p = \frac{4\lambda f^2}{d^2 L}\,. \qquad [3.5]$$

Then, the combined finesse F is given as

$$\frac{1}{F^2} = \frac{1}{F_r^2} + \frac{1}{F_s^2} + \frac{1}{F_p^2} \; . \qquad [3.6]$$

The contrast factor of a FPI

Another important characteristic of a FP interferometer is the contrast factor which is defined as the ratio of maximum transmission to the minimum transmission and is related to the finesse of the system by

$$C = \frac{T_{max}}{T_{min}} = 1 + \frac{4F^2}{\pi^2} \qquad [3.7]$$

The n-pass FPI

Although the finesse of a single-pass FP interferometer can be increased to ~ 80, the low contrast limits its application in observing a Brillouin spectrum in which there is an extremely strong elastic part. This problem can be solved by using a multi-pass FP interferometer [69-70]. For an n-pass FP interferometer, the transmission function is the nth power of the single FP interferometer's:

$$T_n = (T)^n . \qquad [3.8]$$

The finesse and the contrast factor of the system are

$$F_n = \frac{F}{(2^{1/n} - 1)^{1/2}} \; , \qquad [3.9]$$

$$C_n = (C)^n . \qquad [3.10]$$

For a 5-pass FP interferometer with R = 95%, finesse $F_5 \geq 80$ and contrast factor $C_5 \geq 10^{10}$ can easily be achieved. Higher reflectivity only lowers the transmission without appreciably increasing the finesse because other factors become dominant. A multi-pass FP interferometer provides a high finesse and contrast factor, but it can not eliminate the overlapping of neighboring interference orders. This problem makes analysis of the spectrum more difficult, sometimes even impossible [71].

The tandem Fabry-Perot interferometer

The tandem Fabry-Perot interferometer (TFPI), introduced by Sandercock in 1978 [71], provides a practicable solution to this problem. A Sandercock TFPI consists of two FP etalons in which the scanning mirrors of both interferometers are mounted on a common translation stage. The axis of the first FP is along the scan axis while the second one is rotated, as shown in Fig.3-3, by a fixed angle θ. Assuming that L_1 and L_2 would both be zero at the same position of the stage, the spacing of these two FPs is related by

$$L_2 = L_1\cos\theta . \qquad [3.11]$$

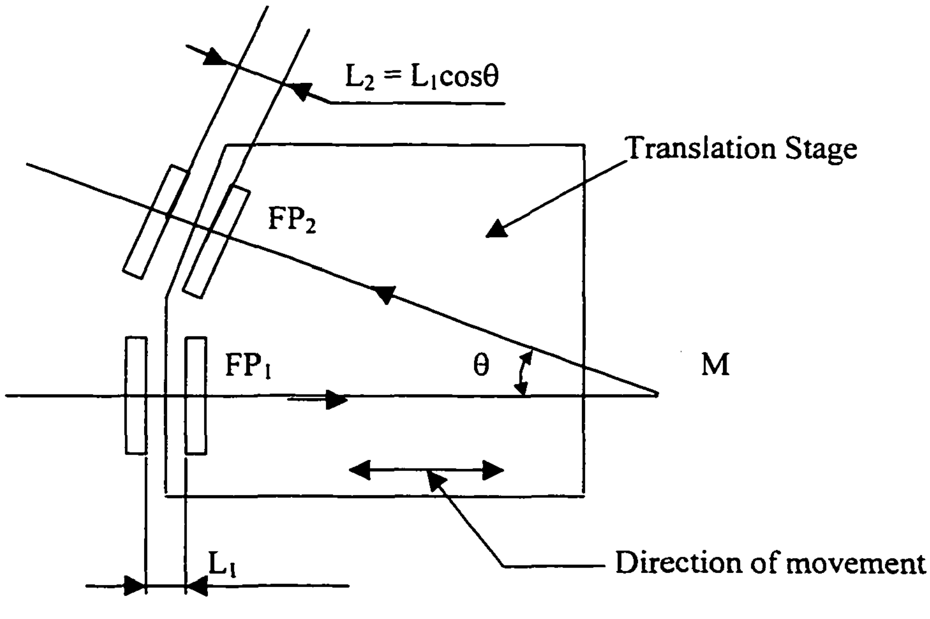

Fig.3-3 schematic diagram of TFPI

The light will be transmitted through this system only when both FPs satisfy the resonance condition:

$$n_1\lambda/2 = L_1, \qquad n_2\lambda/2 = L_2, \tag{3.12}$$

where n_1 and n_2 are integers, L_1 and L_2 are the mirror separations of the first and second FP. The Sandercock TFPI automatically satisfies the synchronization condition:

$$\frac{\Delta L_2}{\Delta L_1} = \frac{L_2}{L_1} = \cos\theta, \tag{3.13}$$

where ΔL_1 and ΔL_2 are the variations of L_1 and L_2 during the scan, respectively, assuming that the zero points of L_1 and L_2 coincide.

The transmission functions of each FP interferometer are

$$T_{FP1} = \frac{T_0}{1 + \frac{4F^2}{\pi^2}\sin^2(\frac{2\pi L_1}{\lambda})}, \tag{3.14a}$$

$$T_{FP2} = \frac{T_0}{1 + \frac{4F^2}{\pi^2}\sin^2(\frac{2\pi L_1 \cos\theta}{\lambda})}, \tag{3.14b}$$

and the total transmission function for light passing these two FPs in tandem is

$$T_{tot} = T_{FP1} * T_{FP2} \tag{3.14c}$$

Schematic plots of equations [3.14] are shown in Figure 3-4. It is clear that the neighboring interference orders are suppressed because of equation [3.13]. using a multi-pass Sandercock TFPI, we can obtain a high suppression of the interference orders, high resolution, and a high contrast system for Brillouin scattering.

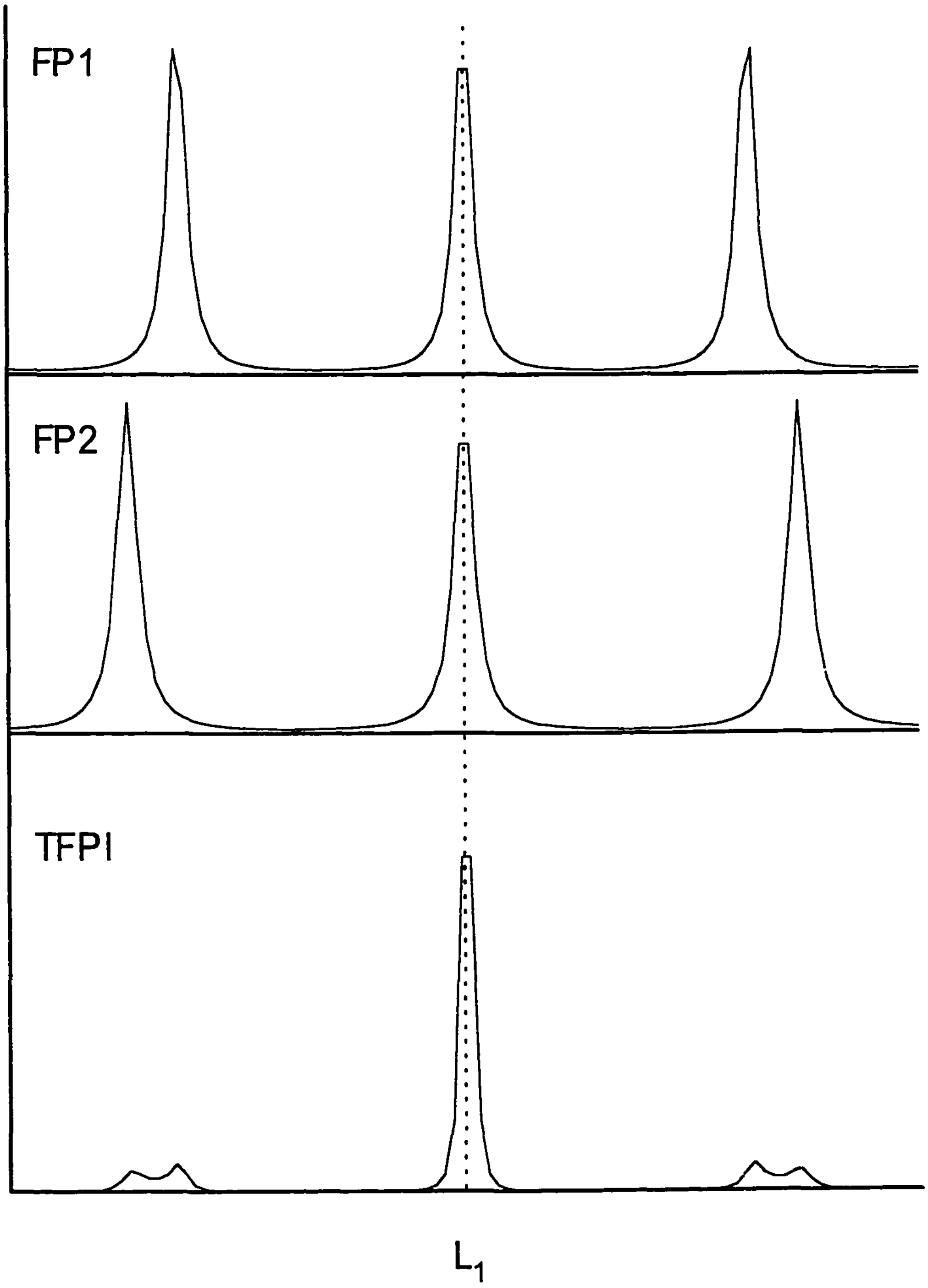

Figure 3-4. Transmission function of the TFPI

B. Brillouin scattering apparatus

A schematic diagram of the experimental apparatus

The interferometer used in our Brillouin scattering spectrometer is a Sandercock TFPI with 6-pass (3x2) operation. The interferometer mirrors are 60mm diameter fused silica flats with a reflectivity of R = 92% at λ = 488nm and a finesse of ~60 over the central 46mm region. The back surfaces of the mirrors are antireflection coated to minimize transmission losses and unwanted reflection. The angle between the first FP axis (scan axis) and the second FP axis is $\theta = 18^{\circ}$ ($\cos\theta = 0.95$) and the mirror separation range is from 0 to 27mm. The mirror used for coupling the first and second FP has reflectivity R = 99 % and a flatness of $\lambda/40$.

A Spectra-Physics 165 Argon ion laser with a built-in air spaced etalon is used as a light source which can be operated in a single mode at λ = 488nm or λ = 515nm.

A schematic diagram of the 90° Brillouin scattering apparatus is shown in figure 3.5. The incident light is polarized perpendicular to the scattering plane and the polarization of the scattered light can be selected by placing a polarizer in the path of the collected light. To protect the photomultiplier tube (PMT) from overload, a computer controlled fast shutter is placed before the focusing lens L_1. The shutter is closed by computer control when the TFPI scans over the strong elastic scattering frequency range of the central order and neighboring orders.

Optical setting

An intense reference beam at the laser frequency is required for automatic stabilization when the shutter is in operation. This is obtained with the beam splitter S1

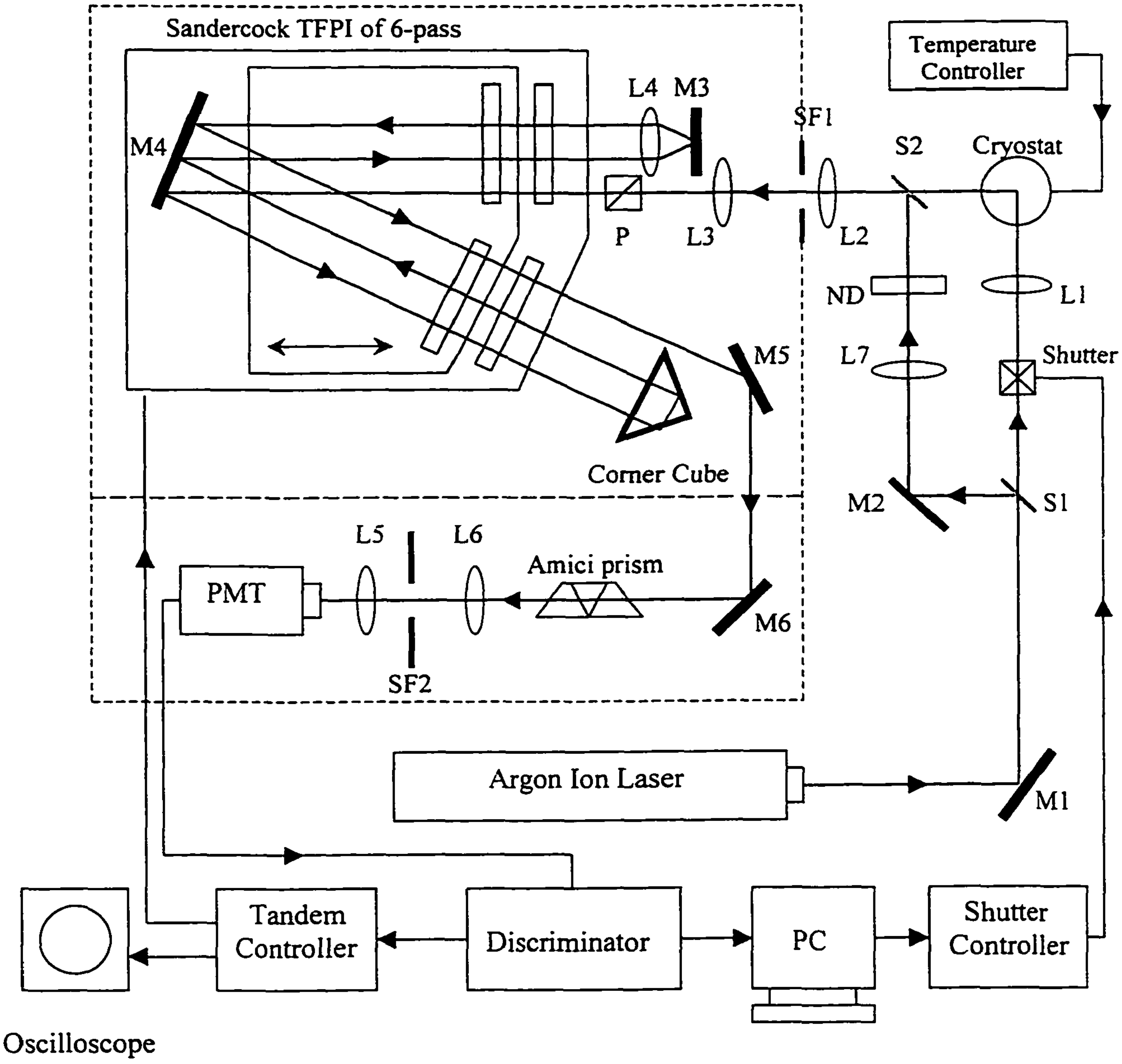

L: Lens
M: Mirror
ND: Neutral Density Filter
P: Polarizer
S: Beam Splitter
SF: Spatial Filter

Figure 3-5 Schematic apparatus of the Brillouin scattering and a continuously adjustable neutral density filter. The second beam splitter S2 is both for sending the reference beam into the system and for acting as a high quality transmitting mirror for the scattered light.

The scattered light (and reference light) is collected and passed through the first spatial filter SF1 which serves to define the scattering volume. The pinhole must be small enough to maintain a high finesse but also should be as large as the scattering volume. The size of the pinhole (0.1-0.5mm depends on the separation) in the spatial filter is chosen according to Eq. [3.5] such that $F_P \sim 150$. The combination of the coupling mirror M4, corner-cube, and cat's-eye element (L4 and M3) reflects the beams and adjusts the beam position to complete the 6 (3x2)-pass through the TFPI.

Band-pass filter and photo-multiplier

Because the frequency response of the PMT is much wider than the effective free spectral range (FSR) of the TFPI, significant background noise would be caused by the light outside the FSR such as Raman scattering and fluorescence from the sample and optics, ambient room light, etc. In order to eliminate this background noise, we use an Amici dispersing prism and spatial filter as a final band-pass filter SF2. Comparison with the regular 1nm filter (30% transmission function), our setup has higher transmission function (~85%) but larger band-width (10nm) at $\lambda = 488$nm.

A Hamamatsu model R464 PMT that has a spectral response range of 300-700nm collects the scattered light. At room temperature, the dark count is about 3.5 count/second (a little high in some depolarized scattering experiments with weak scattering intensity). By using a discriminator and a pre-amplifier, the output of the PMT is converted into a

TTL signal, which is recorded by an EG&G multi-scaler data acquisition system during the scan.

Decoupling vibrations

To decouple the vibrations from the surrounding environment, the whole Brillouin scattering apparatus is mounted on a compressed air floating optical table (Modern Physics). The decoupling of vibration arising from the equipment is accomplished by supporting the laser and the TFPI unit with anti-vibration rubber pads. The other optics are supported solidly by metal holders and guiding rails. To minimize the influence of the air motion inside the FP interferometer and obtain better thermal uniformity, a plexiglass box is used to enclose the entire interferometer.

For maintaining the high contrast of the multi-pass FP interferometer, black cardboard masks are placed at the front and rear of the Fabry-Perots, the front of the coupling mirror and corner cube, and in some additional places.

With these precautions, we obtain a Brillouin scattering spectrum with mirror separation of 10mm with a finesse $F \geq 60$, a contrast $C \sim 10^{10}$, and a suppression ~ 200 of the neighboring interference orders.

C. Data Processing

Data collection

The signal from the PMT also serves as a reference signal for stabilizing the TFPI; it is fed to the EG&G multi-channel scalar (MCS) data acquisition adapter card in a Force 3570 personal computer (Packard Bell). The scan length can be from $2^2(4)$ to

2^{12}(4096) channels. In our Brillouin scattering experiments, a total of 2^{10}(1024) channels is generally used with a collection time of 0.5ms/channel•scan which matches the time scale of the TFPI controller. Sequential scans are accumulated to build up the Brillouin spectrum until a satisfactory Brillouin spectrum is obtained. The accumulation time (depending on the scattering intensity of materials) can be several minutes to more than 10 hours. The result is displayed in real-time on the computer screen and can be saved on the hard (or floppy) disk for further data analyses.

Figure 3-6a shows a typical $\theta = 90^\circ$ polarized (VV) Brillouin scattering spectrum of Acetone at room temperature (294K) with mirror separation of 8mm and Laser wavelength of 488nm. The central peak is the Rayleigh component. The two small peaks (G_L and G_R) near the edges of the spectrum are the suppressed neighboring interference orders (ghosts) of the central component. Between the Rayleigh line and the two ghosts, there are two Brillouin components of the longitudinal acoustic modes. The Stokes component (LA_S) is at the right side and the anti-Stokes component (LA_A) is at the left side.

Data conversion

To convert the x-axis of this spectrum from channel number to frequency (or wave-number), we first locate the position of the central peak by fitting it with a Lorentzian function and this peak position is used as the zero frequency shift point; Second, we determine the frequency scale of the spectrum using the two ghosts (G_L and G_R) whose positions define by the FSR which corresponds to the separation of the FP by

$$\mathrm{FSR} = \frac{1}{2L_1}\ (\mathrm{cm}^{-1})\,. \qquad [3.15]$$

Figure 3-6b shows the converted spectrum obtained from Eq.[3.15] for L = 8mm.

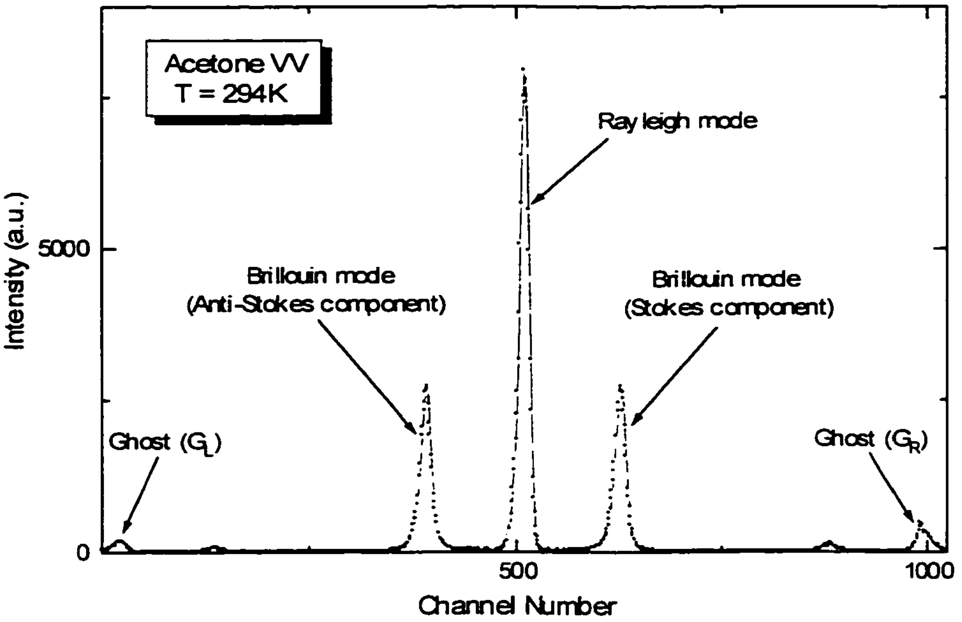

Fig. 3-6a The 90^0 VV spectrum of Acetone at T=294K in channel number

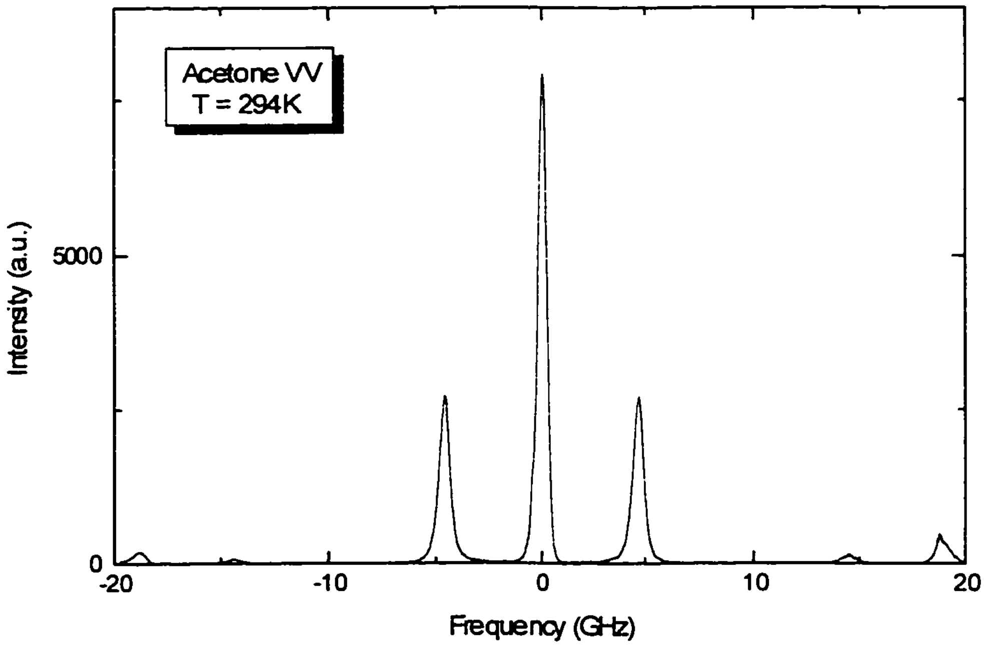

Fig. 3-6b The 90^0 VV spectrum of Acetone at T=294K in frequency

The instrumental response function

Because of the instrumental response function $\bar{I}(\omega)$, the experimentally observed Brillouin spectrum, I(ω), is given by

$$I(\omega) = \int \bar{I}(\omega - \omega')S(\omega')d\omega', \tag{3.16}$$

where S(ω) is the real spectrum before passing through the TFPI. So, before fitting this Brillouin spectrum, I(ω), with a theoretical function, we should convolute the theoretical function with the instrumental response function. In the actual fitting process, the integral is replaced by a summation so that we can directly use the stored digital values of the Rayleigh component obtained with the reference beam as the instrumental response function $\bar{I}(\omega)$.

The non-linear least squares method

The non-linear least squares method is used in our fitting programs. It seeks a set of fitting parameters that, minimize the residual error function

$$\Delta(x)=\sum (y_i - f_i)^2, \tag{3.17}$$

where y_i is the nth experimental data value and f_i is the corresponding theoretical value. Our programs are based on the Fortran program "nllsq.f" from the Bell Laboratories port library. The reduced χ^2 is defined as

$$\chi^2 = \sum_i \frac{(y_i - f_i)^2}{y_i(n - n_p)} \tag{3.18}$$

where n is the total number of data points and n_p is the number of parameters. The χ^2 calculation provides a criterion for testing if the theoretical function agrees with the experimental data. Usually, fluctuations of the signal obey Poisson statistics. Then, χ^2 is approximately equal to 1 if the theoretical function accurately describes the experimental data and is larger than 1 if it does not.

Chapter 4

Brillouin Scattering Measurements

A. Materials

Propylene Carbonate (PC)

Propylene Carbonate (4-methyl-1, 3-diadem-2-one, $C_4H_6O_3$) is a fragile (m = 104) glass-forming material and a polar cyclic carbonate [3, 72]. Fig. 4-1a shows its chemical structure and some physical properties. PC is colorless at room temperature and can be supercooled easily. The glass transition temperature T_g, melting temperature T_m, and boiling temperature T_b of PC are 160 K, 218 K, and 513 K [73-74] respectively. Its formula weight is 102.09 and specific gravity is 1.189. The vapor pressure is 0.13 mm at 20 °C.

Simeral and Amey [75] measured the density ρ(T) and refractive index n(T) as a function of temperature:

$$\rho(T) = 1.541 - 1.148*10^{-3}T \ (g/cm^3),$$

$$n(T) = 1.53314 - 3.752*10^{-4}T .$$

The viscosity of PC was studied by Bondeau and Huck [76] from 157 K to 343 K. Masood et al.[77] and Du et al.[22] measured the sound velocity at low frequency limitation using the pulse-echo technique. The dielectric properties of PC have been studied extensively due to its importance in electrochemical and secondary battery applications.

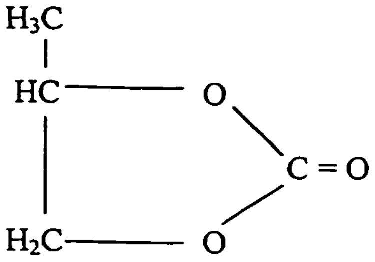

$T_m = 218K$

$T_C = 187K$

$T_g = 160K$

Figure 4-1a The chemical structure of Propylene Carbonate (PC) with the melting, crossover, and glass transition temperatures

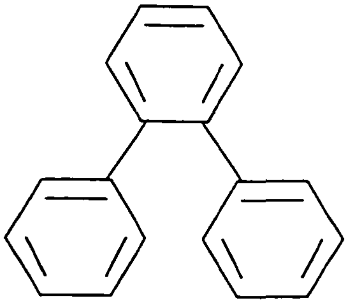

$T_m = 329K$

$T_C = 290K$

$T_g = 243K$

Figure 4-1b The chemical structure of Orthoterphenyl (OTP) with the melting, crossover, and glass transition temperatures

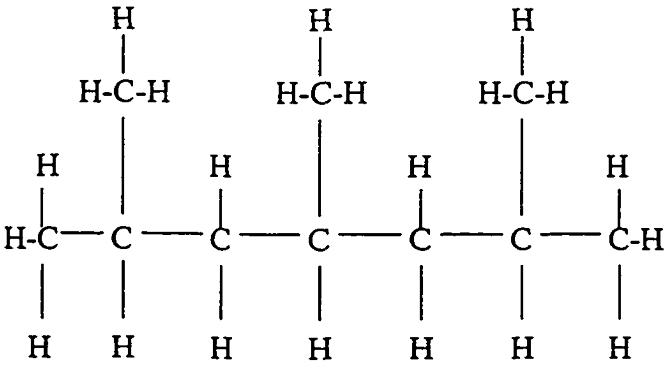

$T_m = 219K$

$T_C = ?$

$T_g \sim 125K$

Figure 4-1c The chemical structure of 2,4,6-Trimethyl-heptane (TMH) with the melting, crossover, and glass transition temperatures

Orthoterphenyl (OTP)

Orthoterphenyl (1,2-di-phenylbenzene, $C_{18}H_{14}$) is a fragile (m = 81) molecular glass-forming material with glass transition temperature $T_g = 243$ K, melting temperature $T_m = 329$ K, and boiling temperature $T_b = 605$ K [3, 45, 16]. Its formula weight is 230.30. OTP is a good material for light scattering studies of liquid-glass transition because of its high glass transition temperature and high scattering intensity. Many physical and chemical properties of OTP have been measured in the supercooled region. OTP consists of well-defined molecular units (three connected Benzene rings, Fig. 4-1b) and the intermolecular interaction is short-range Van der Waals force. OTP also shows a little tendency to crystallization.

There are many studies with different techniques on OTP. D'Arrigo [79] measured the ultrasonic velocity $C_0(T)$, density $\rho(T)$, and specific heat at constant pressure $c_P(T)$ as a function of temperature:

$$C_0(T) = 1454.6 - 3.37\,(T-54.5) \qquad \text{m/s},$$

$$\rho(T) = 1.0546 - 7.40 * 10^{-4}\,(T-54.5) \qquad \text{g/cm}^3,$$

$$c_P(T) = 64.17 + 0.107\,(T-26.87) \qquad \text{cal/mol K}.$$

Cohen and Grest [80] obtained a theoretical viscosity η of OTP as a function of temperature with the free volume theory

$$\log(\eta) = A + \frac{2B}{T - T_0 + [(T - T_0)^2 + 4v_0\zeta_0 T]^{1/2}},$$

where $A = -2.65$, $2B = 253$, $T_0 = 278.7$, and $4v_0\zeta_0 = 6.4$. Lin and Wang [45] found that the refractive index n(T) of OTP is given by:

$$n(T) = 1.824 - 5.6*10^{-4}\,T\,.$$

Naoki and Koede [81] obtained the coefficient of thermal expansion $\alpha(T)$. Cheng and Bestul [82] also reported studies on the thermal properties of OTP.

To study the dynamic properties of OTP, Wang and co-workers performed a series of VV and VH Brillouin experiments at a wide temperature range with different scattering angles [44-46]. Fytas et al. [78] and co-workers measured the photon correlation spectra. Malhotra and Pethrick [84] carried out a series of dielectric measurements on OTP. Lewis [85] did many computer simulations to study orientation fluctuations and density fluctuations. The susceptibility spectra of OTP in a wide frequency range were obtained from neutron [86-87] and depolarized light scattering [24, 48] experiments to test the mode coupling theory (MCT).

Trimethyl-Heptane (TMH)

TMH (2,4,6-trimethyl-heptane, $C_{10}H_{22}$) is an alkane glass-forming material with melting temperature T_m = 219 K, boiling temperature T_b = 418K, and glass transition temperature $T_g \sim$ 125K [49]. It has specific gravity ρ = 0.7225 and refractive index n = 1.4071 at 25°C. TMH is colorless at room temperature. The density and viscosity as a function of temperature were measured by Carroll and Patterson [49] and given by

$$\rho(T) = 0.9558 - 7.946*10^{-4}*T \qquad g/cm^3,$$

$$\eta(T) = 0.01514 \exp(1154/T) \qquad cP.$$

Most of the physical and chemical properties of TMH are unknown because very few studies on this material have been reported, but several new studies are currently in progress.

The most important characteristics of TMH is that its depolarized light scattering intensity I_{VH} is much weaker than the polarized light scattering intensity I_{VV} as found by Carroll and Paterson in a Brillouin scattering study [49]. This means that we can treat the polarized spectrum of TMH as an isotropic spectrum so that the data analysis procedures become much simpler.

B. Sample preparation and Temperature control

Sample preparation

PC of > 99% purity with water content < 0.005% was purchased from Aldrich Chemical Company. Samples used for the experiments were obtained from fractional distillation under reduced pressure [22]. OTP also was purchased from Aldrich with purity > 99% and then filtered (filter size: 0.2μm) into sample cells.

TMH was purchased from Wiley Organics with purity > 99%. To avoid crystallization at low temperature due to the impurities, it was distilled into sample cells directly and the sample cells were sealed under vacuum.

Temperature control

As mentioned before, when liquids are in supercooled state, the dynamic properties of liquids change so extensively that the scattering spectra change rapidly with changing temperature . Therefore, it is important to control the temperature of the sample accurately to obtain a reliable spectrum.

In experiments, the temperature of samples was regulated by a temperature controlling system which includes an Oxford ITC4 temperature controller with a temperature accuracy of 0.1K and an Oxford DN1754 cryostat in a temperature range of 96K to 450K. Liquid nitrogen was used to decrease the temperature and a heater in the cryostat was used to increase the temperature.

Sample cell and holder

The sample cells are cylindrical glass cells made of pyrex glass tubes with two sizes: one is 18mm in diameter (outside) and 15mm in height and another is 8mm (outside) in diameter and 15mm in height. Before filled with samples, sample cells had been immersed in a chromerge solution for 8 hours, and then flashed with distilled water to remove any contamination.

The sample cell was put in a copper sample holder, shown in Fig.4-2, which was screwed onto the cooled finger of the cryostat. To keep good thermal contact, we placed an indium wire between the sample holder and the finger of the cryostat and Cry-Con grease on the bottom of the sample cell. In experiments, we usually wait 15 - 30 minutes after changing the sample temperature in order to obtain thermal equilibrium.

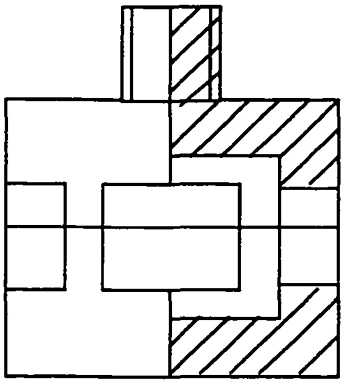

Figure 4-2 Schematic diagram of the sample holder

C. Brillouin Spectra and Fitting Results for OTP and PC

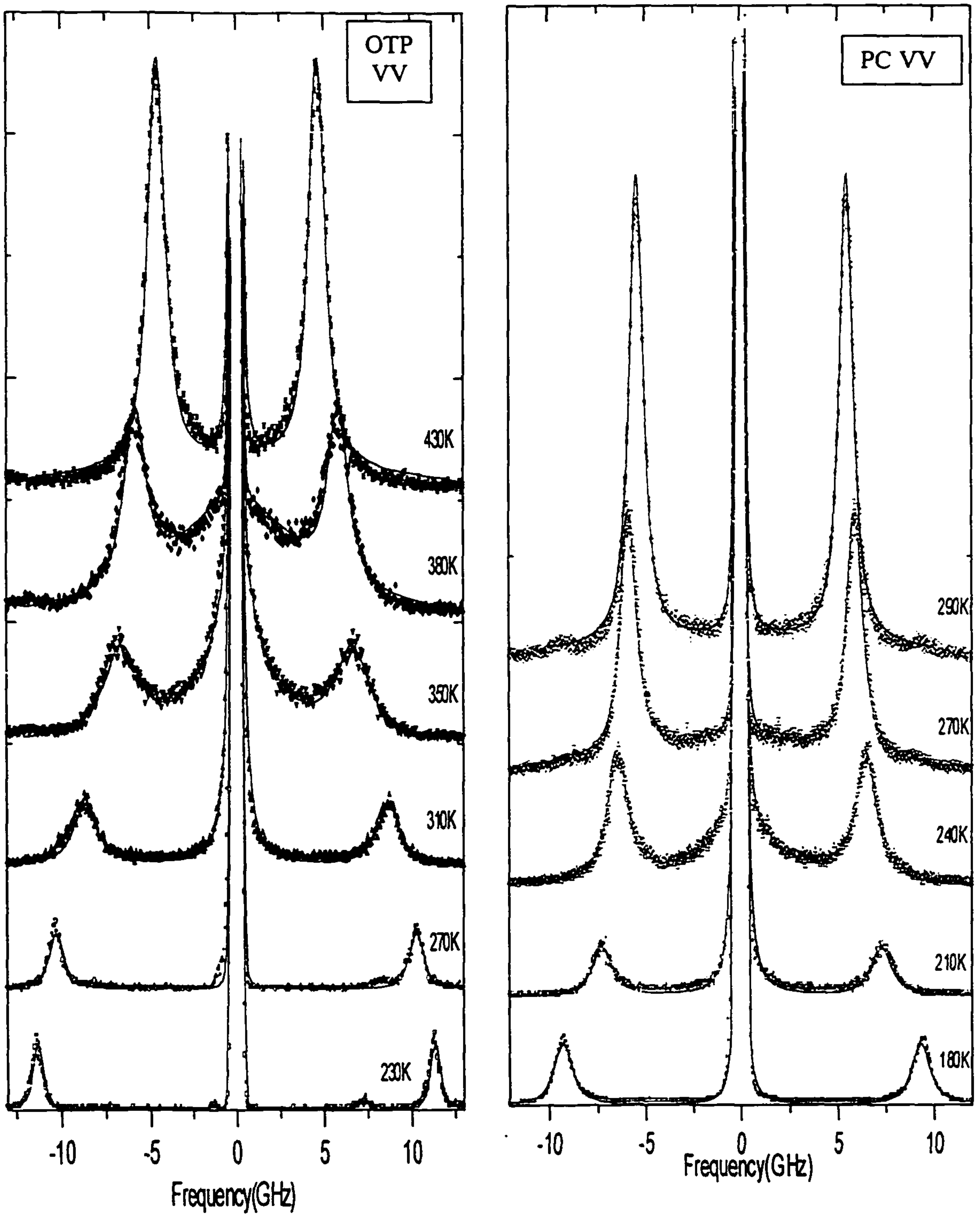

Figures 4-3a and b The VV spectra of PC (left) and OTP (right) with 4 Lorentzians fits

The Brillouin spectra of OTP and PC

The polarized and depolarized Brillouin spectra of OTP from 230 K to 430 K and PC from 160 K to 350 K were measured at $\theta = 90^0$. Figs. 4-3a and b show the polarized spectra of OTP and PC at some temperatures. The solid lines are the 4-Lorentzian fitting curves. The spectrum of OTP at T= 430K (top one) has the typical Brillouin triplet structure: a central (unshifted) Rayleigh component which is due to entropy fluctuations (too strong to plot the entire component) and two symmetrical Brillouin components with frequency shifts $\omega = \pm$ vk due to the propagating longitudinal sound waves. As OTP and PC were cooled, an additionally central component (Mountain mode plus orientational contributions) was observed and its linewidth $\Delta\omega_M$ became narrower with decreasing temperature.

First, we treated those VV spectra as isotropic spectra and analyzed them using the procedures discussed in Chapter 2. We fitted the VV spectra of PC and OTP using the 4 Lorentzians, Mountain theory, and generalized hydrodynamic equation with Cole-Davidson function. In the generalized hydrodynamic equation with the Cole-Davidson function fits, β_{CD} values obtained from fitting α-relaxation peaks of susceptibility spectra were fixed. The β_{CD} values for OTP and PC were 0.6 and 0.7 respectively. The relation between the Cole-Davidson stretching exponent β_{CD} and the Kohlrausch stretching exponent β_K has been given by Lindsay and Patterson [88]. Figs.4-4a and b show the generalized hydrodynamic equation fitting curves with the Brillouin spectra of PC and OTP at some temperatures.

The Brillouin peaks

The measured Brillouin shift ω_B with the computed high and low frequency limits ω_∞ and ω_0 are shown in Fig. 4-5a for OTP and Fig. 4-5b for PC. The linewidths of the Rayleigh mode $\Delta\omega_R$, Mountain mode $\Delta\omega_M$, and Brillouin mode $\Delta\omega_B$ from the 4-Lorentzian fit were plotted in Fig. 4-6a for OTP and Fig. 4-6b for PC. When the

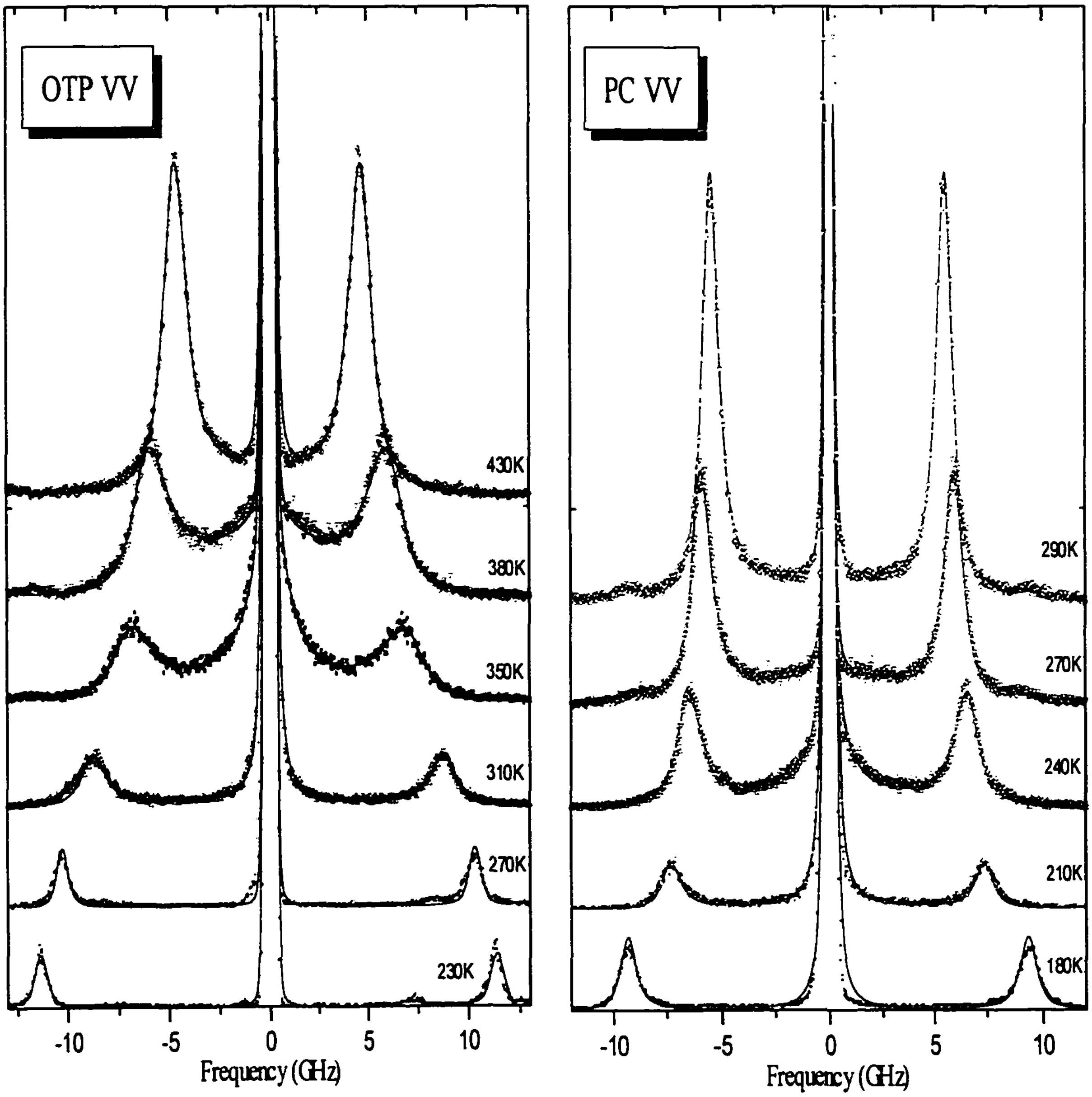

Figures 4-4a and b The VV spectra of OTP (left) and PC (right) with generalized hydrodynamic equation fits

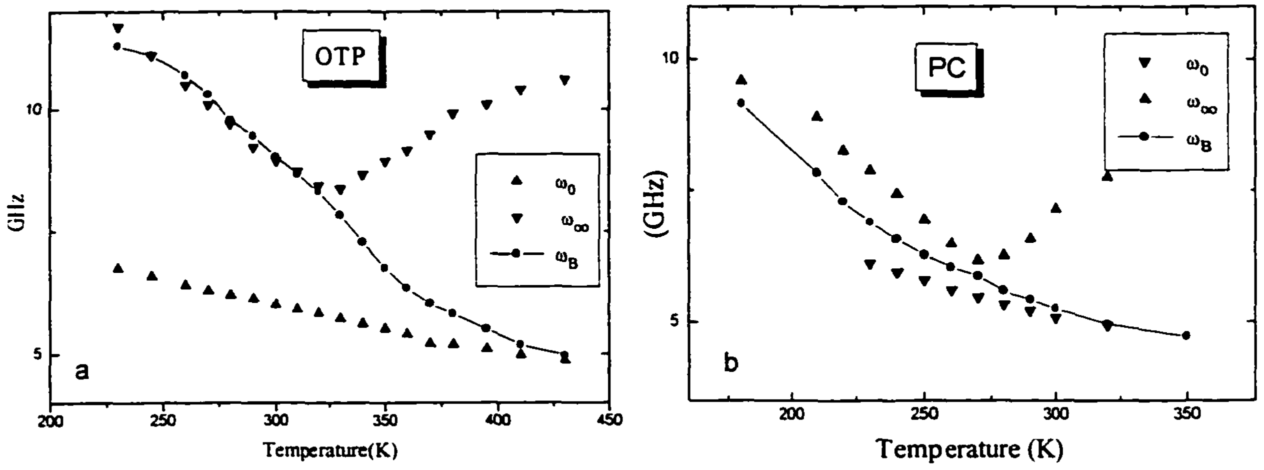

Figures 4-5a and b The ω_B with high and low frequency limits of OTP and PC

temperature is decreased, the linewidth of the Rayleigh mode $\Delta\omega_R$ did not change significantly. However, the linewidth of the Mountain mode $\Delta\omega_M$ changed from very broad at high temperature to narrow and finally merged with the Rayleigh peak. The linewidth of the Brillouin mode $\Delta\omega_B$ increased and reached a maximum at T = 350K for OTP and T = 240K for PC, and then decreased. Conversely, the intensities of the Brillouin peaks decreased to a minimum and then increased.

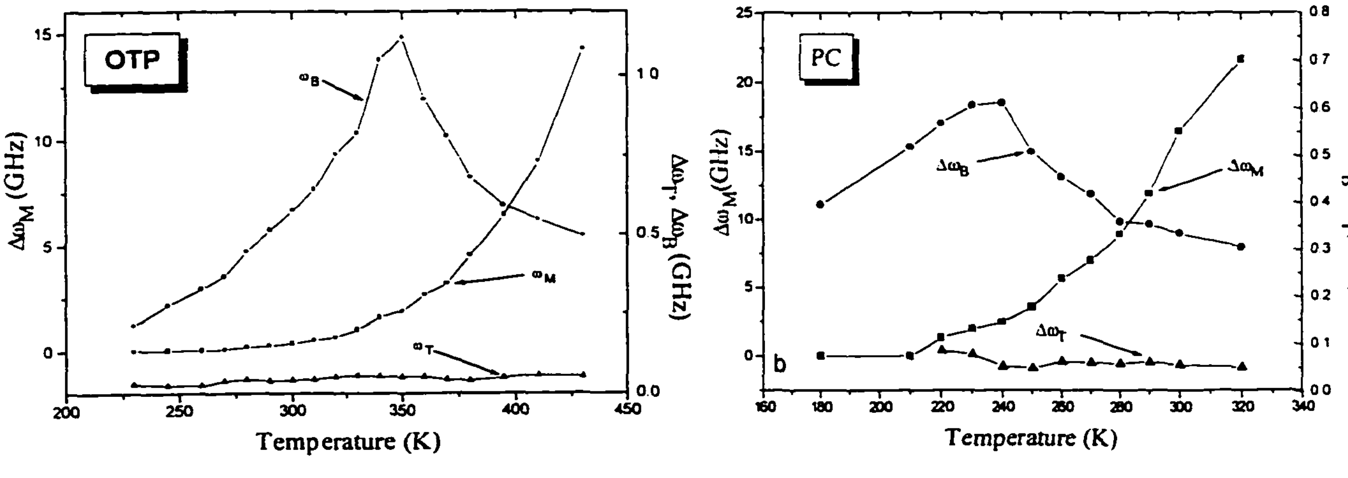

Figures 4-6a and b Linewidths of Rayleigh mode $\Delta\omega_T$, Mountain mode $\Delta\omega_M$, and Brillouin mode $\Delta\omega_B$ of OTP and PC

The Landau-Placzek ratio of OTP and PC was calculated from the integrated intensities of Rayleigh and Brillouin components by Eq.[2.13] and shown in Figs. 4-7a and 4-7b respectively. The ratio of specific heats of OTP and PC obtained from the Mountain theory fits was also plotted as a function of temperature in Fig. 4-7. These results agree with other studies but are much larger than expected from the theory. Fischer [84, 89] suggested an explanation of this behavior by introducing an additional order parameter in the melt whose fluctuation gives rise to 'excess' scattering (Fischer cluster).

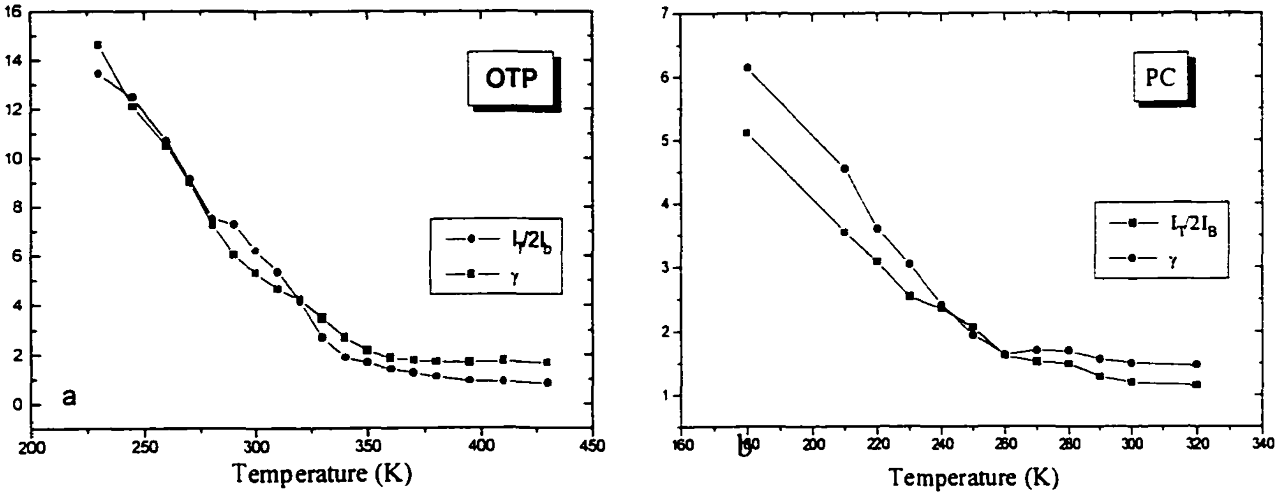

Figures 4-7a and b The Landau-Placzek ratios and the ratios of specific heats of OTP and PC

For both OTP and PC, relaxation time τ obtained from the generalized hydrodynamic equation was shorter than that obtained from the Mountain theory fits at high temperature as discussed in Chapter 2. Figs. 4-8a and b show the relaxation time for OTP and PC obtained from different fitting procedures as a function of temperature: •-symbols are from the Mountain theory fits and ■-symbols are from the generalized hydrodynamic equation fits.

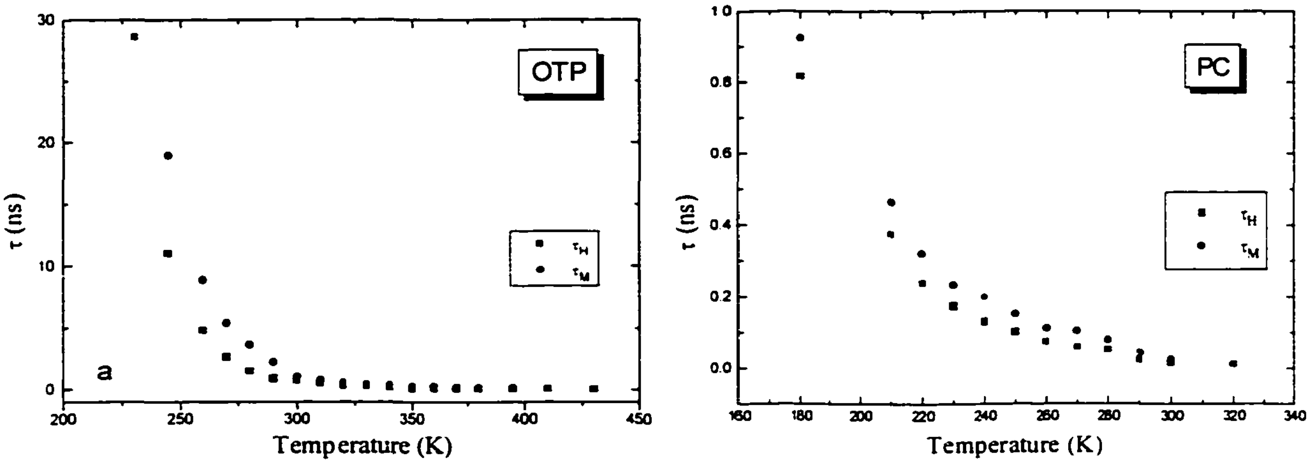

Figures 4-8a and b Relaxation time τ of OTP and PC

The high and low frequency limits (ω_∞ and ω_0)

In the data analyses, ω_0 was fixed due to the strong correlation between ω_0 and ω_∞ and the value of ω_0 for OTP was calculated from the ultrasonic velocity C_0^u measured by D'Arrigo [79] and for PC from the ultrasonic measurements of Du et al.[22]. The scattering vector q is determined by Eq.[1-3]. ω_∞ was calculated from $\omega_\infty^2 = \omega_0^2 + \Delta^2$ and Δ^2 was treated as a free fitting parameter. The longitudinal sound velocity C_B of OTP was plotted as a function of temperature with the high frequency limiting velocity C_∞

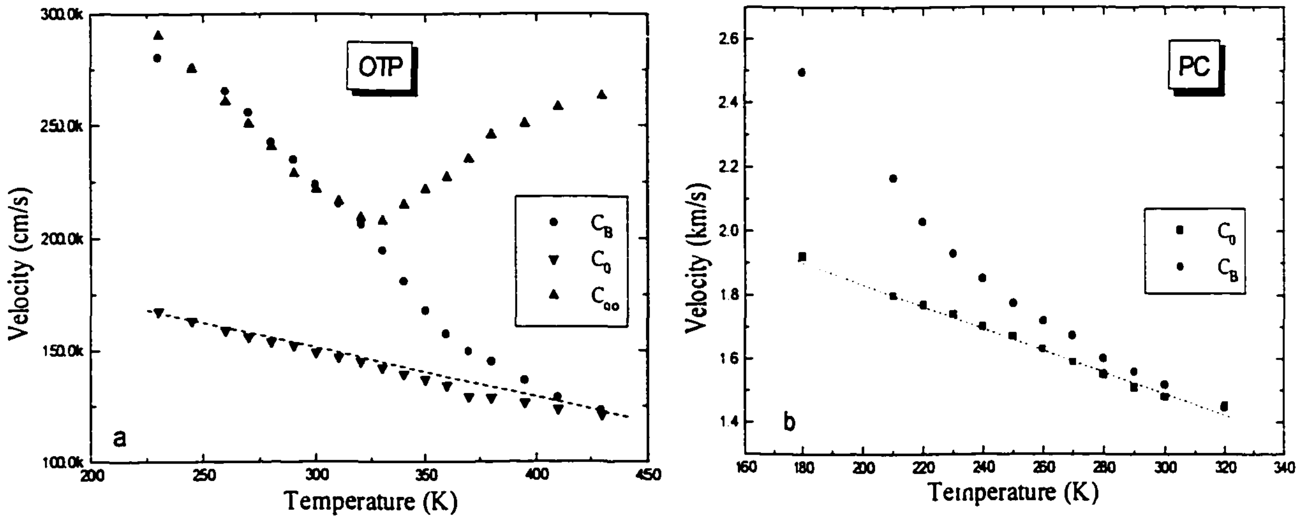

Figures 4-9a and b The longitudinal sound velocity C_B with high C_∞ and low C_0 frequency limiting velocities of OTP and PC. The dashed lines are the ultrasonic data.

and the ultrasonic velocity C_0^u in Fig. 4-9a. Fig. 4-9b plots the longitudinal acoustic velocity and the ultrasonic velocity C_0^u measured by Du et al.[22] of PC as a function of temperature. It shows that the ultrasonic velocity C_0^u is close to the longitudinal sound velocity C_B at high temperature (low frequency), while C_B approaches the high frequency limit velocity C_∞ at low temperature. To compare the fitting results, we also fitted the Brillouin spectra with both ω_0 and ω_∞ as free fitting parameters. The low frequency limit velocity C_0 obtained from ω_0 is also shown in Fig. 4-9. These two curves were only slightly different which indicates that the fitting results are reliable.

Determining the nonergodicity factor $f_q(T)$

The nonergodicity factor $f_q(T)$ at long wavelength can be calculated from the Brillouin spectrum by [90]:

$$f_{q\to 0} = 1 - \left(\frac{C_0}{C_\infty}\right)^2 = 1 - \left(\frac{\omega_0}{\omega_\infty}\right)^2, \qquad [4.1]$$

The resulting $f_0(T)$ values for OTP and PC were plotted in Figs. 4-10a and b. Both figures show that there is a possible cusp which indicates the crossover temperature T_C of MCT ($T_C \sim 290$ K for OTP and $T_C \sim 200$ K for PC). However, the apparent T_C values are somewhat different from the values ($T_C \sim 288$ K for OTP and $T_C \sim 187$ K for PC) obtained by other methods. The T_C values found from this procedure strongly depend on the choice of β [90]. There was a $f_0(T)$ minimum at T ~ 220K for PC and T ~ 300K for OTP. The nonergodicity factors $f_0(T)$ also can be calculated from the integrated intensity of the Brillouin modes by

$$f_0(T) = 1 - AI_B(T) / T, \qquad [4.2]$$

where A is a temperature-independent constant [90]. Therefore, the nonergodicity factor $f_0(T)$ can be determined directly by measuring the integrated intensity of the Brillouin peak (up to a constant A).

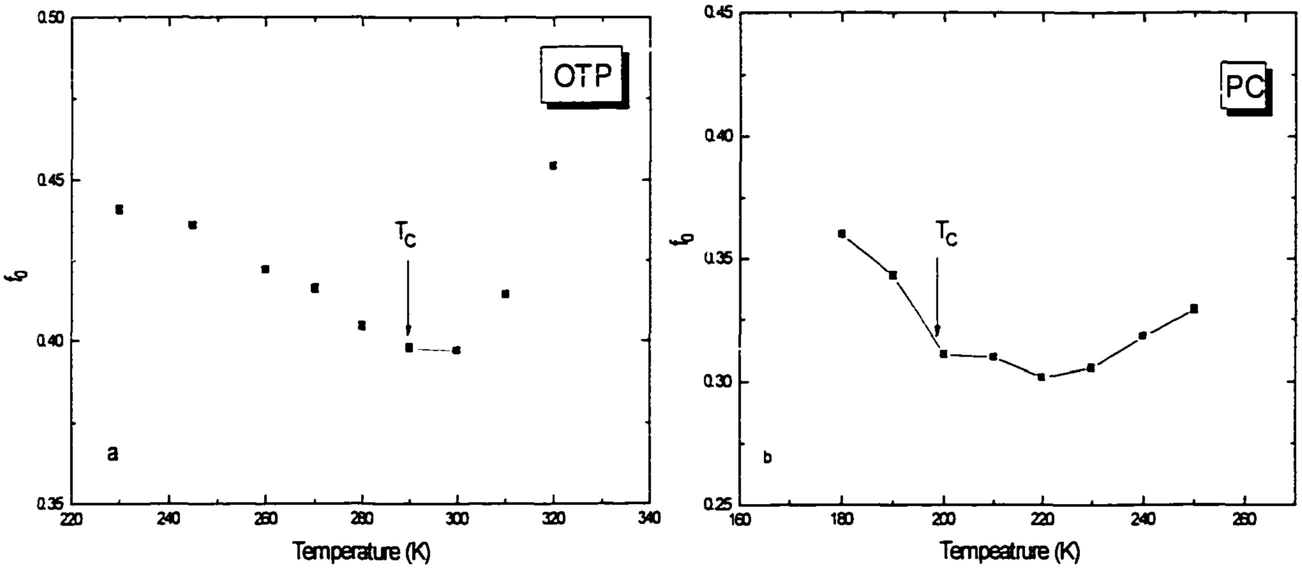

Figures 4-10a and b The nonergodicity factors of OTP and PC

Polarized, Depolarized, and Isotropic Spectra

While the VV spectra always exhibit a longitudinal acoustic mode, the VH spectra exhibit a transverse acoustic mode only when the temperature is low enough for $\omega\tau \geq 1$ to be valid. The VH spectra of OTP and PC have been shown in Fig. 1-7. The transverse mode can be observed at low temperature range. With decreasing temperature, the frequency shift and the intensity of transverse mode increase, and the linewidth of transverse mode decreases. Since the transverse modes are very weak, it is difficult to analyze accurately. We did not observe any central dip at high temperature range in both OTP and PC, in contrast to salol which exhibits a prominent central dip at high temperatures.

The isotropic spectra of PC and OTP were obtained from the VV and VH spectra using Eq.[2.41]. The constant (4/3), determined from the measured depolarization ratio is 1.28 for OTP and 1.24 for PC. The VV spectra I_{VV}, the VH spectra I_{VH}, and the isotropic spectra I_{ISO} of OTP at T = 350 K and PC at T = 240 K were shown in Figs. 1-4 and 2-13 respectively. Note that the isotropic spectra is quite different from the VV spectra at low frequency region, indicating that orientational fluctuations and second order density fluctuations make significant contributions to the VV spectrum. The isotropic spectra were fitted using the 4-Lorentzian, Mountain theory, and generalized hydrodynamic equation with the Cole-Davidson function. We found that the Mountain mode was very weak and the fitting results became worse. This is because Eq.[2.41] is valid only when the orientational fluctuations and transverse shear waves are independent but they couple with each other in both OTP and PC. Similar results were also found by other studies. More sophisticated analyses which include translation-rotation coupling have been proposed, but not yet tested.

However, if we can find a material in which the depolarized scattering intensity is much weaker than the polarized scattering intensity, we can treat a VV spectrum as an isotropic spectrum in a good approximation and apply all procedures discussed in Chapter 2 to this VV spectrum directly.

D. Physical properties of TMH

Carroll and Patterson [49] measured the VV and VH Brillouin spectra of TMH at supercooled region and found that the VH spectrum was so weak that it cannot be observed on the same scale as that used for the VV spectrum. This suggests that the scattering contributions of orientational fluctuations in TMH are so weak that we can treat a VV spectrum as an isotropic spectrum. Therefore, TMH is a good material for the light scattering study on the liquid-glass transition. Unfortunately, most physical and chemical properties of TMH are unknown.

Density of TMH

We measured some physical properties of TMH. The density as a function of temperature was determined by measuring the volume change with temperature. A TMH sample was filled into a volumetric flask (volume ~ 3 ml) with graduated neck (accuracy < 0.1 ml). This volumetric flask was put into a cooling system (temperature accuracy < 1K). The volume change was recorded as a function of temperature, and then converted to the density change. Table 4-1 gives the density and thermal expansion coefficient of

Table 4-1. The density and thermal expansion coefficient of TMH

T(K)	V(ml)	α (10^{-4})(K^{-1})	ρ (g/ml)
296	2.53		.701
286	2.51	8.5	.707
266	2.465	9.4	.719
251	2.435	8.1	.728
238	2.405	9.8	.737
231	2.39	8.5	.742
224	2.375	9.7	.746
218	2.36	10.1	.752
204	2.33	9.3	.761
181	2.28	9.6	.778
158	2.23	9.4	.795

TMH at different temperatures. To reach the thermal equilibrium, we waited more than 15 minute for each temperature change.

The thermal expansion coefficient $\alpha = (1/V)(dV/dt)$ was also calculated. Fig. 4-11 shows the density and expansion coefficient versus temperature. The density varies linearly with temperature while the thermal expansion coefficient remains constant. A linear function was used to fit this density data. The density of TMH as a function of temperature was given in a temperature range from 294K to 150K:

$$\rho(T) = 0.902 - 6.9 \times 10^{-4}T .$$

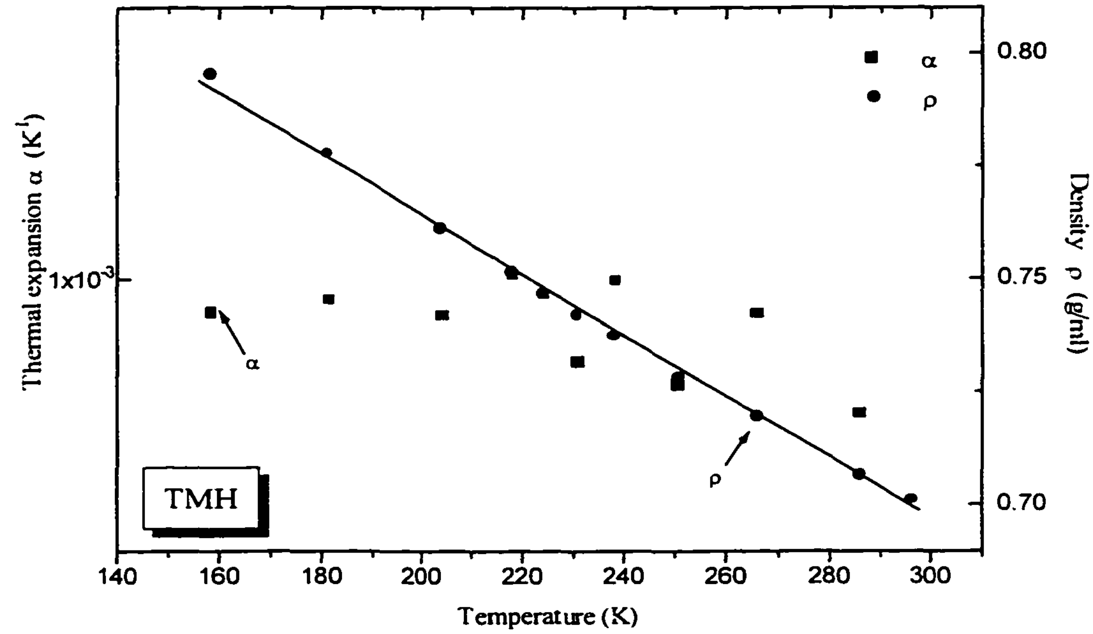

Figure 4-11 The density and expansion coefficient of TMH

Refractive index

The refractive index of TMH was measured by light deviation method. This experiment was carried out in our laboratory by Dr. J. Henandez. Fig. 4-12 shows a schematic diagram of this apparatus. A TMH sample was filled into a triangular prism cell. The angles of the prism are 45^0, 45^0, and 90^0. One of the 45^0 angles was used as the refraction angle A. Since X and Y (~ 1m) were much larger than the size of the cell, the deviation angle was determined approximately by $\delta_m = \tan^{-1} Y/X$. This cell was

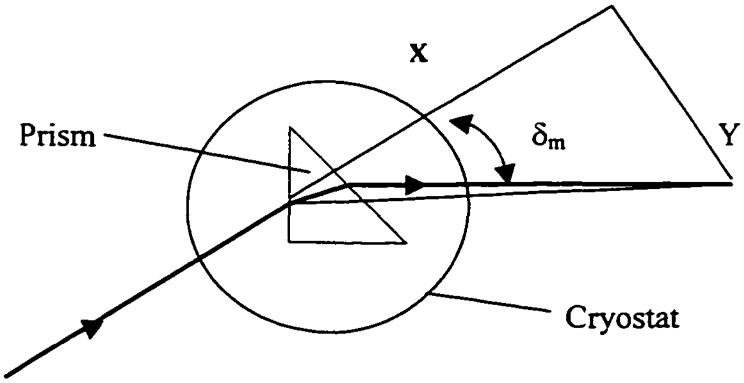

Figure 4-12 Schematic diagram of refractive index measurement

placed in a cryostat and connected with the finger of the cryostat directly. To obtain a precise temperature, an extra thermocouple (GB31P2, Fenwal) was attached at the middle of the cell where light passes through. The cryostat was mounted on a rotating base. We can always find a minimum deviation angle by rotating the base. The refractive index n was calculated by the deviation equation:

$$n = \frac{\sin(A/2 + \delta_m)}{\sin(A/2)} \qquad [4.3]$$

To test our apparatus, some materials with known refractive index values were measured at different temperatures. Differences of the results were less than one percent. The refractive index of TMH was obtained in a temperature range from 294 to 200 K. Table 4-2 gives the data of the deviation angle δ_m and the refractive index n of TMH at different temperatures. The refractive index versus temperature was plotted in Fig. 4-13 and fitted by a linear function: $n(T) = 1.5344 - 4.4 \times 10^{-4} T$.

Table 4-2. Refractive index of TMH

T (K)	$\delta_m(^0)$	n
199	11.12	1.447
214	10.97	1.440
232	10.76	1.432
251	10.55	1.424
276	10.26	1.413
294	10.04	1.405

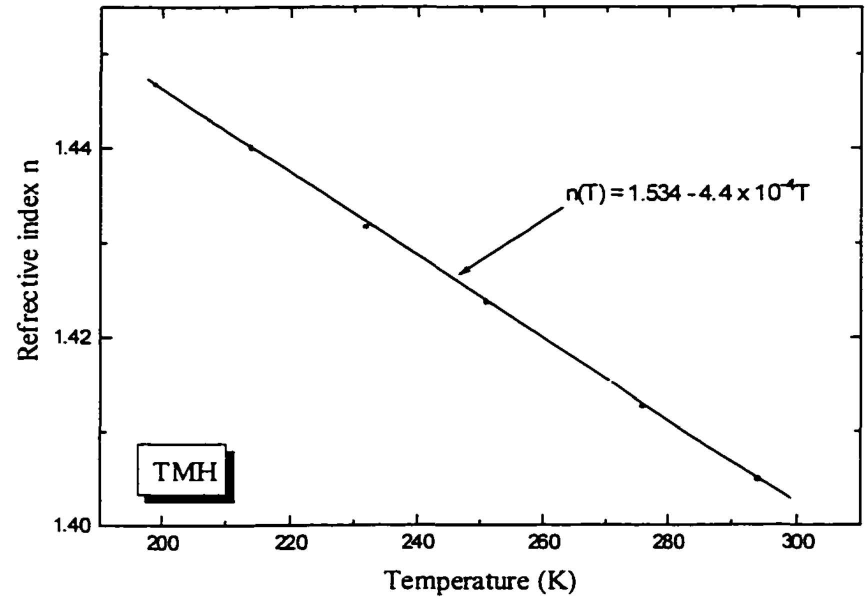

Figure 4-13 Refractive index and fitting function of TMH

To test our results, the refractive index n was also converted to the density by the Lorentz-Lorentz relation:

$$\rho(T)=C\left[\frac{n(T)^2-1}{n(T)^2+2}\right] \qquad [4.4]$$

where $C = 2.94$ was determined by the values of density and refractive index at $T = 294K$. Fig. 4-14 shows the converted density using Eq. [4.4] and the density obtained from last section. The two results are in a good agreement.

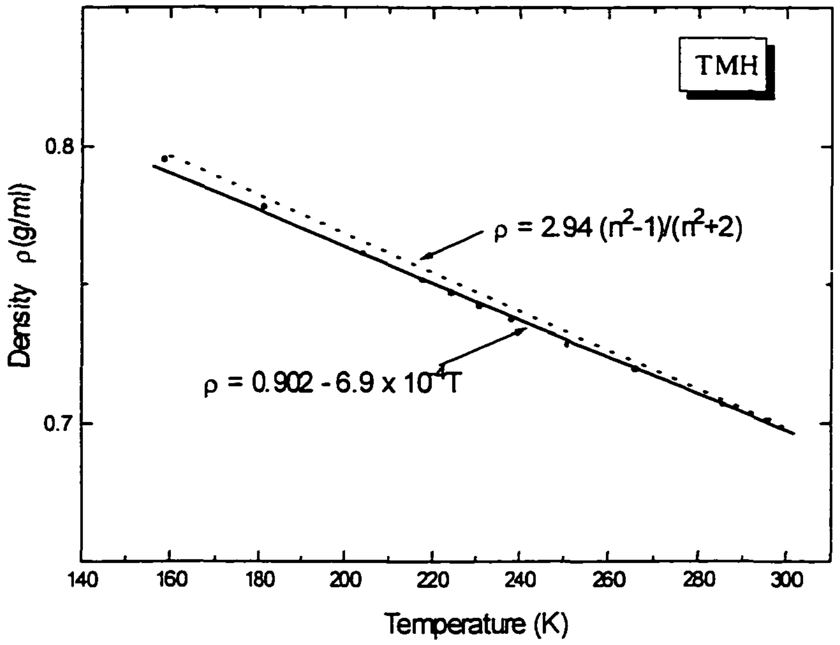

Figure 4-14 The converted density (dashed line) and density (solid line) of TMH

Ultrasonic velocity and specific heat of TMH

The ultrasonic velocity of TMH was measured in a preliminary experiment by Prof. J. Toulouse and P. Finkel at Lehigh University using the phase-sensitive technique [91]. The phase-sensitive technique provides absolute and relative velocity measurements with a very high accuracy ($\Delta v/v \sim 0.01\%$) [92]. The ultrasonic velocity was obtained only at high temperature because the signal disappeared at low temperature due to attenuation. Fig. 4-15 shows the ultrasonic velocity data as a function of temperature. The ultrasonic velocity C_0 was fitted by a linear function:

$$C_0 = 2474.4 - 4.4T \qquad \text{(m/s)}$$

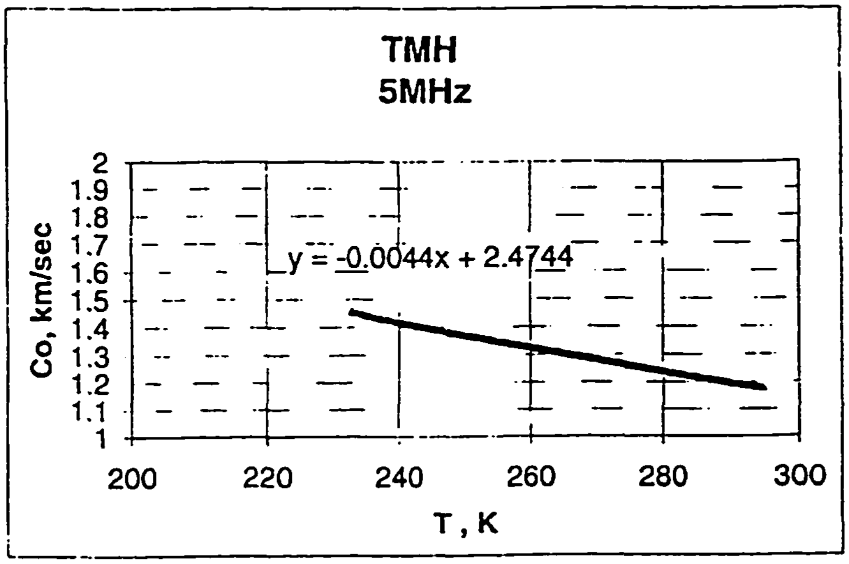

Figure 4-15 Ultrasonic velocity of TMH [93]

The specific heat at constant pressure c_p of TMH was measured by Prof. C. Ecolivet using DSC (differential scanning calorimetry) at the University de Rennes, France. Fig.4-16 shows a preliminary specific heat curve against temperature. A clear glass transition signature can be observed at T ~ 125 K. This glass transition temperature confirms Carroll and Patterson's result [49].

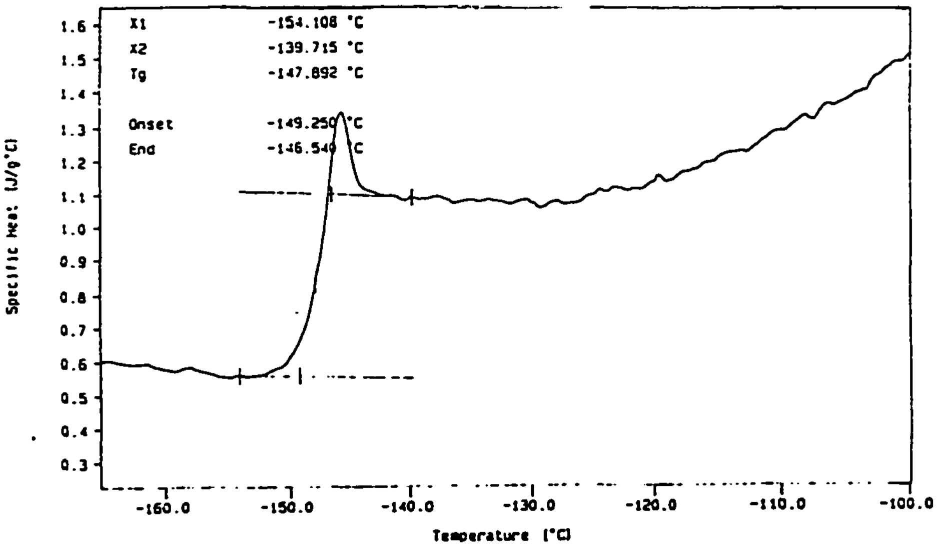

Figure 4-16 Specific heat at constant pressure of TMH [94]

E. Density and Orientational Fluctuations

The relative importance of density and orientational fluctuations

To test the relation of scattering intensities between the orientational fluctuations and density fluctuations, we compared the Rayleigh ratio R_{VH}^{exp}, the geometry-independent scattering cross section per unit volume, to the computed Rayleigh ratio due to the Dipole-Induced-Dipole (DID) scattering R_{VH}^{DID} using $CHCl_3$ as a reference material. In this section, Dr. Y.H. Hwang measured the Raman spectra of TMH and $CHCl_3$. He also did part of the calculations. Patkowski and co-workers suggested that the DID effects only contribute to the low frequency part of the depolarized light scattering spectrum [96].

The polarized and depolarized light scattering intensities were measured in the frequency range from 0.03 to 4000 GHz at room temperature with $\theta = 90^\circ$. For low frequency range (0.03 ~ 400 GHz), the Sandercock TFPI was used with three different free spectral ranges (FSR): 7.5, 50, and 500 GHz. For the high frequency range (200 ~ 4000 GHz), a Spex 1401 Raman spectrometer was used. The spectra in different FSRs were combined into a large frequency range spectrum using the overlapping method [97]. The spectra with FSR = 7.5 GHz were used as intensity references.

We used a constant intensity which was calculated from the average value of low frequency range (0.03 ~ 0.04 GHz for VV spectra and 0.5 ~ 0.6 GHz for VH spectra) to extrapolate the spectra to zero frequency. Figs. 17a and 17b show the VV and VH spectra of TMH and $CHCl_3$ in a wide frequency range (0 ~ 4000 GHz). We integrated the intensities of those spectra from 0 to 4000 GHz and the results are shown in Table 4-3.

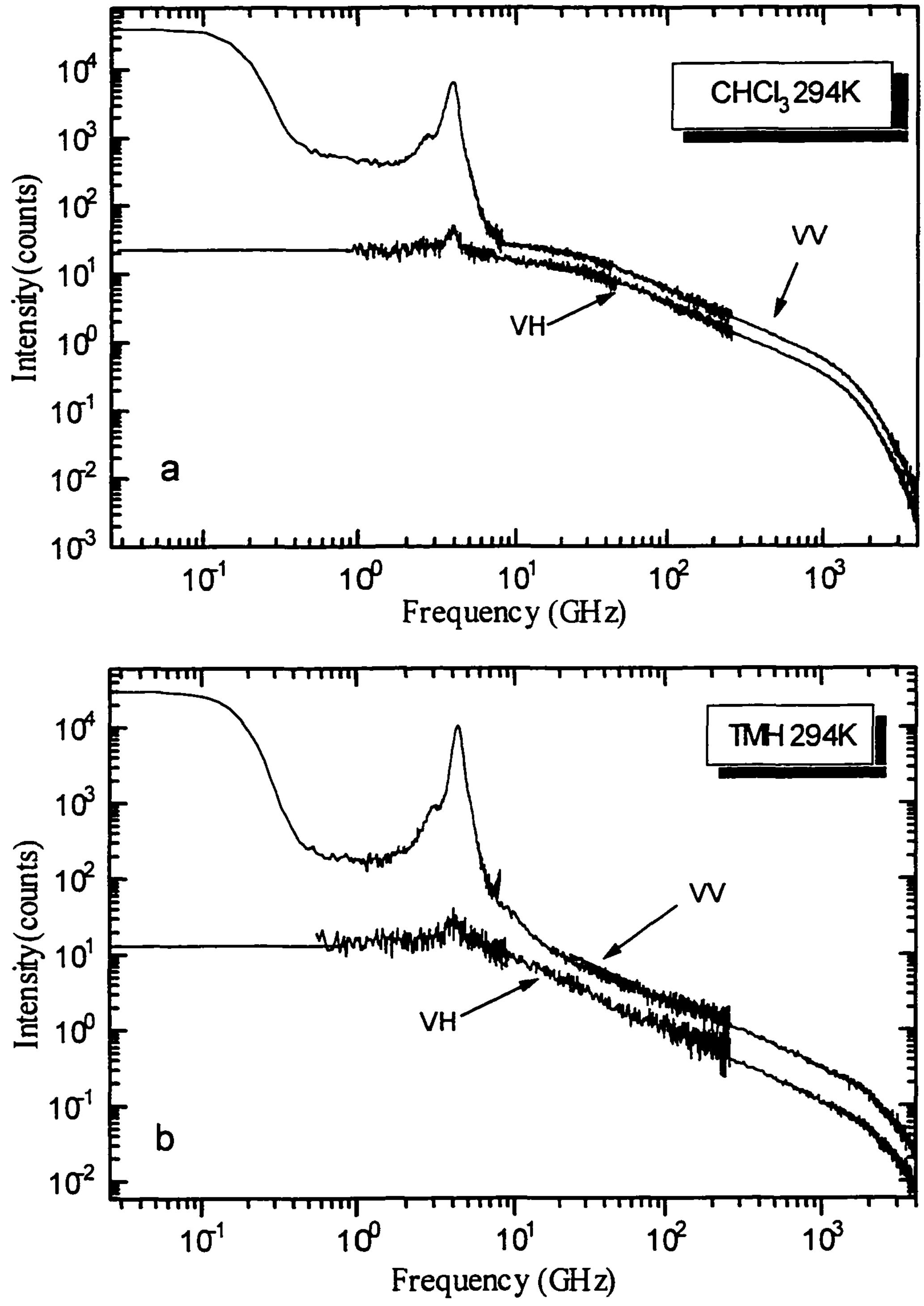

Figures 4-17a and b The VV and VH spectra of $CHCl_3$ and TMH

Table 4-3. Integrated intensity of TMH and $CHCl_3$

SAMPLE	I_{tot}^{VV} (counts)	I_{tot}^{VH} (counts)
TMH	15700	770
$CHCl_3$	17300	1970

Rayleigh ratio

Since the experimental value R_{VV}^{exp} of VV spectrum of $CHCl_3$ is known as 1×10^{-5} cm^{-1} and the integrated intensity is proportional to the Rayleigh ratio, we converted these integrated intensities to Rayleigh ratios using R_{VV}^{exp} of $CHCl_3$ as a standard reference. The R_{VH}^{DID} can be calculated by [98]

$$R_{VH}^{DID} \approx N^3 k^4 \alpha^4, \qquad [4.5]$$

where N is the number density, k is the wavenumber, and α is the polarizability determined by the Lorentz-Lorentz equation

$$\alpha = \frac{3(n^2-1)}{4\pi N(n^2+2)}, \qquad [4.6]$$

where n is the refractive index.

Rayleigh ratios of TMH and $CHCl_3$ and the ratio of $R_{VH}^{exp}/R_{VH}^{DID}$ are given in Table 4-4. For comparison, the data of the isotropic molecule CCl_4 and anisotropic glass-forming molecule salol (both from reference [98]) are also listed in Table 4-4. Comparing the $R_{VH}^{exp}/R_{VH}^{DID}$ value of TMH (~2) to that of the isotropic molecule CCl_4 (~1.4) and the anisotropic molecule salol (~30), we can conclude that the density fluctuations are more important than the orientational fluctuations in TMH. Therefore, we can treat VV spectra of TMH as isotropic spectra by ignoring the VH spectra.

Table 4-4. Experimental and theoretical Rayleigh ratio

SAMPLES	R_{VV}^{exp}(cm^{-1})	R_{VH}^{exp}(cm^{-1})	R_{VH}^{DID}(cm^{-1})	$R_{VH}^{exp}/R_{VH}^{DID}$
TMH	9.6x10^{-6}	4.5x10^{-7}	2.0x10^{-7}	2.3
$CHCl_3$	1.0x10^{-5}	1.2x10^{-6}	1.1x10^{-7}	10.1
CCl_4	9.2x10^{-6}	2.2x10^{-7}	1.5x10^{-7}	1.4
Salol	4.5x10^{-5}	1.8x10^{-5}	5.8x10^{-7}	30

Polarized and Isotropic spectra

The VV and VH Brillouin spectra of TMH were measured from 294K to 96K with a free spectral range FSR = 15GHz and at a scattering angle θ of 90^{O}. The VV spectra were obtained with a polarizer in the scattered beam because the VV spectra were

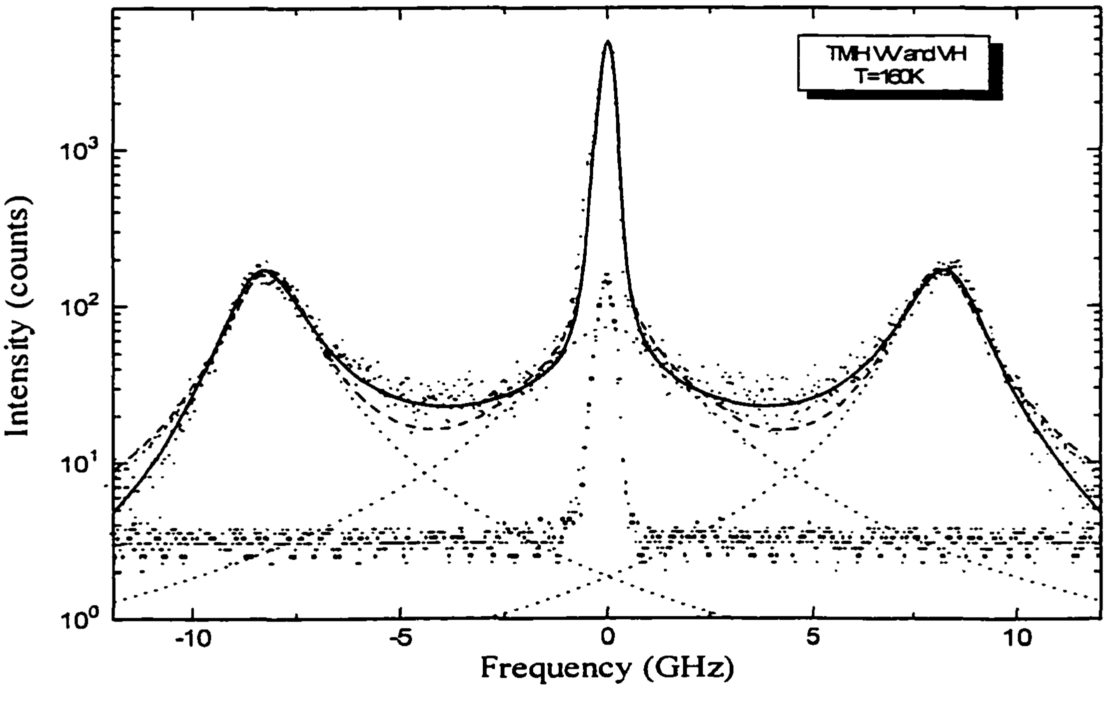

Fig.4-18a The VV and VH Brillouin spectra of TMH at 160 K. The □-symbols are the VV spectrum and the ♦-symbols are the VH spectrum. The solid line is the Mountain theory fit. The long dashed line is the 4-Lorentzian fit and the short dashed lines represent the Mountain mode and Brillouin modes.

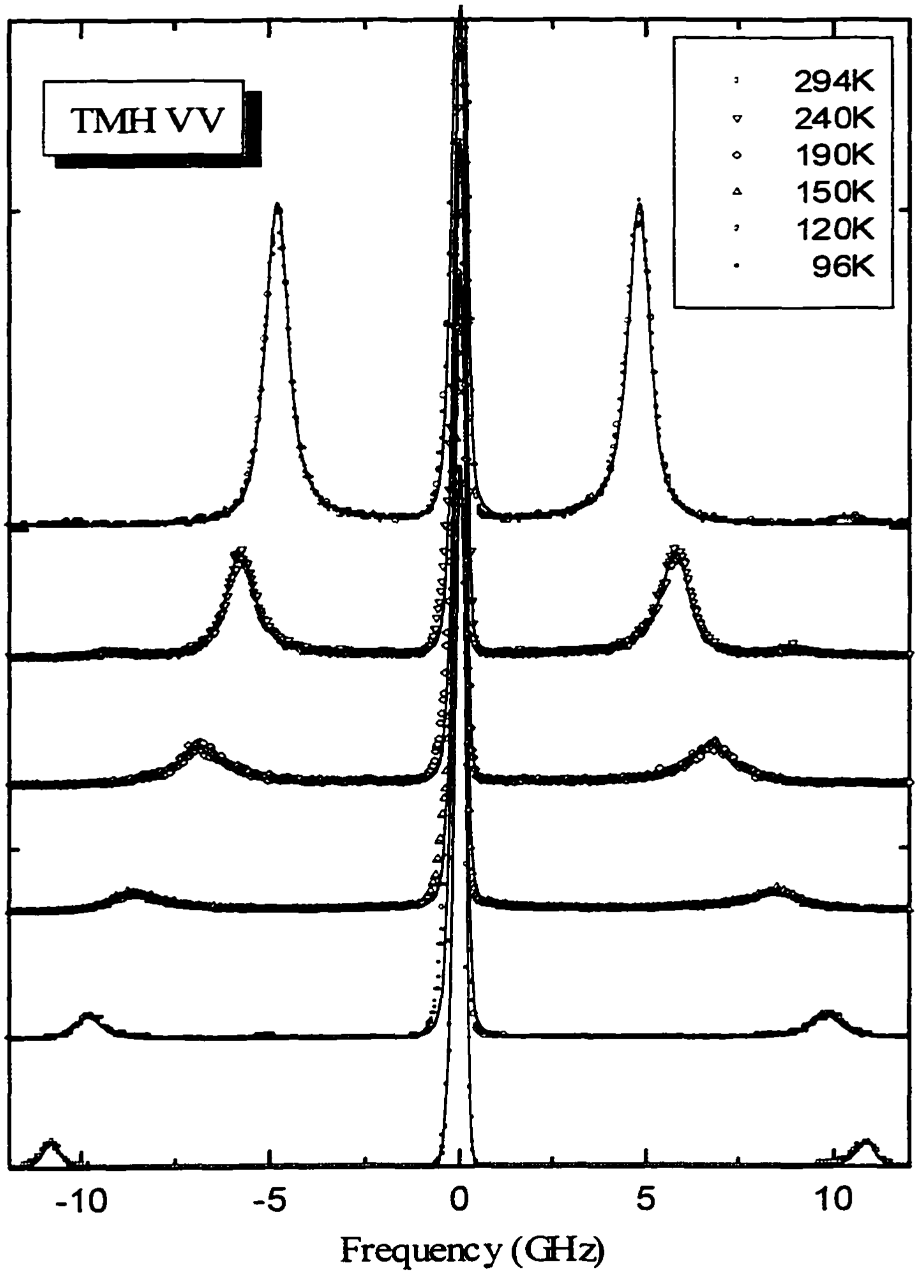

Figure 4-18b The VV Brillouin spectra of TMH with Mountain theory fits

slightly different from the spectra without the polarizer. The VV and VH Brillouin spectra of TMH at 160K were shown in Fig.4-18a. The VH spectrum was too weak to observe on the same scale as that used for the VV spectrum. So in a good approximation, we can ignore the VH spectra and treat the VV spectra as the isotropic spectra.

Figure 4-18b shows the VV Brillouin spectra of TMH at (top to bottom) 294, 240, 190, 150, 120, and 96K with Mountain theory fits. At the highest temperature, the Brillouin peaks are very strong. As found for OTP and PC, the Brillouin peak shifted to higher frequency as the temperature is decreased. The Brillouin shift ω_B is plotted with high and low frequency limits in Fig.4-19. When the sample was cooled, the linewidth of the Brillouin peak changed from narrow to broad, reached a maximum at T = 160K then

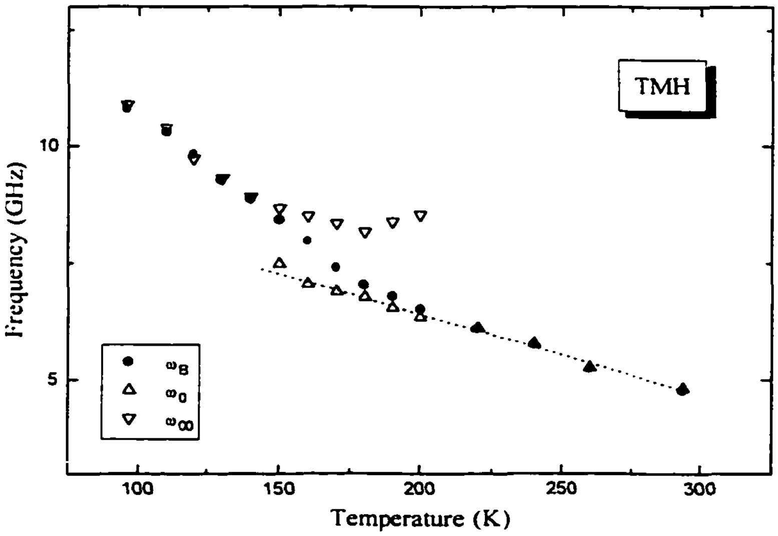

Figure 4-19 Brillouin shift ω_B with high and low frequency limits

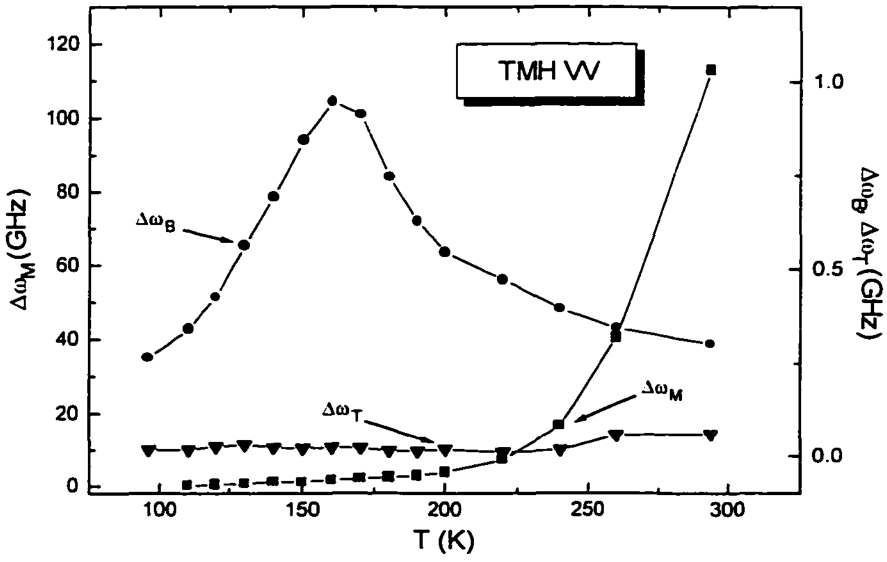

Figure 4-20 The linewidth of Mountain modes, Rayleigh modes, and Brillouin modes

narrowed again, while the intensity and linewidth of the Rayleigh peak were almost constant, as shown in Fig. 4-20. Fig. 4-21 shows the Landau-Placzek ratio of TMH obtained from the 4-Lorentzian fit and the ratio of specific heat γ which is much higher than expected.

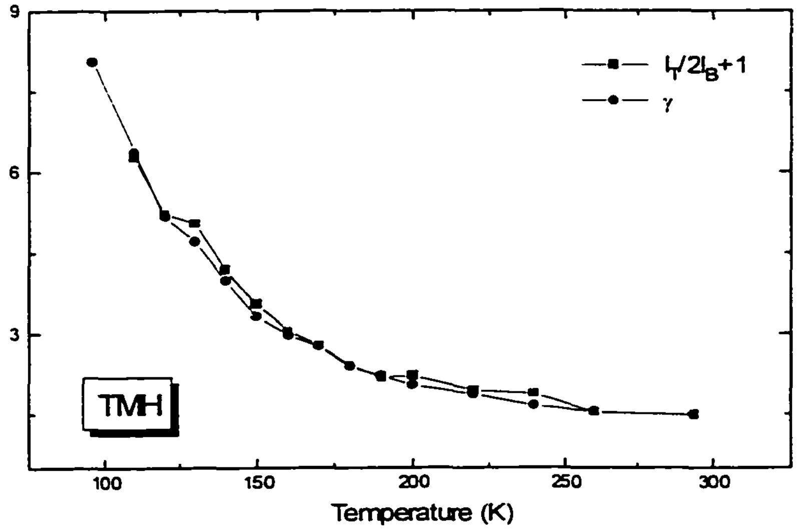

Figure 4-21 The Landau-Placzek ratio and the ratio of specific heats γ of TMH

Relaxation time

The relaxation times obtained from the Mountain theory fit and generalized hydrodynamic equation fit were also plotted as a function of temperature in Fig.4-22.

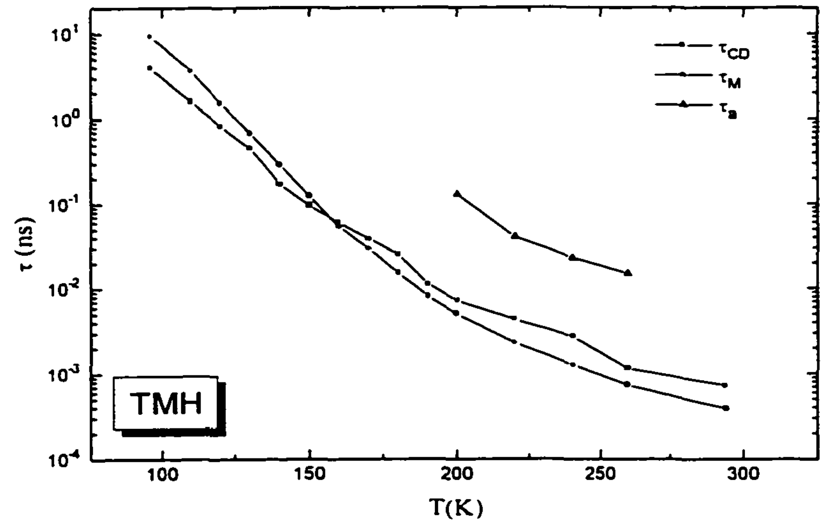

Figure 4-22 The relaxation times of TMH

Fig.4-22 also shows α-relaxation time calculated from α-peaks of the susceptibility spectra using the stretched exponential fit. The α-relaxation time was much longer than the relaxation time obtained from the Brillouin spectra while the Mountain fit and general hydrodynamic equation fit gave similar relaxation times. The same problem was found in several other materials, such as salol, PC, and OTP. This means that these two relaxation times represented two different relaxing processes.

A popular explanation [99-100] is that the relaxation processes in the VV spectra are due to the combination of structural relaxation and orientational relaxation while the α-relaxation process corresponds to the orientational relaxation. This explanation seems unlikely for TMH since the orientational relaxation is not important in the light scattering spectra of TMH.

High and low frequency limit sound velocities

To check the fitting results, we converted the ω_B, and ω_0 obtained from the fitting

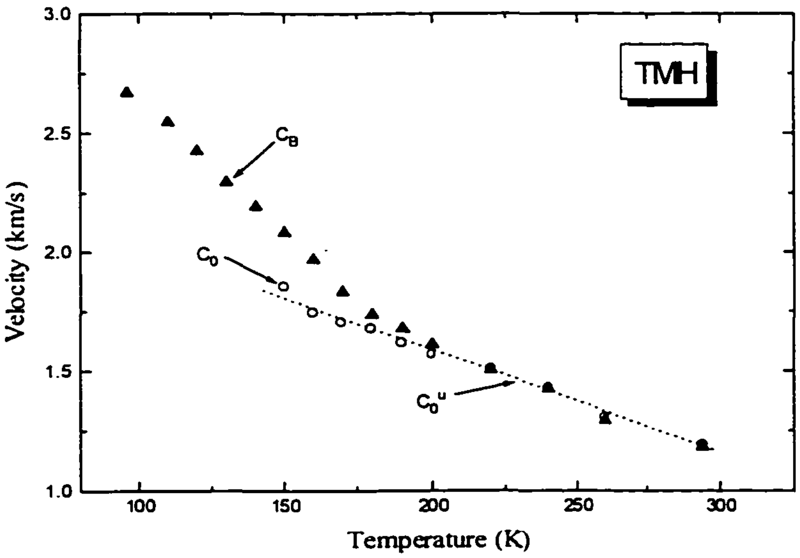

Figure 4-23 The acoustic sound velocity and low frequency limit of TMH

procedures to the acoustic sound velocity C_B and the low frequency limiting sound velocity C_0. These two velocities are plotted in Fig.4-23 with the ultrasonic velocity C_0^u (dashed line) obtained from the phase-sensitive technique. The low frequency limit sound velocity C_0 and the ultrasonic velocity C_0^u are very close.

Nonergodicity factor

The nonergodicity factor $f_0(T)$ of TMH was calculated from ω_0 and ω_∞ by Eq.[4.1] and plotted in Fig. 4-24. Note that there is a cusp in the $f_0(T)$ curve around 140K, which may indicate the crossover temperature T_C of the mode coupling theory. This crossover temperature is slightly lower than that obtained from the depolarized light scattering spectra. Unfortunately, there is no standard crossover temperature T_C for TMH.

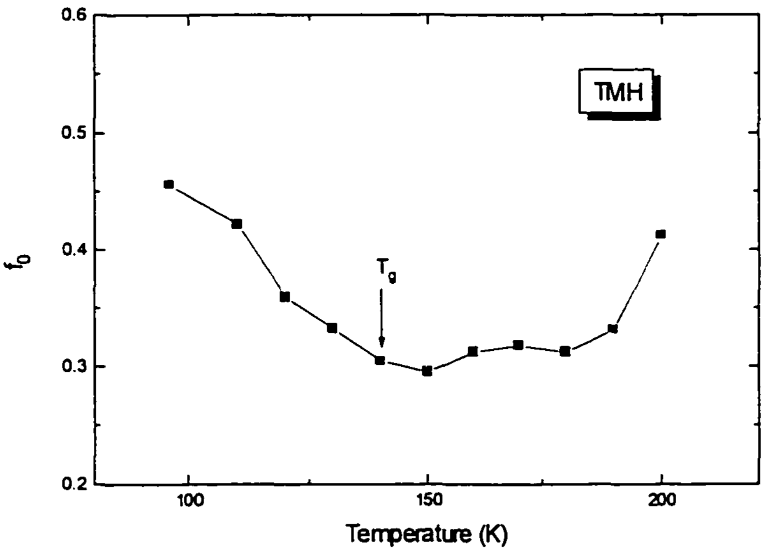

Fig. 4-24 The nonergodicity factor $f_0(T)$ of TMH

F. Depolarized Spectra of Salol

Orientational processes and shear waves

In the polarized spectrum, the central components arise from the mechanism of entropy and orientational fluctuations and the shifted Brillouin components are due to the propagation of longitudinal acoustic waves. On the other hand, the depolarized spectrum arises from the scattering of the shear acoustic waves and the fluctuations in the polarizability anisotropy associated with the molecular reorientational processes. At high temperature, the shear waves are overdamped in the normal viscous region and a central dip appears. As the liquid becomes supercooled, shear waves become underdamped and give rise to two symmetric transverse modes.

Salol

Since the central dip was not observed in the VH spectra of OTP and PC, another fragile (m = 73) glass-forming material [3], salol was studied. Salol has the melting temperature T_m = 315K, crossover temperature T_C = 256K, and the glass transition temperature T_g = 218K [90]. Many studies about the polarized (VV) and depolarized (VH) Brillouin spectra of salol were reported [101-102]. In those VH spectra, there is a clear central dip at high temperature and transverse modes at low temperature.

The salol was purchased from SIGMA in powder, then distilled 3 times in vacuum to obtain the dust free samples. The experimental setup was same as that for OTP and PC. The VV and VH spectra of salol were obtained in the temperature range 230K to 385K and at a scattering angle θ of 90^0 with FRS = 18.75GHz. Fig.4-25 shows the VV and VH spectra of salol at 370K. The VV spectrum consists of a Rayleigh component, a Mountain component, and two Brillouin components as discussed before. In the VH spectrum, an unshifted board Lorentzian shape (linewidth Γ) component combines a central dip. As the sample cooled, the linewidth of the board Lorentzian decreases, and the central dip becomes more difficult to observe. Several theories predict that the central dip only appears as $\Gamma << q^2\eta_0/\rho_0$, where q is the scattering wave vector, η_0 is the shear viscosity of the liquid in zero frequency limit, and ρ_0 is the density of the liquid.

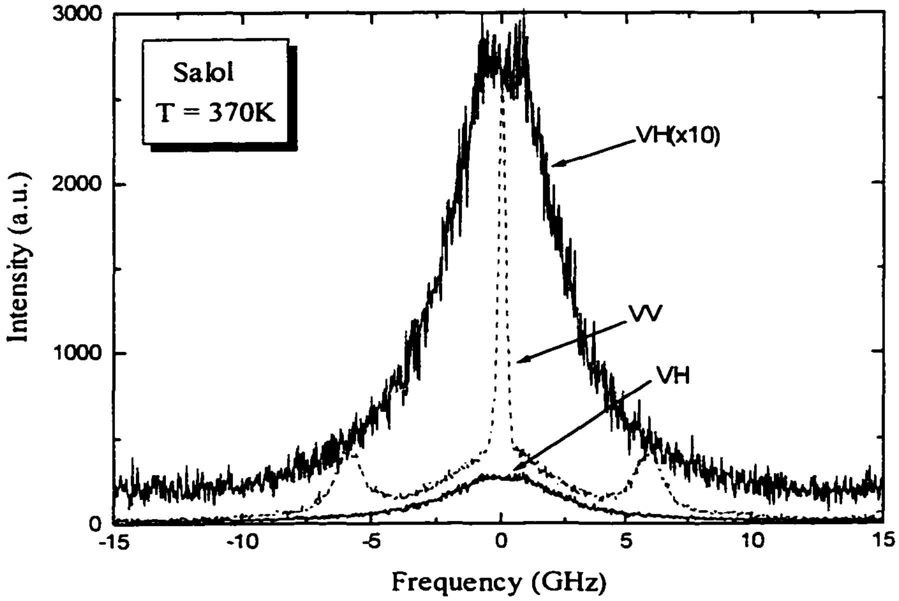

Figures 4-25 The VV and VH spectra of salol at T = 370K

Fig.4-26 shows the three typical VH spectra of salol at T = 240, 310, and 370 K. The VH spectra display totally different behaviors at different temperature regimes.

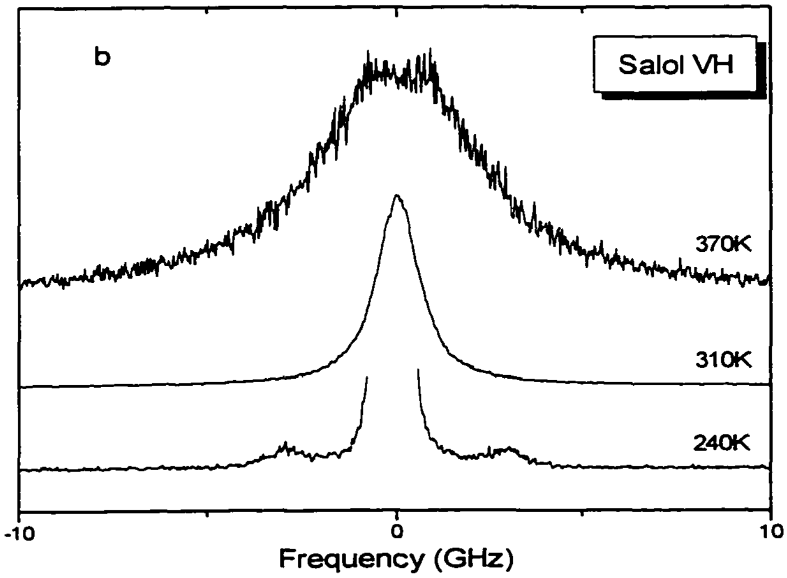

Figure 4-26 The three typical VH spectra of salol

High temperature ($\Gamma << q^2\eta_0/\rho_0$)

The VH spectra observed at high temperatures include an unshifted board Lorentzian with half-width Γ arising from the orientational fluctuations and a Lorentzian central dip with negative intensity due to the coupling of transverse velocity (shear waves) and orientational fluctuations. As the temperature decreases, the linewidth of board Lorentzian decreases and its intensity increases. In the contrast, the linewidth of central dip increases and its intensity decreases with decreasing temperature in the temperature range 385K to 350K. The central dip disappears below 350 K.

Intermediate temperature ($\Gamma \sim q^2\eta/\rho_0$)

In this temperature range, the viscosity of salol increases rapidly and the quantity $q^2\eta/\rho_0$ can compare with the linewidth of central component. Only an unshifted non-Lorentzian shape component due to orientational fluctuations, shear waves, and their couplings displays in the VH spectrum (the middle curve of Fig. 4-26).

Low temperature ($\Gamma << q^2\eta/\rho_0$)

Below 300 K, the value of $q^2\eta/\rho_0$ becomes much larger than the linewidth Γ. The supercooled salol presents solid-like behavior and the orientational fluctuations are frozen out. The VH spectrum contains a very strong central component and two symmetric transverse components with frequency shift $\omega_T = \pm v_T q$, where v_T is the velocity of the transverse acoustic waves (the bottom curve of Fig. 4-26). The frequency shift ω_T of the transverse mode moves to the high frequency as temperature decreases.

Detailed analysis of these depolarized spectra is currently in progress in our laboratory and will not be discussed further in this thesis.

PART II

DEPOLARIZED LIGHT SCATTERING SPECTROSCOPY

Chapter 5

Mode Coupling Theory

The viscoelastic behavior of supercooled liquids approaching the liquid-glass transition has been extensively investigated by various techniques for over 100 years. Many theories have been developed to explain this phenomenon. However, the origin of the strongly temperature-dependent slow relaxation behavior and its relation to the liquid-glass transition remained unclear until 1984.

In 1984, a new theoretical approach to supercooled liquid dynamics and the liquid-glass transition, known as the mode coupling theory (MCT), was developed in which the strong temperature dependence of structural relaxation results from retarded non-linear interactions among density fluctuations. MCT was first introduced by Leutheusser [14] and Bengtzelius, Gotze, and Sjolander [15] and primarily developed by Gotze and Sjogren [16, 18]. A complementary approach, which is based on fluctuating non-linear hydrodynamics, was introduced by Das and Mazenko [103].

MCT analyzes the dynamics of the density-fluctuation correlation function $\Phi_q(t)$ due to interaction with other modes and provides many detailed predictions for the liquid-glass transition dynamics. The central prediction in the idealized MCT is the existence of an ergodic (liquid-like) to nonergodic (solid-like) transition at a crossover temperature T_C, which should be the same for a given material from any appropriate experiment. This transition can be interpreted as the liquid-glass transition.

A. Equation of Motion

The normalized density-fluctuation correlation function

Fundamentally, MCT is a generalized kinetic Zwanzig-Mori equation approach to the density fluctuation dynamics in which a memory function representing retarded damping due to structural relaxation processes is expressed in terms of products of density correlation functions.

The quantity of primary concern in MCT is the normalized density-fluctuation correlation function given by

$$\Phi_q(t) = <\delta\rho_q(t)\delta\rho_q^*(0)> / S_q , \qquad [5.1]$$

where $\delta\rho_q$ is the qth Fourier component of the density fluctuation $\delta\rho$, and $S_q = <\delta\rho_q(0)\delta\rho_q^*(0)>$ is the static structure factor. The Laplace transform $\Phi_q(z)$ of the density-fluctuation correlation function $\Phi_q(t)$ is represented as a Zwanzig-Mori fraction in terms of a generalized damping function $M_q(z)$:

$$\Phi_q(z) = -1/\{z- \Omega_q^2/[z+M_q(z)]\} , \qquad [5.2]$$

where $\Omega_q^2 = v^2q^2/S_q$ is the microscopic frequency.

The generalized oscillator equation

There are two versions of MCT: the original idealized MCT and the extended MCT. The idealized MCT only considers cage effects while the extended MCT includes additional hopping effects. In this thesis, we focus on the idealized MCT but include a brief introduction to the extended MCT. In the idealized MCT, $M_q(z)$ is expressed in the form of a fast damping (or regular damping) term γ_q and a slow damping term (the kernel) which is frequency dependent

$$M_q(z) = \Omega_q^2[i\gamma_q+m_q(z)] , \qquad [5.3]$$

where the slow damping term $m_q(z)$ is the Laplace transform of the memory function $m_q(t)$. The normalized density-fluctuation correlation function $\Phi_q(t)$ obeys the generalized oscillator equation:

$$\ddot{\Phi}_q(t) + \gamma_q\Omega_q^2\dot{\Phi}_q(t) + \Omega_q^2\Phi_q(t) + \Omega_q^2\int_0^t dt' m_q(t-t')\dot{\Phi}_q(t') = 0 \ . \qquad [5.4]$$

It can be proved that Eq. [5.2] is equivalent to Eq. [5.4] by Laplace transforming Eq.[5.4] with initial conditions of $\dot{\Phi}_q(t=0) = 0$ and $\Phi_q(t=0) = 1$. The Laplace transform conventionally used for the MCT is different from the conventional (-st) Laplace transform. The definition of a Laplace transform f(z) of a function f(t) in the MCT is given by

$$\Lambda[f(t)] = f(z) = i\int_0^\infty f(t)e^{izt}dt \ . \qquad [5.5]$$

Memory function

Note that Eq. [5.4] can be reduced to Eq. [3.37] if q goes to zero and the memory function $m_q(t)$ is assumed to have a specific form, e.g. the KWW function. In the idealized MCT, which does not include activated hopping processes, the memory function $m_q(t)$ is expressed as

$$m_q(t) = \sum_{q_1} V^{(1)}(q,q_1)\Phi_{q_1}(t) + \sum_{q_1q_2} V^{(2)}(q,q_1,q_2)\Phi_{q_1}(t)\Phi_{q_2}(t) + \cdots , \qquad [5.6]$$

where $V^{(i)}$ are the coupling constants (vertices) which can be expressed in terms of the static structure factors S_q [15]. In principle, S_q is determined by the intermolecular potentials of the liquid. A complete self-consistent solution of Equations [5.4] and [5.6] can be obtained by restricting both the range of q values and the number of coupling constants. The Fourier transform of the result $\Phi(t)$ gives the dynamic structural factor $S_q(\omega)$ and the susceptibility spectrum $\chi_q''(\omega) = \omega S_q(\omega)$.

Within the ideal glass-transition approximation, the self-consistent solutions of Eqs.[5.4] and [5.6] show that when a system is cooled in the liquid phase, the vertices increase and there exists a crossover temperature T_C in which a critical slowing down of $\Phi_q(t)$ occurs that leads to a transition from ergodic liquid dynamics for $T > T_C$ to nonergodic glass dynamics for $T < T_C$ [14-15].

Cage effects

The idealized MCT primarily deals with the solutions of Eqs. [5.4] and [5.6] for small separation parameter $\sigma \propto (T_C - T)/T_C$ which quantifies the cage effect. For $T < T_C$, the particles of the liquid are permanently trapped in cages, which are formed by their neighbors, without any chance to jump out so that density fluctuations no longer decay totally, but only to a nonzero value limit. When $T > T_C$, the cages can only localize the captured particles for a finite time before they find paths to escape, and the density fluctuations then decay to zero. α-relaxation corresponds to this long-time decay due to the cage effect while β-relaxation, which occurs on a shorter time scale, is attributed to molecular motions within the transient cages [104].

Hopping effects

Das and Mazenko [103] suggested that the glass transition singularity at T_C is smeared out due to terms in $m_q(t)$ originating from a coupling to the current density. The same conclusion was found later by Gotze and Sjogren [18]. The latter authors identified the hopping processes, in which a tagged particle jumps over saddle points in a potential landscape, to be responsible for restoring ergodicity. In the microscopic theory, the hopping event appears because phonons kick the particles over barriers. The hopping effects depend crucially on structural details on length scales corresponding to the inter-particle spacing [16]. In the idealized MCT version, the hopping effect is ignored.

B. Schematic idealized MCT

In the idealized MCT, the major term in the memory function $m_q(t)$ is the two-mode coupling, $\Sigma_{q1,q2}$ $V^{(2)}(q, q_1, q_2)\Phi_{q1}(t)$)$\Phi_{q2}(t)$ with $q = q_1+q_2$. The largest contribution comes from q-values close to the peak of the static structure factor S ($q=q_0$), where q_0^{-1} corresponds approximately to the separation between nearest neighbors.

The F_2 model

The simplest schematic model is the F_2 model in the idealized MCT in which one restricts q to a thin spherical shell with $q = q_0$. The memory function is written as $m_q(t) = V^{(2)}\,\Phi^2(t)$ and Eq.[5.4] reduces to a single schematic equation

$$\ddot{\Phi}(t) + \gamma\Omega^2\dot{\Phi}(t) + \Omega^2\Phi(t) + \Omega^2\int_0^t dt'\, V^{(2)}\Phi^2(t')\dot{\Phi}(t') = 0 \ . \qquad [5.7]$$

Leutheusser [14] and Bengtzelius et al. [15] solved Eq.[5.7] numerically and showed the evolution of the two-peak structure of the susceptibility spectrum. They carried out expansions around the transition point and gave a set of self-consistent solutions of the F_2 model. They found that the system transforms from an ergodic liquid state for $T>T_C$ to a nonergodic glass state for $T<T_C$ as the coupling constant $V^{(2)}$

increases to a critical value $V^{(2)} = 4$. At $T = T_C$, the correlation function Φ asymptotic value $f_q = \lim_{t\to\infty} \Phi(t)$ increases abruptly from zero to a nonzero limit called the nonergodicity parameter, or Debye-Waller factor. The nonergodicity parameter is chosen as an order parameter which vanishes in the ergodic phase (liquid state) and is positive in the nonergodic phase (glass state). Although the results obtained with this simple model were preliminary and could not provide detailed quantitative explanations of experimental results, they illustrate clearly the basic concepts of MCT.

Stretched exponential decay

For $T>T_C$, the F_2 model predicts an exponential long-time decay but not the stretched exponential decay of the final α-relaxation which is observed in many experiments. For the F_{12} model ($V^{(1)} \neq 0$ and $V^{(2)} \neq 0$) or the F_{13} model ($V^{(1)} \neq 0$ and $V^{(3)} \neq 0$), the α-relaxation is well described by the Kohlrausch-Williams-Watts (KWW) equation, in which the stretching exponent β is between 0 and 1.

The F_{12} model

The next simplest schematic model, the F_{12} model for which the memory function is read

$$m(t) = V^{(1)}\Phi(t)+V^{(2)}\Phi^2(t)\,, \qquad [5.8]$$

does produce the stretching exponential decay and has been used frequently in the subsequent studies of schematic models.

The equation of motion for the F_{12} model is given by

$$\ddot{\Phi}(t) + \gamma\Omega^2\dot{\Phi}(t) + \Omega^2\Phi(t) + \Omega^2\int_0^t dt'[V^{(1)}\dot{\Phi}(t') + V^{(2)}\Phi^2(t')\dot{\Phi}(t')] = 0\,. \qquad [5.9]$$

In Eq. [5.9], there are only two coupling parameters and no input information is used, which is directly related to structural relaxation features. Fig. 5-1a shows the numerical solutions of the F_{12} model for the correlation function Φ(t) at three temperatures and Fig. 5-1b shows the corresponding susceptibility spectra χ"(ω). These results predict several crucial properties independent on the details of the microscopic interactions.

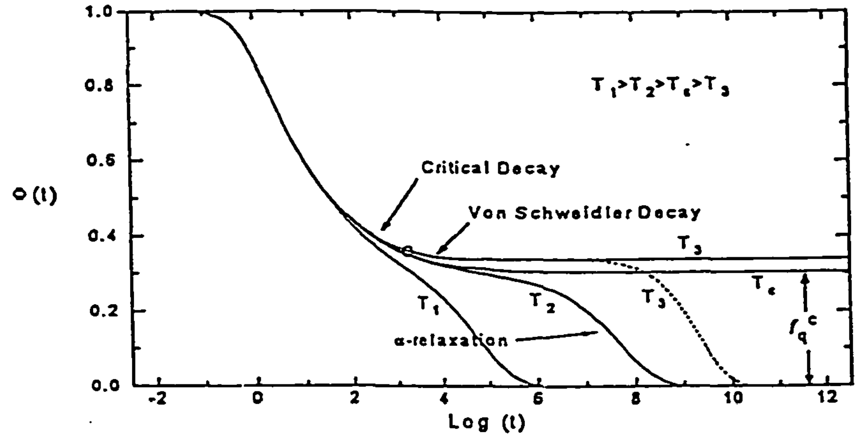

Figure 5-1a Numerical solutions of the correlation functions Φ(t) of the F_{12} model. The dashed line is the result of the extended MCT [105].

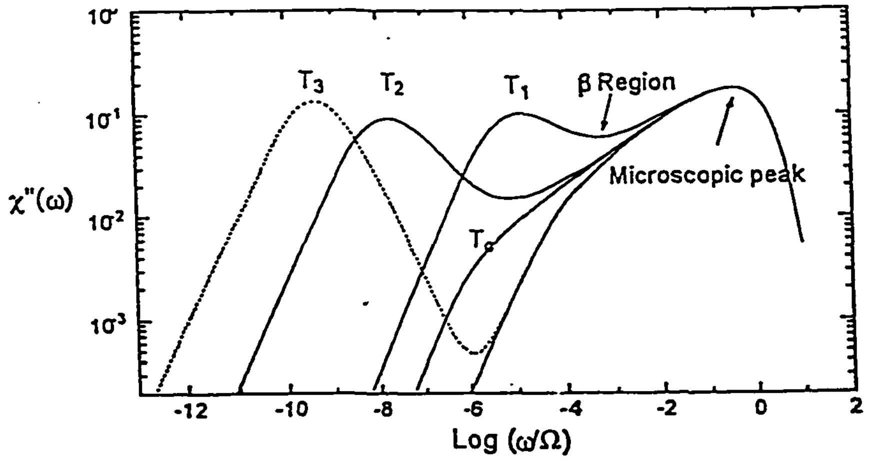

Figure 5-1b The corresponding susceptibility spectra χ"(ω) [105]

Two-step relaxation processes

For $T>T_C$, the system is in the liquid state (curve T_1 or T_2 in Fig. 5-1), and the correlation function $\Phi(t)$ exhibits a two-step relaxation process. First, a fast decay (the critical decay) towards a plateau value f_q (the non-ergodicity parameter) followed by a slow decay (the von Schweidler decay); then the α-relaxation process takes over from the von Schweidler decay and describes the final decay towards the equilibrium value zero. The α-relaxation process does not describe the complete structural relaxation but rather the final part of the decay from the plateau. The critical and von Schweidler processes, for which $\Phi(t)$ is close to the plateau value, are togather referred to as the β-relaxation region.

In the corresponding susceptibility spectrum $\chi''(\omega)$ there are three region: a high frequency microscopic peak which is essentially temperature independent corresponding to microscopic phonon excitations, also called the Boson peak; a low frequency primary α-relaxation peak due to the cage effects which moves towards lower frequency with decreasing temperature; between these two peaks is the intermediate β-relaxation region surrounding a susceptibility minimum, due to molecular motions within the transient cages.

At $T=T_C$, the correlation function $\Phi(t\rightarrow\infty)$ jumps from zero to the non-ergodicity parameter f_q and no α-relaxation process exists. For $T<T_C$, the system enters the glass state (curve T_3), and the correlation function $\Phi(t)$ reaches a plateau, via the critical decay (The dashed line section of T_3 is the results of the extended MCT which includes the hopping processes as discussed below in section D). The value of the plateau increases

with decreasing temperature. In the susceptibility spectrum, the α peak disappears, and the β-relaxation process changes from concave upwards to downwards, the so called 'knee'.

The nonergodicity parameter $f_q(T)$

The temperature dependence of the nonergodicity parameter $f_q(T)$ obeys

$$f_q(T) = \begin{matrix} f_q^c + h_q\sqrt{\sigma} + O(\sigma^2), & T < T_C \\ O(\sigma^2), & T > T_C \end{matrix} \qquad [5.10]$$

where f_q^c and h_q are two temperature-independent constants, $\sigma \propto (T_C - T)/T_C$ is the separation parameter. Fig. 5-2 shows the theoretical curve of the nonergodicity parameter $f_q(T)$ as a function of temperature.

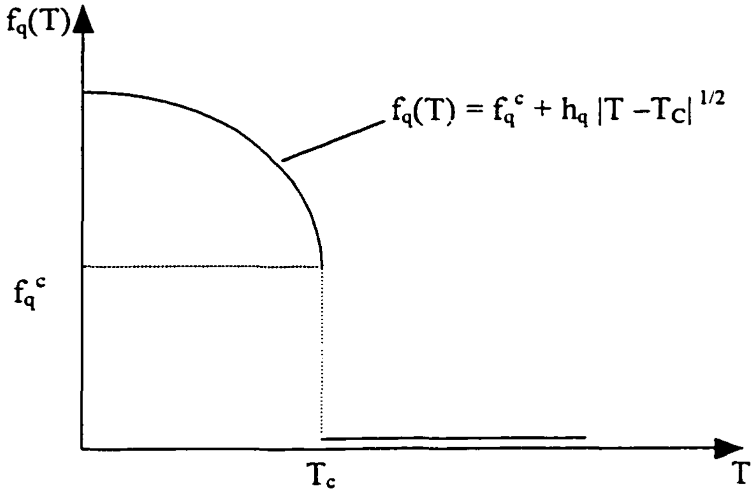

Figure.5-2. Schematic diagram of the nonergodicity parameter $f_q(T)$

C. Predictions of the idealized MCT

Numerical solution

Numerical solution of the Eq.[5.4] can be obtained if the intermolecular potential is tractable, such as the hard sphere or Lennard-Jones potential. However, asymptotic solutions can give some important asymptotic behaviors of the correlation function $\Phi(t)$ and show that the asymptotic forms of $\Phi(t)$ are independent of the detailed structure of the vertices $V^{(i)}$ for temperatures close to the crossover temperature T_C.

Two scaling laws

For the idealized MCT, there are two frequency scales ruling the slowing down of relaxation processes when the temperature is near T_C [16,18]. One scaling frequency

$$\omega'_\sigma \propto \Omega|\sigma|^\gamma \qquad [5.11a]$$

governs the primary relaxation (α-relaxation) in the liquid state, while the other scaling frequency

$$\omega_\sigma \propto \Omega|\sigma|^{1/2a} \qquad [5.11b]$$

governs the secondary relaxation (β-relaxation) in both the liquid and glass states. In Eq. [5.11], $\gamma = 1/2a + 1/2b$ and a ($0 < a < 1/2$) and b ($0 < b < 1$) are the critical exponents of the theory, determined by a single exponent parameter λ via the Γ function equation,

$$\frac{\Gamma^2(1-a)}{\Gamma(1-2a)} = \lambda = \frac{\Gamma^2(1+b)}{\Gamma(1+2b)}. \qquad [5.12]$$

In principle, the exponent parameter λ can be evaluated if the vertices $V^{(i)}$ are known. λ is usually treated as a material-dependent fitting parameter in practical data analysis due to the complexity of the structure of real materials.

β-relaxation scaling

The β-relaxation denotes the relaxation dynamics in the intermediate frequency range between the microscopic frequency and the primary α-relaxation range. The idealized MCT makes detailed predictions for the frequency and temperature dependence of the density-fluctuation correlation function $\Phi_q(t)$. Within the β-relaxation regime, the idealized MCT found that the correlation function $\Phi_q(t)$ obeys a factorization rule:

$$\Phi_q(t) = f_q^c + h_q G(t), \qquad [5.13]$$

where f_q^c is the Debye-Waller (nonergodicity) factor at T_C, h_q is a critical amplitude, and the q-independent G(t) is the β correlator. Similar relations hold for the correlation functions of any variables which have nonzero projection onto the density fluctuations.

The β correlator G(t)

The β correlator G(t) is a universal function for all variables and wave vectors and obeys the equation of motion

$$\sigma + \lambda G^2(t) - \frac{d}{dt}\int_0^t G(t-t')G(t')dt' = 0. \qquad [5.14]$$

For the separation parameter $\sigma \ll 1$, the β correlator G(t) satisfies the conventional scaling law

$$G(t) = |\sigma|^{1/2} g_\pm(t/t_\sigma), \qquad [5.16]$$

where $t_\sigma = 1/\omega_\sigma = t_0|\sigma|^{1/2a}$ is the scaling time, t_0 is a microscopic matching time, and the master functions $g_\pm(t)$, ± signs refer to $\sigma > 0$ (glass state) and $\sigma < 0$ (liquid state), are independent of the separation parameter.

The master functions

The asymptotic forms of the master functions $g_\pm(t)$ follow the power laws

$$g_{\pm}(t) = t^{-a}, \qquad (t_0 << t << t_\sigma) \qquad [5.17a]$$

$$g_{-}(t) = -Bt^{b}, \qquad (t >> t_\sigma) \qquad [5.17b]$$

$$g_{+}(t) = (1-\lambda)^{1/2} \qquad (t >> t_\sigma)\,. \qquad [5.17c]$$

Then, the correlation function $\Phi_q(t)$ for the β-relaxation region can be constructed from these asymptotic expansions of the master functions $g_{\pm}(t)$. For temperature T above but near T_C, the form of $\Phi_q(t)$ in the β-relaxation region exhibits a power-law decay (the critical decay) towards to a plateau f_q^c:

$$\Phi_q(t) = f_q^c + h_q(t/t_\sigma)^{-a}, \qquad [5.18]$$

followed by a second power-law decay (the von Schweidler decay):

$$\Phi_q(t) = f_q^c - B_q(t/t_\sigma)^{b}\ , \qquad [5.19]$$

which is the beginning of the α-relaxation process. For $T < T_C$, the correlation function $\Phi(t)$ follows the same power-law decay, Eq.[5.18], towards a plateau f_q given by Eqs.[5.16] and [5.17]. Both α-relaxation and von Schweidler decay arrest.

Power laws

Similarly, these two power-law regions of $\Phi_q(t)$ cause of two power-law regions in $S_q(\omega)$: $S_q(\omega) \propto \omega^{-(1+b)}$ in the low frequency region and $S_q(\omega) \propto \omega^{-(1-a)}$ in the high frequency region.

Therefore, the susceptibility spectrum $\chi''(\omega) = \omega S_q(\omega)/S_q$ is given by:

$$\chi''(\omega) = h_q\, |\sigma|^{1/2}\, \hat{\chi}''_{\pm}(\omega)\ . \qquad [5.20]$$

Eq.[5.20] predicts that for either T > T_C or T < T_C, all susceptibility spectra should scale onto a single master curve ($\hat{\chi}_-$ or $\hat{\chi}_+$), with the scaling frequency $\omega_\sigma \rightarrow 0$ as $T \rightarrow T_C$ from either above or below.

For T > T_C, $\chi''(\omega)$ exhibits a minimum between these two regions which asymptotically approaches

$$\hat{\chi}''_-(\omega) \propto \omega^{-b} \qquad (\omega \ll \omega_\sigma) \qquad [5.21a]$$

and

$$\hat{\chi}''_-(\omega) \propto \omega^{a} \qquad (\omega \gg \omega_\sigma). \qquad [5.21b]$$

For T < T_C, there is a 'knee' which locates a crossover at ω_σ from

$$\hat{\chi}''_+(\omega) \propto \omega \qquad (\omega \ll \omega_\sigma) \qquad [5.22a]$$

to

$$\hat{\chi}''_+(\omega) \propto \omega^{a} \qquad (\omega \gg \omega_\sigma). \qquad [5.22b]$$

The interpolation function

The two susceptibility master functions $\hat{\chi}''_+(\omega)$ for the glass state and $\hat{\chi}''_-(\omega)$ for the liquid state can be calculated numerically once λ is specified [106]. Eq.[5.21] yields an approximate interpolation formula for the $\chi''(\omega)$ in the frequency regime around the susceptibility minimum:

$$\chi''(\omega) = \frac{\chi''_{min}\left[b(\omega/\omega_{min})^{a} + a(\omega_{min}/\omega)^{b}\right]}{a+b}, \qquad [5.23]$$

where χ''_{min} and ω_{min} are the susceptibility and frequency minimums. Comparing Eqs.

[5.20] and [5.23], $\chi''_{\min}$ and $\omega_{\min}$ are described by the separation parameter σ:

$$\chi''_{\min} \propto |\sigma|^{1/2}, \qquad [5.24a]$$

$$\omega_{\min} \propto |\sigma|^{1/2a}. \qquad [5.24b]$$

For $T < T_C$, an explicit expression for the susceptibility can be derived from Eqs. [5.22a] and [5.22b]. The α-peak disappears and the β-relaxation process changes from concave upwards to downwards.

α-relaxation scaling

The long time part of the correlation function $\Phi_q(t)$ is the α-relaxation which corresponds to the low frequency peak in the susceptibility. Unlike the β-relaxation that only depends on the single exponent parameter λ, the α-relaxation is much more complicated. It depends on the microscopic structural details contained in the vertices $V^{(i)}$.

For $T > T_C$, the α-relaxation is governed by the scaling frequency ω_α. The form of $\Phi_q(t)$ obeys the time-temperature superposition principle[16]

$$\Phi_q(t) = F_q(t\omega_\alpha), \qquad [5.25]$$

where the temperature dependence only enters via the scaling frequency ω_α. The idealized MCT does not give a general form for this process, but Gotze and Sjogren [16] have shown that F_q can be closely approximated by the Kohlrausch-Williams-Watts or stretched-exponential function in the α-relaxation regime. Therefore, the correlation function $\Phi_q(t)$ is given by

$$\Phi_q(t) = F_q(t\omega_\alpha) \propto \exp[-(t/\tau_\alpha)^{\beta_K}] \,, \qquad [5.26]$$

where $\tau_\alpha = 1/\omega_\alpha$ is the α-relaxation time and the stretched exponent β_K is temperature independent.

The susceptibility spectrum $\chi''(\omega)$ follows a scaling relation

$$\chi''(\omega) = \hat{\chi}''(\omega/\omega_\alpha) \,. \qquad [5.27]$$

It can be found from Eq.[5.27] that the position of the α-relaxation maxima on the susceptibility spectra are controlled by the scaling frequency ω_α:

$$\omega_{max} \propto \omega_\alpha \propto |\sigma|^\gamma \,, \qquad [5.28a]$$

or

$$\tau_\alpha = 1/\omega_\alpha \propto |\sigma|^{-\gamma} \,. \qquad [5.28b]$$

So, T_C can be determined by fitting $\tau_\alpha(T)$ with a linear function.

D. Introduction to the extended MCT

It is important to note that the prediction of the idealized version MCT of an ergodic to a nonergodic state transition at T_C is incorrect, although this theory correctly describes many aspects of supercooled liquid dynamics. Activated transport processes, which are not included in this version of the theory, provide additional relaxation mechanism for density fluctuations at temperatures below T_C, restoring both ergodicity and α-relaxation.

Hopping parameter $\delta_q(\omega)$

The extended version MCT [106] which includes ergodicity-restoring activated hopping processes was developed by Gotze and Sjogren. In the extended MCT, a current term $\delta_q(t)$ is added in the kernel M(t-t') in Eq.[5.3] to represent this hopping effect:

$$M_q(\omega) = \frac{i\gamma_q + m_q(\omega)}{1 - \delta_q(\omega)\Omega_q^2[i\gamma_q + m_q(\omega)]}\ , \qquad [5.29]$$

where $\delta_q(\omega)$ is the Fourier transform of

$$\delta_q(t) = \sum_{q1,q2} V'(q_1, q_2, q)\dot{\Phi}_{q1}(t)\Phi_{q2}(t) + \cdots\ . \qquad [5.30]$$

Eqs.[5.29] and [5.30] represent, to leading order, the coupling of density fluctuations to activated transport processes through the temperature-dependent hopping kernel δ_q taken as the $\omega \to 0$ limit of $\delta_q(\omega)$.

β-correlator G(t)

The correlation function $\Phi_q(t)$ in the β-relaxation region still obeys the factorization property of [5.13] in the extended MCT. However, the equation of motion for the β-correlator is now given by

$$\sigma - \delta t + \lambda G^2(t) - \frac{d}{dt}\int_0^t G(t-t')G(t')dt' = 0\ . \qquad [5.31]$$

In Eq.[5.31], σ is the previously introduced separation parameter which quantifies the cage effect. δ, designated as the hopping parameter, is a smoothly-varying quantity determined by the kernels δ_q (t). In the β regime the dependence of the solution on the many vertices is reduced to the dependence on the exponent parameter λ and the two temperature-dependent quantities σ and δ. These quantities play the role of the relevant control parameters, governing the physical behaviors near the glass-transition singularity for intermediate times or frequencies (β-relaxation regime). Once λ has been specified, the β-correlator G(t) and the corresponding susceptibility function χ"(ω) are fixed by the separation parameter σ and the hopping parameter δ.

In extended MCT, interaction effects among density fluctuations dominate relaxation for $T > T_C$ (normal and moderately supercooled state) and hopping events are elementary steps leading to complex relaxation for $T < T_C$ (strongly supercooled state). Therefore, the sudden structural arrest at T_C is replaced by a gradual crossover from liquid dynamics to glassy dynamics; the α-peak and susceptibility minimum both exist at all temperature. The extended version MCT can be reduced to the idealized version in the limit of $\delta \to 0$. For more details, see reference [106].

Chapter 6

Tests of the Mode Coupling Theory: TMH

The mode coupling theory (MCT) of the liquid-glass transition, based on the concept of non-linear interaction between density fluctuation modes, provides detailed predictions for the dynamics of supercooled liquids. Experimental tests of the MCT predictions for the α and β-relaxation dynamics have been carried out by neutron and light scattering spectroscopies for some fragile glass-forming materials. In our laboratory, the depolarized near back-scattering spectra of the fragile glass-forming liquids CKN, salol, PC, OTP, and the intermediate glass-forming material glycerol were measured in a wide frequency range and analyzed by the idealized and extended MCT. Good fits to experimental data and some useful information were obtained. Following the methods of these previous studies, the wide-frequency-range depolarized back-scattering spectra of TMH were collected and the corresponding susceptibility spectra were analyzed by the idealized MCT. As discussed in Chapter 4, TMH was selected because its low depolarization ratio indicates that orientational dynamics can be ignored, making direct comparison with MCT more straight-forward.

A. Experimental Apparatus

To obtain a wide-frequency-range spectrum, two primary experimental apparatuses were employed: a Sandercock 6-pass Tandem Fabry-Perot interferometer which has been described in Chapter 2, and a conventional tandem Raman spectrometer (Spex 1401) which will be discussed below. Light-scattering measurements were performed in the depolarized near back-scattering geometry to eliminate the influence of Brillouin scattering from the longitudinal and transverse acoustic modes which are both forbidden in this geometry. The depolarized back-scattering geometry also provides a high signal-to-noise ratio due to the large effective length of the scattering volume.

Fig. 6-1 shows a schematic diagram of the Raman scattering apparatus. The excitation light (Coherent, Innona 300C, Argon laser; λ = 488 nm) is focused on the sample by lens L1. The excitation electric field was vertically polarized relative to the scattering plane. Scattered light was collected at a near back-scattering angle of 173^0 by lens L2 and focused on the spatial filter SF, which determined the scattering volume. The polarizer P selected the polarization component of scattered light. The polarizer P was set in the horizontal direction in depolarized back-scattering measurements. The lens L3 collimated the beam. A scrambler S was used to produce unpolarized light in order to average the polarization efficiency of the monochromater. The lens L4 matched the entrance solid angle and focused the scattered beam on the entrance slit. The entrance,

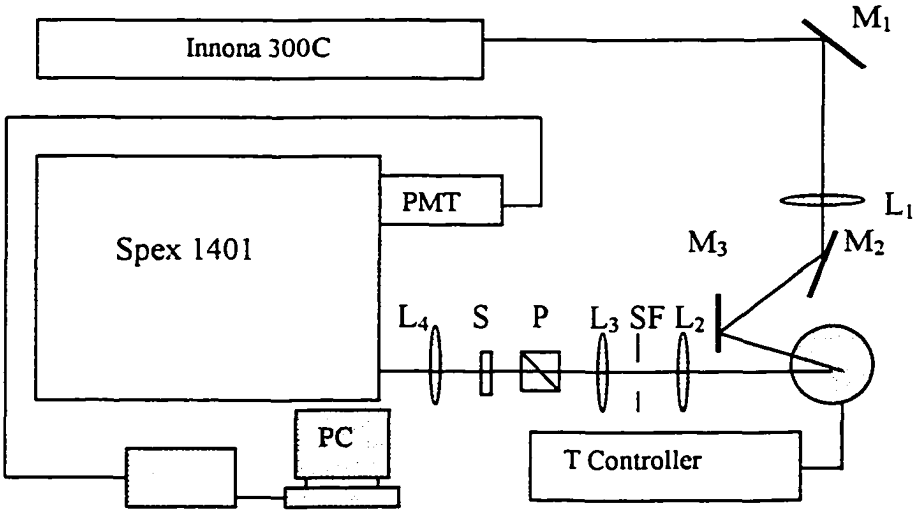

Figure 6-1 Schematic diagram of Raman apparatus at near back scattering geometry

middle, and exit slits of the spectrometer were usually set to 100, 200, and 100μm respectively. With these slit-widths, the spectral resolution is about 1 cm^{-1}. Like the Brillouin scattering apparatus, the signal collected by PMT is fed to an EG&G multi-channel scale acquisition adapter card in a PC computer after passing a discriminator.

B. Data Processing

Composite spectrum

Fig. 6-2a shows a typical depolarized back-scattering spectrum of TMH at T = 220 K with FRS = 18.75 GHz. To obtain a large frequency range spectrum, four TFPI spectra with different free spectral ranges (FSR = 7.5, 18.75, 75, 300 GHz) for the low frequency region (0.5 ~ 200 GHz) and a Raman spectrum for the high frequency region (200 ~ 4000 GHz) were measured in the same scattering geometry. Fig. 6-2b shows a log–log plot of the positive (Stokes) sides of the four TFPI spectra and the Raman spectrum of TMH at T = 220 K.

Using their overlapping ranges, the five spectra were spliced together smoothly by adjusting the intensity amplitudes to construct a wide-frequency-range composite intensity spectrum [97], shown in Fig. 6-2c. This intensity spectrum covers a frequency range of ~ 0.4 GHz to 4 THz. This overlapping method was primary developed in our laboratory. During the data processing, the Raman spectrum, which was carefully controlled to avoid drifting of the instrumental response, was used as a standard spectrum to normalize the intensity of the TFPI spectra. Because of the weak depolarized scattering intensity of TMH, the TFPI spectra were obtained by averaging several measurements in the same experimental environment to increase the signal-to-noise ratio.

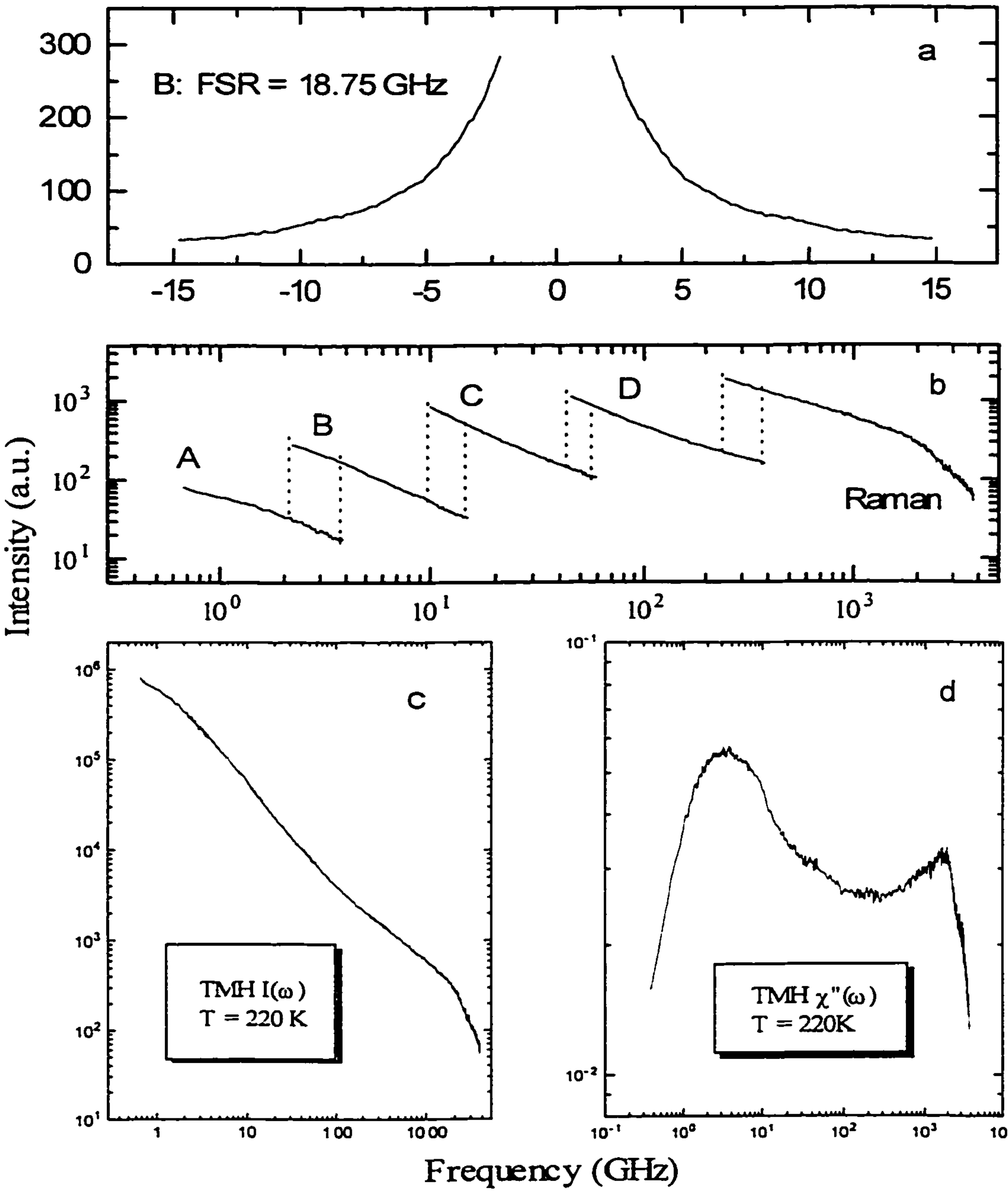

Figure 6-2 (a)The depolarized back-scattering spectrum of TMH at 220K with FSR = 18.75 GHz. (b) Four TFPI spectra with different FSRs and a Raman spectrum. (c) The combined intensity spectrum. (d) The corresponding susceptibility spectrum of TMH at 220K

The same procedure was applied for the spectra at different temperatures. Fig. 6-3 shows the complete set of the intensity spectra of TMH. The intensity spectra span a frequency range of over four decades and display a continuous evolution of the dynamics with decreasing temperature which was identified in other experimental studies and predicted by MCT. Around 200 K, the spectra exhibit two distinct power law regions implying a two-step relaxation process as predicted by MCT.

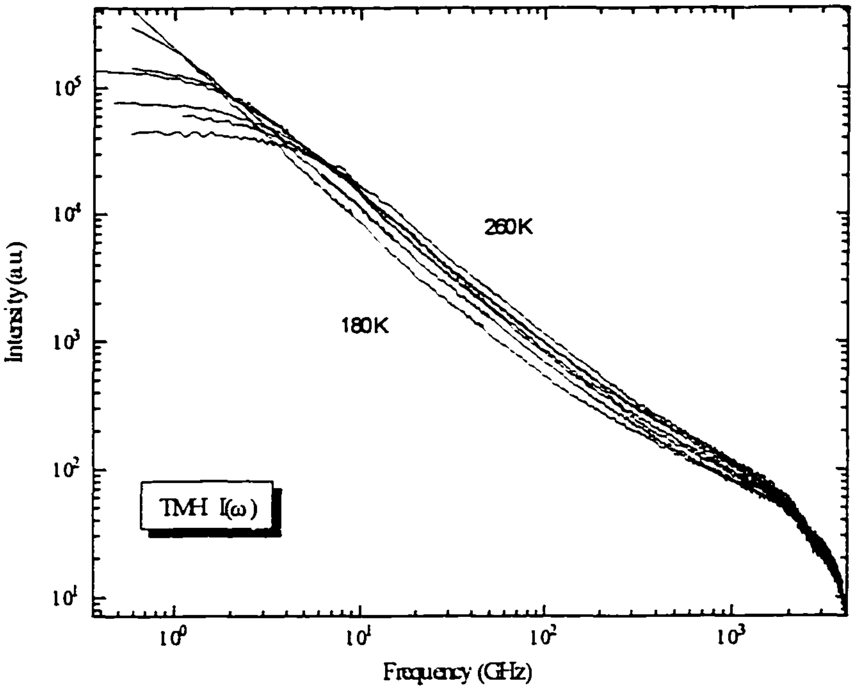

Figure. 6-3 Composite intensity spectra of TMH. The temperature are (top to bottom) 260, 240, 230, 220, 210, 200, and 180 K.

Susceptibility spectrum

Following the fluctuation-dissipation theorem [26], the composite intensity spectrum of Fig. 6-2c was converted to the susceptibility spectrum $\chi''(\omega)$ through the relation

$$\chi''(\omega) = \frac{I(\omega)}{n(\omega,T)+1}, \qquad [6.1]$$

where $n(\omega,T)$ is the Bose factor. The corresponding susceptibility spectrum $\chi''(\omega)$ is shown in Fig. 6-2d. The low-frequency broad peak is the α-relaxation peak, which is associated with the primary structural relaxation process. The high-frequency peak is the microscopic excitation band (or Boson peak). The range around the minimum between the α-relaxation peak and microscopic excitation band is identified as the MCT intermediate β-relaxation region.

Fig. 6-4 shows a set of susceptibility spectra of TMH obtained from the intensity spectra (Fig. 6-3). At high temperature, the α-relaxation and β-relaxation merge with the microscopic excitation band (The spectra shown in Fig. 6-1 do not extend to high enough temperature to exhibit this merging clearly). The α-relaxation peak moves towards low frequency with decreasing temperature and disappears from the experimental window at ~ 200K. In addition, the β-relaxation range gradually develops in the intermediate-frequency and the susceptibility minimum moves towards lower frequency with decreasing temperature. The microscopic excitation band shows a nearly temperature-independent characteristic.

C. Data Analysis and results

A quantitative test of the MCT can be carried out by directly comparing the scaling-law predictions reviewed in the preceding chapter with the experimental susceptibility data.

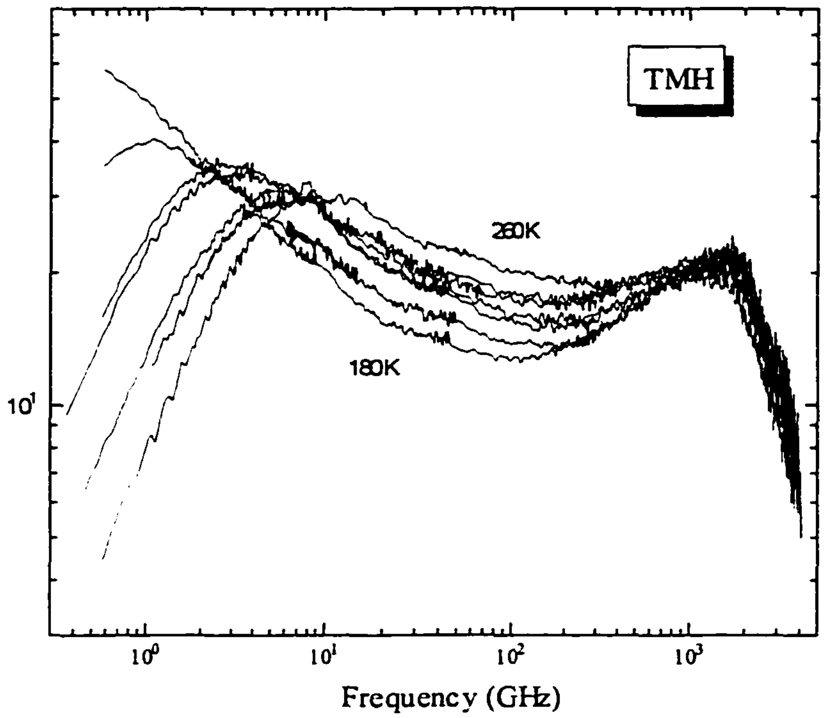

Figure 6-4 Susceptibility spectra corresponding to the data of Fig. 6-3 obtained with Eq. [6.1].

β-relaxation region

The susceptibility spectra of TMH from 260 to 180 K were analyzed directly using the interpolation function of Eq. [5.23]. First, χ''_{min}, ω_{min}, and the critical exponent a were treated as adjustable parameters for each spectrum and the exponent b was determined by the constraint of Eq. [5.12]. Then, a single optimum value of the critical exponent a for all the spectra was found by a global fit. The best global fit for all those curves was obtained with

$$a = 0.293$$

which determined the values of b and λ for TMH [107]:

$$b = 0.519, \qquad \lambda = 0.77.$$

The best fit values of χ''_{min} and ω_{min} obtained from the global fit for each temperature are listed in Table 6-1. Fig. 6-5 shows the best global fitting curves and the experimental susceptibility spectra (high frequency part). Note that disagreement is beginning to appear at low frequency for the lowest temperature (180K) spectrum. This disagreement is probably due to activated transport (hopping) processes not considered in the present analysis.

Table 6-1 Fitting parameters for the α and β-relaxation

T(K)	β-relaxation		α-relaxation		
	χ''_{min} (a.u.)	$\omega_{min}/2\pi$ (GHz)	τ_α (ns)	$\omega_{max}/2\pi$ (GHz)	β
260	1.68	358	0.0126	11.4	.722
240	1.53	261	0.0223	6.52	.731
230	1.45	198	0.0252	4.93	.724
220	1.34	165	0.0345	3.87	.709
210	1.22	132	0.0487	2.65	.735
200	1.18	107	0.0968	1.36	.684
180	1.05	69.5	0.372	.317	.718

In the fitting procedures, it was found that the critical exponent a was very sensitive to the fitting range while the χ''_{min} and ω_{min} were independent of the fitting range. This sensitivity of fitting range dependence was studied for PC by Du [22]. Generally, the critical exponent a depends on the low frequency limit but not the high frequency limit. The value of a increases as the low frequency limitation is extended to lower frequency. The critical exponent b increases as a increases due to the constraint of Eq. [5.12]. This result indicates that the b of the von Schweidler decay $(\omega_{min}/\omega)^b$

increases when more of the high frequency tail of the α-peak is included in the β-relaxation region.

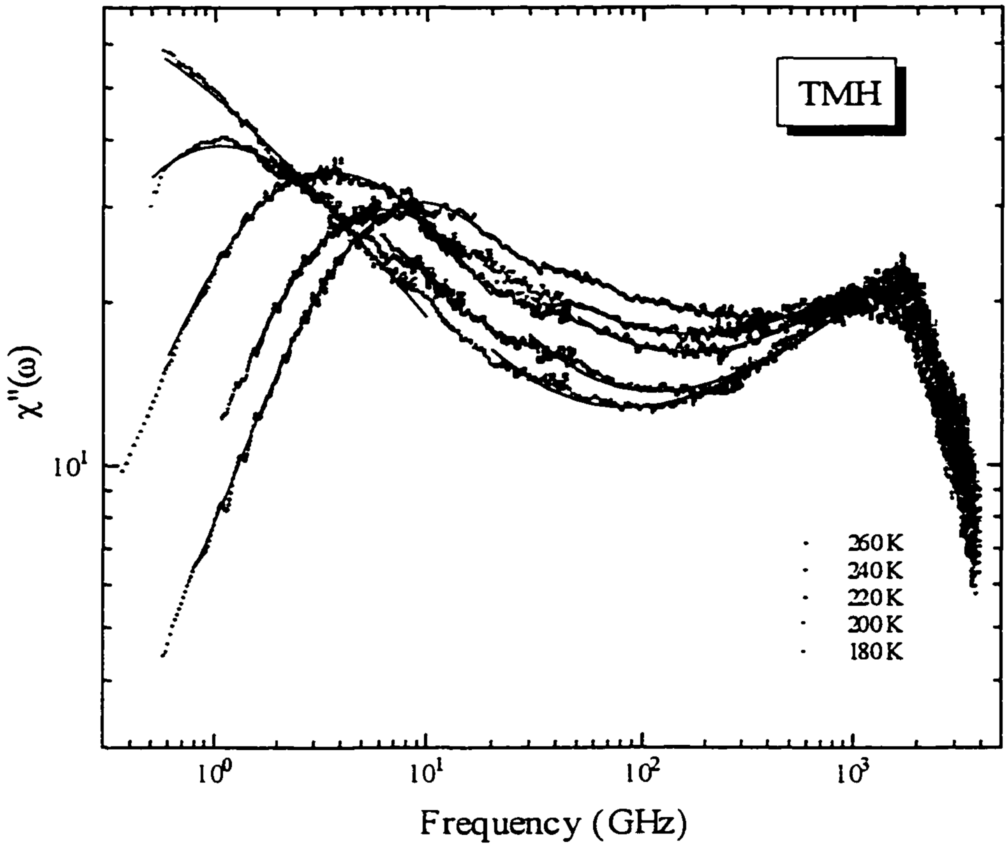

Figure. 6-5 Best global fit of $\chi''(\omega)$ data in the β region using Eq.[5.23] with λ = 0.77, a = 0.293, and b = 0.519 (thick solid line) and in the α region using Eq.[6.3] (thin solid line)

The MCT constraint of Eq. [5.12] was further tested by a consistentcy check in which both critical exponents a and b were treated as free fitting parameters. The best fit was obtained with a = 0.304 and b = 0.531, which are very close to the values obtained from the constrained fits. This agreement on the critical exponents a and b and the good description of the susceptibility spectra by the interpolation expression of Eq. [5.23] provide a strong support for the predictions of the MCT.

We also tested the β-relaxation scaling properties by rescaling $\chi''(\omega)$ and ω with χ''_{min} and ω_{min}, respectively. The rescaled curves are shown in Fig. 6-6. In Fig. 6-6, the β-relaxation region of different temperature curves can be expressed by a single master curve with the exponent parameter $\lambda = 0.77$ ($a = 0.293$, $b = 0.519$).

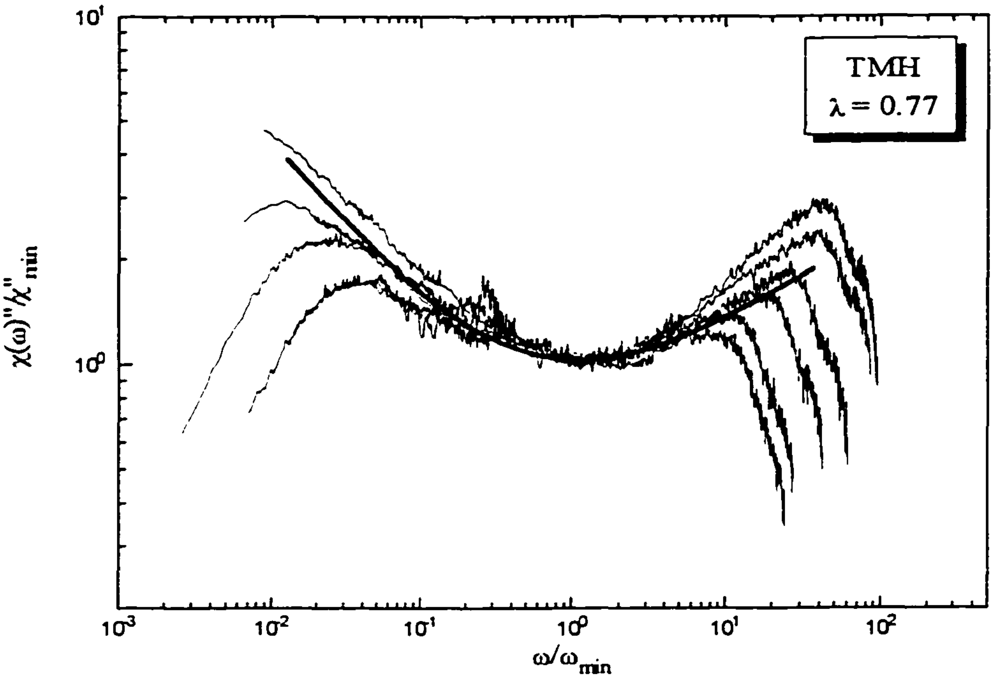

Figure 6-6 Rescaled plot of the Fig.6-4. The solid line is the master curve.

As a test of the scaling-law predictions of Eq. [5.24], we plot $(\chi''_{min})^2$ and $(\omega_{min})^{2a}$ versus temperature T in Fig. 6-7a and b respectively. In both plots, the data points indicate a linear dependence on temperature as predicted by the MCT. The extrapolation to the abscissa determines the crossover temperature T_C of MCT. A crossover temperature $T_C = 143$ K was obtained from the $(\chi''_{min})^2$ vs. T plot for TMH while the $(\omega_{min})^{2a}$ vs. T plot gave the $T_C = 142$ K.

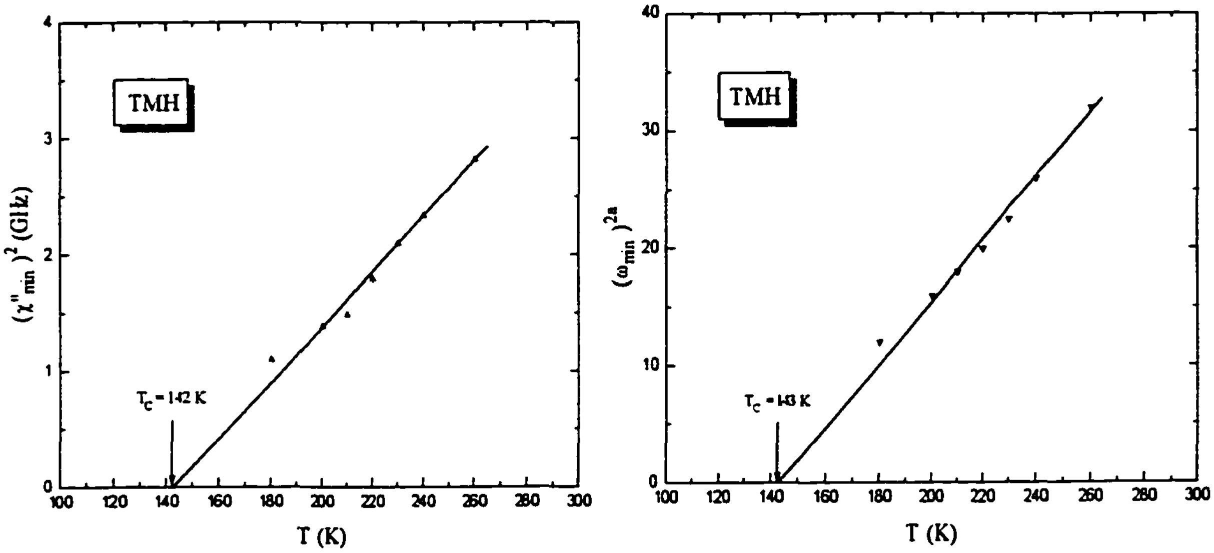

Figure 6-7a and b The temperature dependence of $(\chi''_{min})^2$ and $(\omega_{min})^{2a}$. The solid lines are linear fits to the data points.

According Eq. [5.24], the curve of log (χ''_{min}) versus log (ω_{min}) obeys a linear function with a slope which is equal to the critical exponent a:

$$\log(\chi''_{min}) = a \log(\omega_{min}) + C_1, \qquad [6.2]$$

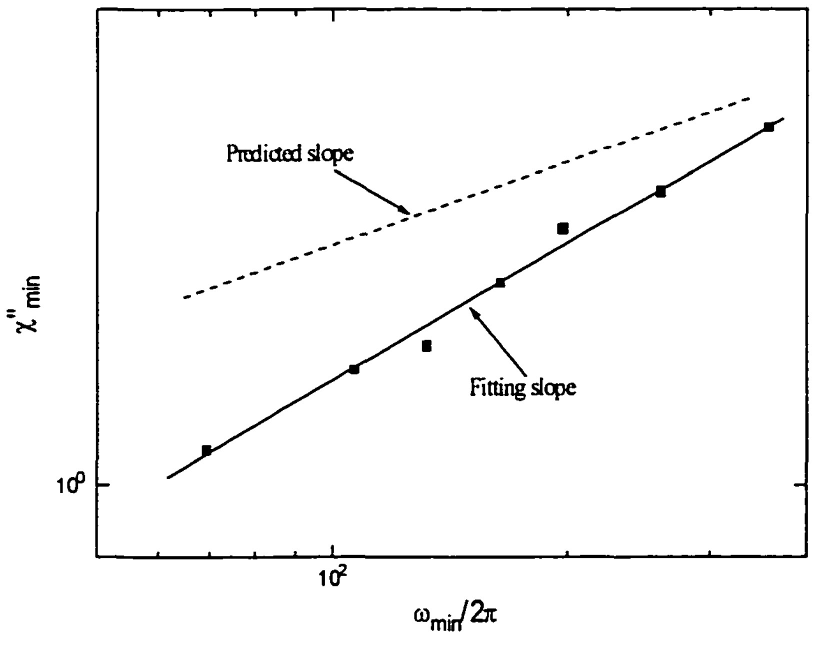

Figure 6-8 Log-log plot of (χ''_{min}) versus (ω_{min}).

where C_I is a constant. A cross test of the scaling-law predictions of Eq. [5.24] can be examined by plotting log (χ''_{min}) versus log (ω_{min}) as shown in Fig. 6-8. The data points exhibited a linear behavior as expected by Eq. [6.2], but the slope a = 0.43 was different than the expected value of a = 0.293. Similar discrepancies have also been found in the experimental results for other materials [19, 22]. This discrepancy was examined in Reference [62, 95] where it was found to arise from the temperature dependence of h_q in Eq.[5.13].

α-relaxation region

The most important features of α-relaxation observed in supercooled glass-forming materials are the rapid increase of the relaxation time and the strong non-Debye behavior of the relaxation function. The stretched exponential function is a good approximate solution for the scaling equation of the α-relaxation region.

The generally accepted α-relaxation function is the Kohlrausch Williams-Watts function, Eq. [2.31], but it is not convenient to use in a real fitting procedure for $\chi''(\omega)$. Often, the Cole-Davidson function is used to study the experimental spectra in order to extract information that can be compared with predictions of the MCT. In our fitting program, a numerical Fourier transformation of Eq. [2.31]

$$\chi''(\omega) = (A\omega/k_BT)\mathrm{Re}[\{\exp[-(t/\tau_\alpha)^{\beta_K}]\}] \qquad [6.3]$$

was used to fit the α-peaks. The amplitude A, relaxation time τ_α, and stretching constant β_K are treated as fitting parameters.

The low frequency data of the susceptibility spectra from 260 to 180 K were analyzed by Eq. [6.3] to obtain the temperature dependence of β_K and τ_α. The fitting curves (solid lines) to the experimental data for each temperature are shown in Fig. 6-5 (low frequency part). From the fitting results, we noted that the high frequency tail of the α-relaxation peak overlaps with the low frequency wing of the β-relaxation region. Therefore, it is important to restrict the fitting range so that the interference from the β-relaxation can be eliminated.

To illustrate the scaling of the α-relaxation, the rescaled spectra $\chi''(\omega)/\chi''_{max}$ versus ω/ω_{max} are shown in Fig. 6-9. Clearly, all the α- relaxation peaks fall approximately on a single master curve of Eq. [6-1] with $\beta_K = 0.73$ (solid line). There is no tendency for the α peak to narrow with increasing temperature.

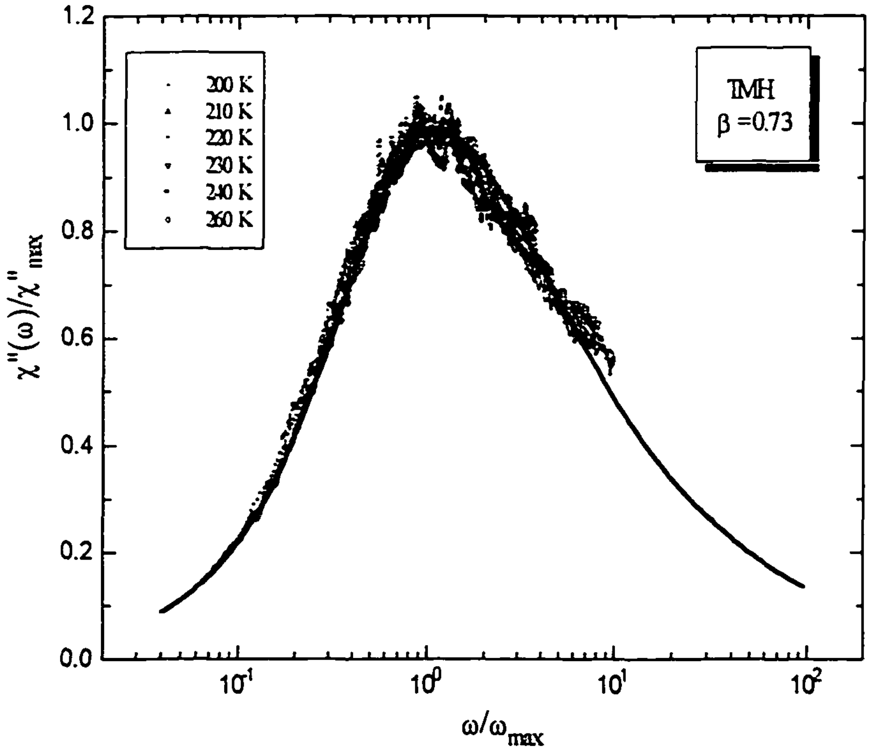

Figure 6-9 The rescaled plot of $\chi''(\omega)/\chi''_{max}$ versus ω/ω_{max}. The solid line is the theoretical curve of Eq.[6.3] with $\beta_K = 0.73$.

As emphasized in Chapter 5, information on the temperature dependence of the stretching constant β_K is a crucial test of the MCT and the percolation theory initially suggested by Campbell [108]. The stretching constant β_K found from these fits is plotted against temperature in Fig. 6-10. The fitting results show that $\beta_K = 0.73 \pm 0.05$ with no evidence of a systematic increase with increasing temperature. This result provides strong support for the MCT predictions of constant α-relaxation shape above T_C. Similar conclusions were also found in other studies on the fragile glass-forming materials [19, 21, 22, 24]. The temperature-independent β_K indicates that the α-relaxation obeys the time-temperature superposition principle.

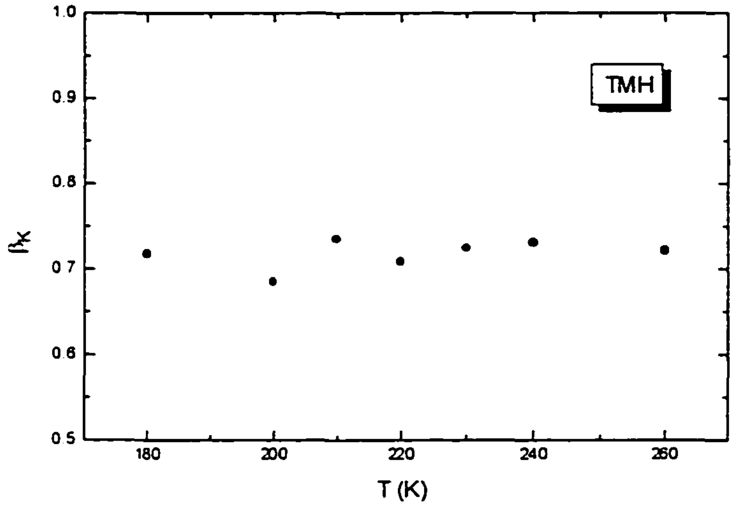

Figure 6-10 Temperature dependence of the stretched exponent β_K

As predicted by MCT, when the system is around the ideal glass transition region, the correlation function obeys the time-temperature superposition principle and the α-peak position is controlled by the scaling frequency ω_α. The MCT prediction for the temperature dependence of $\omega_{max} = 1/\tau_\alpha$ is given by Eq. [5.28]

$$\omega_{max}^{1/\gamma} = (1/\tau_\alpha)^{1/\gamma} \propto T - T_C$$

where γ is determined by $\gamma = 1/2a + 1/2b$ and the values of a and b were found from the β-relaxation fit. Fig. 6-11 shows this power law fit with $\gamma = 2.67$ given by a = 0.293 and b = 0.519 from the β-relaxation fit. This plot gives a crossover temperature T_C = 150 K which is somewhat higher than that obtained from the analysis of the β-relaxation region.

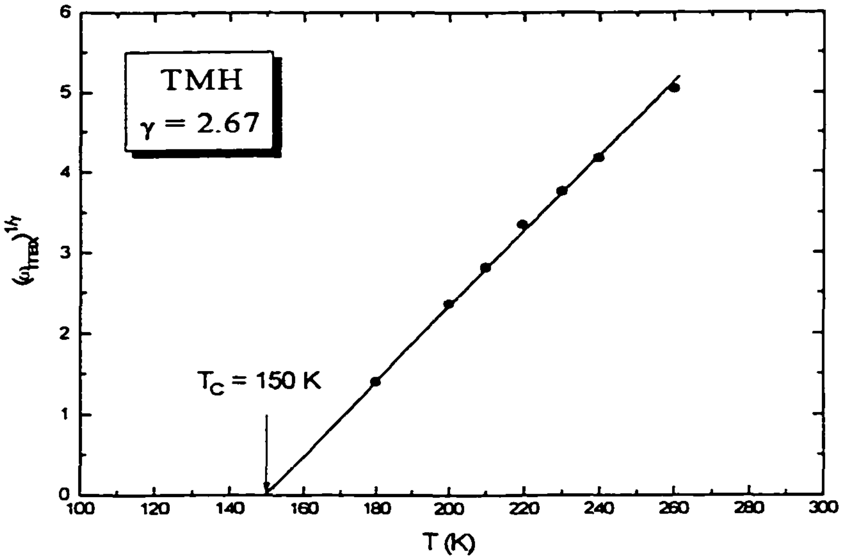

Figure 6-11 The temperature dependence of $\omega_{max}^{1/\gamma}$

Relaxation time

To compare the relaxation time τ_α with that obtained from the Brillouin scattering spectra, we plot τ_α and the relaxation times τ_M found from the Mountain theory and τ_D from the generalized hydrodynamic equation with the Cole-Davidson function fits in Fig. 6-12. The relaxation time τ_α for the α-relaxation processes is larger than τ_M and τ_D by a factor of about 10 (see Table 6-2). Similar results were also found in salol, PC, and OTP [21, 22, 68], although in most studies, the difference becomes smaller at high temperature.

This difference may be associated with the presence of two very different relaxation processes: the α-relaxation (slow relaxation) and β-relaxation (fast relaxation) in glass-forming materials, since the Mountain theory and generalized hydrodynamics equation only include the α-relaxation. If we ignore the β-relaxation,

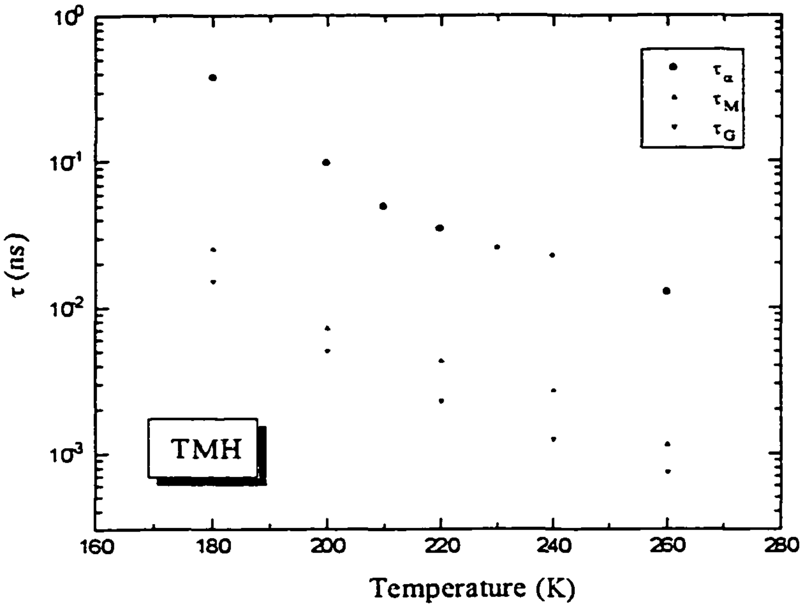

Figure 6-12 Temperature dependence of relaxation time τ_α from the α-peak fit (circle), τ_M from the Mountain theory fit (up-triangle), and τ_G from the generalized hydrodynamic equation with the Cole-Davidson function fit (down-triangle).

Table 6-2 Comparison of relaxation time

T (K)	τ_α (ns)	τ_M (ns)	τ_G (ns)
260	0.0126	0.00073	0.00114
240	0.0223	0.00124	0.00267
230	0.0252		
220	0.0345	0.00226	0.00426
210	0.0487		
200	0.0968	0.00498	0.00714
180	0.372	0.0153	0.0251

it will result in modified fitting parameters for the α relaxation since the parameters become severely distorted to account for the β-relaxation as well once the α peak frequency is below the Brillouin peaks [90].

To include the β-relaxation contributions, two other memory models, the empirical and hybrid model were reported [22, 90]. These analyses revealed the inadequacy of α-relaxation-only models and the importance of including β-relaxation in the analysis.

Recently, Soltwisch and co-workers [109] carried out an analysis of Brillouin spectra with a memory function which includes two Cole-Davidson functions: one represents the slow α-relaxation and the other represents the fast β-relaxation. They found that the fast relaxation time τ_β is temperature-independent while the slow relaxation time τ_α increases rapidly with decreasing temperature.

Despite these attempts, however, a complete explanation of the different structural relaxation times illustrated in Fig. 6-12 has not yet been achieved.

CONCLUSIONS

In this experimental study, polarized and depolarized Brillouin scattering spectroscopy and depolarized back-scattering spectroscopy were employed to study the dynamics of the liquid-glass transition and test the Mountain theory and mode coupling theory. Four glass-forming materials (OTP, PC, salol, and TMH) were analyzed. The results obtained from this study revealed many features common to glass-forming materials.

A. Brillouin Scattering Spectroscopy

Polarized spectrum

Conventional Brillouin scattering studies have primarily explored the longitudinal and transverse acoustic modes and their interactions with the α-relaxation. The polarized and depolarized Brillouin scattering spectra of OTP and PC were measured. The anisotropic contributions were subtracted from the VV spectra in order to obtain the isotropic spectra. These isotropic spectra were then compared with the Mountain theory.

An analysis employed different approximate versions of the Mountain theory to the polarized and isotropic spectra of OTP and PC. It was found that polarized spectra of OTP and PC could be fit well by the 4-Lorentzian, Mountain theory, and generalized hydrodynamic theory while the isotropic spectra could not be adequately described by these approaches due to the questionable subtraction approximation of Eq.[1.21]. Furthermore, equal quality fits could be obtained with different values of the fitting parameters. Therefore, the fitting parameters determined by these fits are not generally reliable.

The Brillouin scattering spectra of TMH, which has very weak depolarized scattering intensity compared to the polarized scattering intensity, were studied to avoid the subtraction problem. The polarized spectra of TMH were treated as isotropic spectra and fitted by the different versions of the Mountain theory directly. In the fitting procedures, the generalized hydrodynamics equation with the Cole-Davidson function gave the best fitting results although the other approaches also gave good fits. This result implies that the relaxation processes have the stretched exponential behavior.

However, the relaxation times obtained from the Brillouin spectra fits do not increase sufficiently rapidly as temperature decreases toward T_g. The α-relaxation time τ_α determined from the depolarized back-scattering spectra is about 10 times longer than that obtained from the Brillouin spectra fit of the generalized hydrodynamics equation with the Cole-Davidson function. Similar results were found in other glass-forming materials. Two other memory models, the empirical and hybrid model, were developed to investigate this difference but for all materials but CKN the results were inconclusive [21, 22]. These analyses revealed the inadequacy of α-relaxation-only models and the importance of including β-relaxation in the analysis.

We recognize that structural relaxation extends over many decades of frequency and that a large frequency window is required to accurately reveal the structural dynamics of the liquid-glass transition. Normal Brillouin scattering covers a spectral range of only about one decade and is not able to determine the structural dynamics unambiguously. Brillouin scattering spectra can be fitted accurately with α-relaxation-only models, but the fitting results are not likely to be physically meaningful once the temperature is low enough that the β-relaxation enters the experimental frequency window. Only when a complete memory function which includes both of the α and β-relaxation is used in the analysis of Brillouin scattering spectra, can the fit provide reliable and meaningful results, particularly for the relaxation time.

Depolarized Brillouin spectrum

The depolarized scattering spectrum includes contributions from orientational fluctuations, the coupling of translation velocity (shear waves) and rotational motion, and DID effects. The depolarized Brillouin spectra were measured in a large temperature region for OTP, PC, and Salol. Transverse modes due to the propagation of shear waves were observed in the low temperature spectra of all the materials studied but the Rytov dip (central dip) due to the coupling of the shear wave and orientational fluctuations was only observed in the high temperature spectra of salol.

Recently, the depolarized spectra of salol were analyzed with the Pick theory [61] in which the orientation-shear flow coupling with viscoelasticity is included. This theory provides a central dip at high temperatures and two transverse modes at low temperatures.

B. Isotropic Spectrum

Conventionally, the isotropic spectrum has been calculated by the subtraction procedure of Eq.[1.21]. This equation is valid only when there is no coupling of the shear waves and orientational fluctuations. However, there always is coupling of the shear waves and orientational fluctuations in real glass-forming materials composed of anisotropic molecules. We also found that the shear waves only contribute to the depolarized spectrum, while uncoupled orientational fluctuations and DID effects contribute to both polarized and depolarized spectra. Therefore, another problem arises: how to separate the orientational fluctuations and DID contributions to the depolarized spectrum. This separation has been carried out, at least qualitatively, by comparing the total depolarized intensity with a theoretical estimate for DID scattering.

C. Depolarized Back-Scattering Spectroscopy

A large-frequency-range (0.3 GHz ~ 4 THz) depolarized back-scattering study has been carried out in order to explore the dynamics of the glass-forming material TMH near the liquid-glass transition. The depolarized back-scattering geometry suppresses both the longitudinal and transverse Brillouin components and provides a high signal-to-noise ratio to observe the weak depolarized scattering spectrum. Since orientational dynamics are not important for TMH, the spectra are ascribed to DID scattering due to density fluctuations. The composite susceptibility spectra $\chi''(\omega)$ were converted from the intensity spectra by the fluctuation-dissipation theorem. In the $\chi''(\omega)$ spectra, both α and β-relaxation merge with the microscopic band at high temperature. With decreasing temperature, the α peak splits off from the microscopic band and the β-relaxation process develops. Around the crossover temperature T_C the relaxation spectra exhibit a well defined two-step relaxation process. The susceptibility spectra $\chi''(\omega)$ of TMH was analyzed with the idealized MCT.

β-relaxation

The β-relaxation processes were observed and the β-relaxation time scale was found to exhibit critical slowing down when the temperature approaches T_C. The composite susceptibility spectra $\chi''(\omega)$ were analyzed using the interpolation equation in the region of the minima from 180 to 260 K. This analysis provided acceptable fits with the exponent parameter $\lambda = 0.77$. The β-relaxation master function was then constructed by using λ obtained from the interpolation fit. Scaling the $\chi''(\omega)$ spectra minima region onto the master function confirmed the λ value.

The crossover temperature $T_C = 143$ K obtained from the power-law of χ''_{min} and $T_C = 142$ K obtained from the power-law of ω_{min} were very close but slightly lower than that obtained from the α-relaxation (150K). Although there was a slope-asymmetry problem which suggested that the theory is incomplete, scaling analysis for both χ''_{min} and ω_{min} indicated that the experimental results were generally in good agreement with the scaling-law predictions of the MCT.

α-relaxation

The α-relaxation peak of the susceptibility spectra $\chi''(\omega)$ exhibits rapid slowing down with decreasing temperature. The α peaks observed from 260 to 180 K were fitted with the stretched exponential function (KWW) and the temperature-dependent α peaks frequency ω_α (or the α-relaxation time $\tau_\alpha = 1/\omega_\alpha$) and the temperature-independent stretching exponent β_k were deduced.

The result of τ_α vs. T obeyed the power-law prediction of the MCT. $(\tau_\alpha)^{-1/\gamma}$ showing a linear temperature-dependence and extrapolation to zero led to the crossover temperature T_C = 150 K. The stretching exponent β_k was found to be about 0.73 and showed a temperature-independent behavior. This implied that the α-relaxation dynamics followed the time-temperature superposition principle predicted by the MCT.

Crossover temperature T_C

The crossover temperature T_C was deduced by a variety of anomalies of the spectra. The existence of a characteristic temperature T_C between 142 ~ 150K was obtained from the analysis of α and β-relaxation. It is difficult to confirm an accurate crossover temperature T_C for TMH because there is no other report about T_C of TMH. Table C-1shows some parameters of OTP, PC, Salol, and TMH obtained from MCT analyses.

By comparing these results, we conclude that TMH follows the same crossover pattern predicted by the MCT. It implies that the scaling behavior in these materials may be universal for all the fragile glass-forming materials. Although the idealized MCT can reasonably describe the experimental spectra, systematic differences between the experimental $\chi''(\omega)$ curves and the idealized

Table C-1 MCT analysis parameters for some glass-forming materials

Materials	T_m(K)	T_C(K)	T_g(K)	T_C-T_g	a	b	λ	β_K
OTP	329	289	243	46	0.31	0.55	0.74	0.60
PC	218	187	160	27	0.29	0.51	0.78	0.78
Salol	315	256	218	38	0.33	0.64	0.71	0.84
TMH	219	~150	~125	~25	0.29	0.52	0.77	0.73

MCT master curves on the low-frequency side for lower temperatures indicate the insufficiency of the idealized MCT. An extended MCT analysis, which includes the contribution of the hopping processes would probably correct the deviations. Recently, a new version of the MCT [110-111] which includes the orientational contributions has been developed. It was not attempted in this study because of the rather low signal-to-noise ratio of the spectra resulting from the weak depolarized scattering intensity.

D. Future Study

Brillouin scattering spectroscopy

In the analysis of Brillouin scattering spectra of supercooled liquids, the Mountain theory which is valid for liquids of isotropic molecules is widely used. However, most supercooled liquids are anisotropic. Their VV spectra contain isotropic contributions due to density fluctuations and anisotropic contributions due pure orientational fluctuations, while their VH spectra only contain anisotropic contributions due to orientational fluctuations and the coupling of orientation and shear waves. To obtain the isotropic spectrum, the conventional subtraction procedure does not work for liquids containing the coupling contribution. Furthermore, the coupling also modifies the longitudinal viscosity.

We will continue to study the polarized and depolarized spectra of salol using the Mountain theory, Pick theory, and Wang theory. We will try to develop a method to obtain a correct isotropic spectrum which can replace the procedure of simple subtraction.

Depolarized back-scattering spectroscopy

Depolarized back-scattering spectroscopy is a powerful technique to study the liquid-glass transition. Due to the very weak depolarized intensity of TMH, we could not obtain depolarized back-scattering spectra of TMH at low temperatures. We will continue the depolarized back-scattering measurements on TMH and try to obtain depolarized back-scattering spectra at low temperatures in order to complete the MCT analysis.

The glass transition singularity of the idealized MCT at T_C is smeared out due to the relaxation kernel contributions from hopping effects. To describe the depolarized back-scattering spectra of TMH more accurately, we will also use the extended MCT to analyze TMH spectra.

BIBLIOGRAPHY

[1] J. Wong and C.A. Angell, *Glass* (Marcel Dekker, New York 1978)

[2] C.A. Angell, J. Phys. Chem. Solids, 49, 863 (1988)

[3] R. Bohmer, K.L. Ngal, C.A. Angell, and D.J. Plazek, J. Chem. Phys. 99, 4201 (1993)

[4] W. Kauzmann, Chem. Rev 43, 219 (1948)

[5] M.L. Mansfield, J. Chem. Phys. 103, 8124 (1995)

[6] F.H. Stillinger, J. Chem. Phys. 88, 7818 (1988)

[7] A. Einstein, Ann. Phys. (Leipzig) 33, 1275 (1910)

[8] R.D. Mountain, J. Res. Natl. Bur. Standards 70A,207 (1966)

[9] T. Keyes and D. Kivelson, J. Chem. Phys. 54, 1786 (1971)

[10] R. Lipeles and D. Kivelson, J. Chem. Phys., 67, 4564 (1977)

[11] G. Adam and J.H. Gibbe, J. Chem. Phys. 43, 139 (1965)

[12] M.H. Cohen and D. Turnbull, J. Chem. Phys 31, 1164 (1959)

[13] G.S. Grest and M.H. Cohen, Phys. Rev. B 21, 4113 (1980)

[14] B. Leutheusser, Phys. Rev. A 29, 2765 (1984)

[15] U. Bengtzelius, W. Gotze, and A. Sjolander, J. Phys. C 17, 5915 (1984)

[16] W. Gotze and L. Sjogren, Rep. Prog. Phys. 55, 241 (1992)

[17] M.H. Cohen and G.C. Grest, J. Non-Cryst. Solid, 61-62, 749 (1984)

[18] W. Gotze L. Sjogren, J. Phys. C 21, 3407 (1988)

[19] G. Li, W.M. Du, X.K. Chen, H.Z. Cummins, and N.J. Tao, Phys. Rev. A 45,

3867 (1992)

[20] H.Z. Cummins, W.M. Du, M. Fushs, W. Gotze, S. Hildebrand, A. Latz, G. Li, and N.J. Tao, Phys. Rev. E 47, 4223 (1993)

[21] G. Li, W.M. Du, A. Sakai, and H.Z. Cummins, Phys. Rev. A 46, 3343 (1992)

[22] W.M. Du, G. Li, H.Z. Cummins, M. Fuchs, J. Toulouse, and L.A. Knauss, Phys. Rev. E 49, 2192 (1994)

[23] J. Wuttke, J. Hernendez, G. Li, G. Coddens, H.Z. Cummins, F. Fujara, W. Petry, and H. Sillescu, Phys. Rev. Lett. 72, 3052 (1994)

[24] H.Z. Cummins, G. Li, W. Du, Y.H. Hwang, and G. Shen, Prog. Theo. Phys. 126, 21 (1997)

[25] W. Steffen, A. Patkowski, H. Glaser, G. Meier, and E.W. Fisher, Phys. Rev. E 49 2992 (1994)

[26] W. Hayes and R. Loudon, *Scattering of Light by Crystals* (John Wiley and Sons, New York, 1978)

[27] J. W. S. Rayleigh, Philos. Mag. 12, 813 (1881)

[28] J. W. S. Rayleigh, Philos. Mag. 47, 375 (1889)

[29] L. Brillouin, Compt. Rend 158, 1331 (1914)

[30] L. Brillouin, Ann. Phys.(Paris) 17, 88 (1922)

[31] E. F. Gross, Nature 126, 201, 400, 603 (1930)

[32] L. Laudau, and G. Placzek, Phys. Z. Sowjetunion 5, 172 (1934)

[33] J.P. Boon and S.Yip, *Molecular Hydrodynamics* (McGraw-Hill, New York, 1980)

[34] B.J. Berne and R. Pecora, *Dynamic Light Scattering* (Wiley, New York, 1976)

[35] R.D. Mountain, Rev. Mod. Phys. 38, 205 (1966)

[36] R.D. Moutain, J. Res. Natl. Bur. Standards 72A, 95 (1968)

[37] S.M. Rytov, Sov. Phys. JETP 6, 401 (1958)

[38] G.I.A. Stegeman and B.P. Stoicheff, Phys. Rev. Lett. 21, 202 (1968)

[39] G.I.A. Stegeman and B.P. Stoicheff, Phys. Rev. A 1, 1160 (1968)

[40] R.Y. Chioa, and B.P. Stocheff, Phys. Rev. Lett. 54, 1286 (1964)

[41] G.B. Benedek, J.B. Lastobka, and K. Fritsch, J. Opt. Soc. Amer.54,1284 (1964)

[42] W.S. Gornell, G.I. Stegeman, and B.P. Stoicheff, Phys. Rev. Lett. 17, 297 (1966)

[43] L.M. Torell, J. Chem. Phys. 76, 3467 (1983)

[44] C.H. Wang, X.R. Zhu, and J.C. Shen, Mol. Phys. 62, 749 (1987)

[45] Y.H. Lin and C.H. Wang, J. Chem. Phys. 70, 681 (1979)

[46] Y. Higashigaki and C.H. Wang, J. Chem. Phys. 74, 3175 (1981)

[47] E.W. Fisher, Ch. Becker, J.U. Hagerah, and G. Meier, Progr. Colloid and Polymer Sci. 80, 198 (1989)

[48] W. Steffen, A. Patkowski, G. Meier, and E.W. Fisher, J. Chem. Phys. 96, 4171(1992)

[49] P.J. Carroll and G.D. Patterson, J. Chem. Phys. 81, 1666 (1984)

[50] R. Zwanzig, J. Chem. Phys. 43, 714 (1965)

[51] C. Allen-Demoulin, P. Lallemand, and N. Ostrowsky, Mol. Phys. 31, 518 (1976)

[52] C.J. Montrose, V.A. Solovyev, and T.A. Litovitz, J. Acoust. Soc. America 43, 117 (1968)

[53] M.A. Leontovich, Izv. Akad. Nauk SSSR, 633 (1941)

[54] I.L. Fabelinskii, L.M. Sabirov, and V.S. Starunov, Phys. Lett. A 29, 414 (1969)

[55] T. Keyes and D. Kivelson, J. Chem. Phys. 56, 1876 (1972)

[56] H.A. Andersen and R. Pecora, J. Chem. Phys. 54, 2584 (1991)

[57] C.H. Wang, J. Chem. Phys. 70, 3796 (1979)

[58] C.H. Wang, Mol. Phys. 41, 541 (1980)

[59] C.H. Wang, Mol. Phys. 58, 497 (1986)

[60] D. Kivelson and G. Tarjus, Phys. Rev. E 47, 4210 (1993)

[61] C. Dreyfus, A. Aouadi, R.M. Pick, T. Berger, A. Patkowski, and W. Steffen, Europhys. Lett. 42, 55 (1998)

[62] H.Z. Cummins, G. Li, W. Du, R.M. Pick, and C. Dreyfus, Phys. Rev. E 53, 896 (1996)

[63] J. Rouch, C.C. Lai, and S.H. Chen, J. Chem. Phys. 65, 4016 (1976)

[64] G. Maisano, P. Miglardo, and G. D'Arrigo, Phys. Rev. Lett. 52, 1025 (1984)

[65] N.J. Tao, G. Li, and H.Z. Cummins, Phys. Rev. B 43, 5815 (1991)

[66] N.J. Tao, G. Li, and H.Z. Cummins, Phys. Rev. B 45, 686 (1992)

[67] G. Shen, H. Barshilia, H.Z. Cummins, *APS March Meeting* (1998)

[68] Y.H. Hwang, G. Shen, W. Du, and H.Z. Cummins, *APS March Meeting* (1997)

[69] M. Born and E. Wolf, *Principles of Optics* 5th ed. Oxford (1975)

[70] J. R. Sandercock, in *Proc. 2nd Int. Conf. on Light Scattering in Solids* edited by M. Balkanski, 9 (1971)

[71] J. R. Sandercock, Solid State Comm. 26, 547 (1978)

[72] J.R. Huck, G.A. Noyel, L.J. Jorat, and A.M. Bondeau, J. Electrostatics 12, 221

(1982)

[73] A. Bondearu and J.R. Huck, J. Phys. (Paris) 46, 1717 (1985)

[74] M. Elmroth, L. Borjesson, and L.M. Torell, Phys. Rev. Lett. 68, 79 (1992)

[75] L. Simeral and R.L. Amey, J. Phys. Chem. 74, 1443 (1970)

[76] L. Borjesson, M. Elmroth, and L.M. Torell, Chem. Phys. 149, 209 (1990)

[77] A.K.M. Masood, R.A. Pethrick, A.J. Barlow, M.G. Kim, R.P. Plowiec, D. Barraclough, and J.A. Ladd, Adv. Molecular Relaxation Processes 9, 29 (1976)

[78] G. Fytas, C.H. Wang, D. Lilge, and Th. Dorfmuller, J. Chem. Phys. 75, 4247 (1981)

[79] G. D'Arrigo, J. Chem. Phys. 63, 61 (9175)

[80] M.H. Cohen and G.S. Grest, Phys. Rev. B 20, 1077 (1979)

[81] M. Naoki and S. Koede, J. Chem. Phys. 93, 948 (1989)

[82] S.S. Cheng and A.B. Bestul, J. Chem. Phys. 56, 503 (1972)

[83] E.W. Fischer, G. Meier, T. Rabenau, A. Patkowski, and W. Steffen, J. Non-Crystall. Solids 131-133, 134 (1991)

[84] B.D. Malhotra and R.A. Pethrick, Phys. Rev. B 28, 1256 (1983)

[85] L.J. Lewis and G. Wahnstrom, Phys. Rev. E 50, 3865 (1994)

[86] W. Peter, E. Bartsch, F. Fujara, M. Kiebel, H. Sillescu, and B. Farago, Z. Phys. B 83, 175 (1991)

[87] E. Bartsch, F. Fujara, J.F. Legrand, W. Peter, H. Sillescu, and J. Wuttke Phys. Rev. E 52, 738 (1995)

[88] C.P. Lindsay and G.D. Patterson, J. Chem. Phys. 73, 3348 (1980)

[89] E.W. Fischer, Ch. Becker, J-U. Hagenah, and G. Meier, Progr. Colloid & Polymer Sci. 80, 189 (1989)

[90] G. Li, W. Du, J. Hernandez, and H.Z. Cummins, Phys. Rev. E 48, 1192 (1993)

[91] J. Toulous and C. Launay, Rev. Sci. Instrum. 59, 492 (1988)

[92] G.L. Peterson, B.Chick, and W. Junker, Ultrasonic Symposium Proceeding IEEE, 407 (1987)

[93] J. Toulous and P. Finkel, Unpublished, Private communication (1997)

[94] C. Ecolivet, Unpublished, Private communication (1998)

[95] H.Z. Cummins, G. Li, Y.H. Hwang, G. Shen, W. Du, J. Hernandez, and N.J. Tao, Z. Phys. B 103, 501 (1997)

[96] A. Patkowski, W. Steffen, H. Nilgens, E.W. Fischer, and R. Pecora, J. Chem. Phys. 106, 8401 (1997)

[97] G. Li, M. Fuchs, W. Du, A. Latz, N.J. Tao, J. Hernandez, W. Gotze, and H.Z. Cummins, J. Non-Cryst. Solid, 172-174, 43 (1994)

[98] H.Z. Cummins, G. Li, W. Du, R.M. Pick, and C. Dreyfus, Phys. Rev. E 53, 896 (1996)

[99] L. Wu and L.J. Lewis, Physica A 201, 150 (1993)

[100] A. Patkowski, E.W. Fischer, H. Glaser, G. Meier, H. Nilgens, and W. Steffen, Progr. Colloid & Polymer Sci. 91, 35 (1993)

[101] G.D. Enright and B.P. Stoicheff, J Chem. Phys. 64, 366 (1976)

[102] C.H. Wang and J. Zhang, J. Chem. Phys. 85, 794 (1986)

[103] S.P. Das and G.F. Mazenko, Phys. Rev. A 34, 2265 (1986)

[104] W. Gotze and L. Sjogren, Z. Phys. B 65, 415 (1987)

[105] W. M. Du, Ph. D. Thesis (1996), CUNY

[106] W. Gotze, in *Liquids, Freezing and glass transition*, edited by J.P. Hansen, D.Levesque, and J. Zinn-Justin (North-Holland, Amsterdam, 1990) p. 287

[107] W. Gotze, J. Phys. Condens. Matter 2, 8485 (1990)

[108] I.A. Campbell, Phys. Rev. B 33, 3587 (1986)

[109] M. Soltwisch, G. Ruocco, B. Balschun, J. Bosse, V. Mozzacurati, and D. Quitmann, Phys. Rev E 57, 720 (1998)

[110] T. Franoch, M. Fuchs, W. Gotze, M.R. Mary, and A.P. Singh, Phys. Rev. E 56, 5659 (1997)

[111] R. Schilling and T. Scheidsteger, Phys. Rev. E 56, 2932 (1997)

IMAGE EVALUATION
TEST TARGET (QA-3)

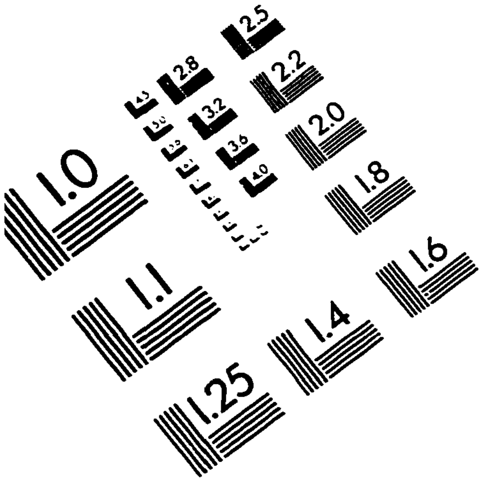

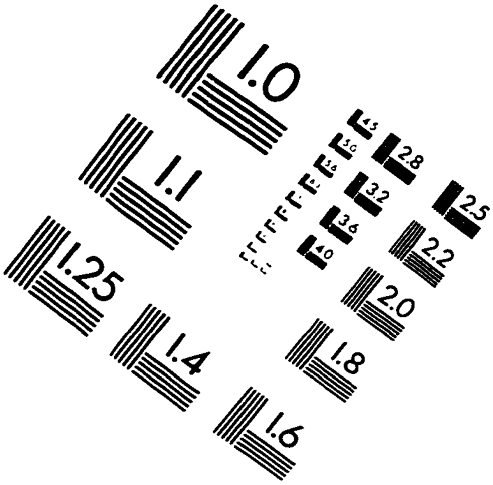

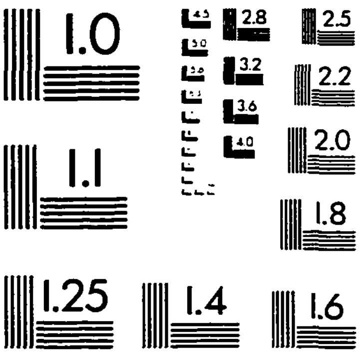

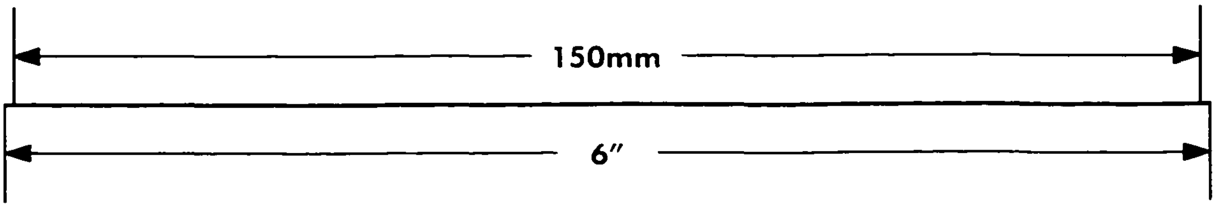

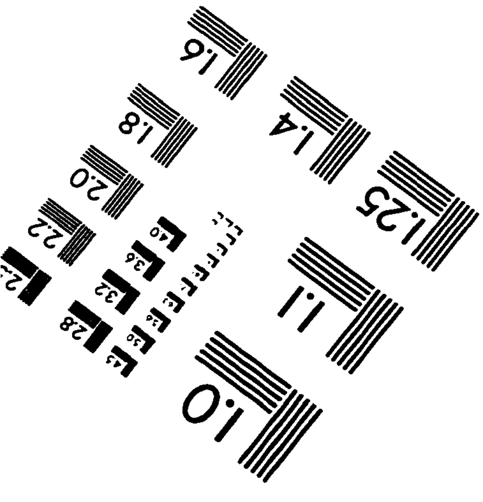

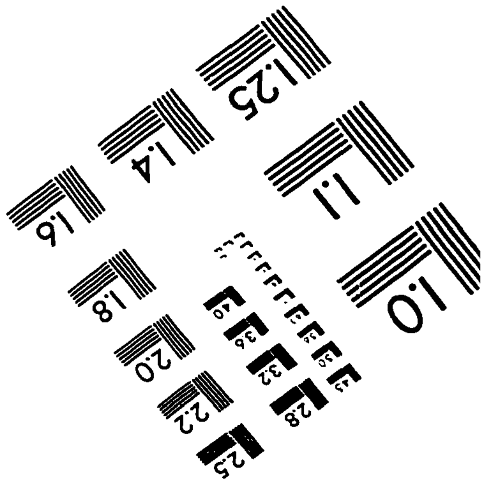

APPLIED IMAGE . Inc
1653 East Main Street
Rochester, NY 14609 USA
Phone: 716/482-0300
Fax: 716/288-5989